Universidad Nacional Autónoma de México

Posgrado en Ciencias Físicas

Near-Field Radiative Heat Transfer and Optical Properties of Nanoparticle Systems

T E S I S

QUE PARA OPTAR POR EL GRADO DE:

Doctor en Ciencias Físicas

PRESENTA:

David Becerril Rodriguez

TUTOR PRINCIPAL:

Dra. Ana Cecilia Noguez Garrido

Instituto de Física, UNAM

COMITE TUTOR:

Dr. Raúl Patricio Esquivel Sirvent

Instituto de Física, UNAM

Dr. Carlos Villareal Luján

Instituto de Física, UNAM

Ciudad de México, Mayo 2019

Acknowledgements

1

Resumen

En este trabajo se estudian las propiedades ópticas y la transferencia de calor por medio del campo eléctrico cercano, de sistemas compuestos por nanopartículas polarizables. Con este fin, el primer capítulo revisa los principios físicos y los antecedentes teóricos de las ondas superficiales y los efectos de campo cercano en tales sistemas. Específicamente se consideran los casos de nanopartículas metálicas y dieléctricas. Después, el trabajo se divide en dos partes principales. En el primero, se introduce un método para estudiar la respuesta óptica de un sistema de nanopartículas esféricas interactuantes cuando son excitados por campos externos multipolares. El método teórico separa las propiedades geométricas y dieléctricas y la simetría del campo incidente. Permite el análisis del acoplamiento del sistema con el campo externo, de modo que se puede predecir la geometría para óptimzar la el coeficiente de dispersión. El método explota la simetría del campo electromagnético incidente para mejorar o suprimir modos específicos, que, a su vez, determinan el campo cercano eléctrico. También se obtiene cuantifica las contribuciones al campo eléctrico cercano de los diferentes momentos multipolares. Se demuestra el método usando un dímero plasmónico de nanoesferas. Los resultados obtenidos en este trabajo son los primeros que utilizan la representación espectral para calcular el campo cercano eléctrico y considerar campos externos no homogéneos. Se encontró que a pequeñas distancias de separación, el campo externo espacialmente modulado se acopla más fuerte a más modos que el campo externo homogéneo. Los resultados y análisis de esta sección fueron publicados en la ref. (1).

En la segunda parte, la energía transferida a través de campos electromagnéticos radiados térmicamente entre nanopartículas dieléctricas a diferentes temperaturas se estudia teóricamente considerando el acoplamiento mutlipoar completo entre los campos eléctricos y las partículas. Usando los métodos desarrollados en la primera sección para estudiar los modos de superficie y el campo cercano eléctrico en sistemas de nanopartículas interactivas, mostramos que los modos acoplados entre nanopartículas abren canales a través de

los cuales los campos electromagnéticos radiados térmicamente pueden transferir energía, y que métodos anteriores no han completamente analizado. Los modos acoplados aumentan la potencia de intercambio en más de un orden de magnitud en comparación con los modelos existentes que generalmente consideran solo interaccion dipolar. En consecuencia, la inclusión de modos acoplados se vuelve esencial para describir el fenómeno correctamente y podría explicar las grandes desviaciones observadas en los experimentos en comparación con los modelos actuales. Discutimos cómo la contribución de los modos acoplados cambia según los parámetros del sistema varían para los casos de un sistema de dos y tres partículas. Esto se hace modificando el formalismo de representación espectral para el campo cercano, incorporando momentos multipolares fluctuantes, que permiten identificar la contribución de la transferencia de energía de cada modo acoplado. Se observó que el acoplamiento de multipolos de orden superior puede conducir a un gran aumento en la transferencia de energía cuando se compara con modelos que solo incluyen interacción dipolar. La contribución a la transferencia de energía por diferentes modos multipolares fue luego analizada sistemáticamente. Esta información se puede utilizar para comprender y controlar el flujo de energía entre las nanopartículas que están muy cerca. Los resultados y análisis de esta sección fueron publicados en la ref. (2).

Abstract

This work studies the optical properties and near-field radiative heat transfer composed of systems of polarizable nanoparticles. To this end, the first chapter reviews the physical principals and theoretical background of surface waves and near-field effects in such systems. Specifically the cases of metallic and dielectric nanoparticles are considered. Afterward, the work is divided into two main parts. In the first, a method is introduced to study the optical response of a system of interacting spherical nanoparticles when excited by multipolar external fields. The theoretical method puts on the same footing geometric and dielectric properties and the symmetry of the incident field. It allows the analysis of the coupling of the system with the external field so that optimal geometry for maximum scattering cross-section can be predicted. It exploits the symmetry of the incident electromagnetic field to enhance or suppress specific modes, which, in turn, tunes the electric near-field. Contribution to the near-field from the coupling of different multipolar moments are also obtained. We first demonstrate the method by using a plasmonic dimer of nanospheres. To the authors knowledge, the results obtained in this work, are the first that use the spectral representation to calculate the electric near-field and consider non homogeneous external fields. It was found that at small separation distances, the spatially modulated external field couples stronger to more modes than the homogeneous external field. The results and analysis of this section were published in Ref. (1).

In the second part, energy transferred via thermally radiated electromagnetic fields between dielectric nanoparticles at different temperatures is studied theoretically by considering full coupling between all thermal electric fields for the cases of a dimer and a trimer. Using the methods developed in the first section to study the surface modes and electric near-field in systems of interacting nanoparticles, we show that coupled modes between nanoparticles act as channels through which thermally radiated electromagnetic fields may transfer energy, and which previous methods have not fully analyzed. Coupled modes increases the power exchanged more than one order of magnitude as compared with existing

models which typically consider only dipole interaction. Consequently, the inclusion of coupled modes becomes essential to describe the phenomenon correctly and might explain the large deviations observed in experiments as compared with current models. We discuss how the contribution from coupled modes changes as parameters of the system are varied for the cases of a two and three particle system. This is done by modifying the spectral representation formalism for the near field, incorporating fluctuating multipolar moments, allowing identification of the contribution of energy transfer of each coupled mode. It was seen that the coupling of higher order multipoles can lead to a large increase in energy transfer when compared to models that only include dipolar interaction. The contribution to energy transfer by different multipolar modes was then systematically analyzed. This information can be used to understand and control the energy flux among nanoparticles in close proximity. The results and analysis of this section were published in Ref. (2).

Contents

Chapter 1

General Introduction

The interaction of matter with electromagnetic (EM) fields is a process that is essential to everyday life. To give an idea, the principal source of usable energy on earth comes from the emission of EM fields from the sun and the ability to absorb this energy is what allows plants to carry out the process of photosynthesis. Our sense of vision, which is our primary manner of understanding our environment, is due light that reaches our eyes after interacting with matter. Many of the advances in science have been thanks to the ability to manipulate, control and trap EM fields, which has been possible thanks to the knowledge of optical properties of different systems, allowing design and construction of devices for particular purposes.

The word *nanostructure* refers to a system with a characteristic size in the range of approximately up to a hundred nanometers (3). With the advent of nanofabrication technologies, more and more attention has been paid to physical phenomena occurring at this scale. In particular, the study of the optical properties of nanostructures has been a very active research area during the last decades and is relevant due to the unusual properties found in these systems. This interest is not only of fundamental character but is based on their possible technological application. Optical properties of these systems are of interest due to their variety of behavior, depending on the geometrical configuration and type of material. At this scale, the intrinsic properties (electronic, optical, thermal conductivities, chemical reactivity, etc.) are not solely determined by the material nature and quality but become critically dependent on the geometrical structure such as size, shape, and physical surroundings. For example, a lot of exciting and exotic optical properties in light absorption/radiation have been achieved by utilizing metamaterials, which are artificial materials composed of sub-wavelength structures (4). Researchers have demonstrated perfect light absorbers which almost absorb all incoming light at normal incidence at specific wavelengths in the near-infrared regime (5). As new physical properties can be obtained by

scaling down the structures, a huge work is done recently on tailoring and characterizing the properties of such nanostructures. Tailored absorption spectrum can be applied to many applications, including solar energy harvesting (6) , biomedical sensing (7), cloaking (8) etc. Additionally, the study of the optical response of these materials is important in various optical spectroscopies since they can be used to characterize the growth process and formation as well as enhance the spectroscopic signal. Optical spectroscopies are very convenient because of their non-destructive properties and because they can be performed in the same device in which the growth process is carried out.

In this work, the term *optical properties* will not be limited to the visible spectrum; instead, it includes the response of a material to external EM excitations over a wide range of frequencies. Of particular interest are the response properties of nanostructures to thermally emitted EM fields. The environment is typically full of thermal radiation since every material above absolute zero emits EM waves. However, this is not always evident because objects at room temperature radiate EM waves dominantly at infrared frequencies, which are not perceivable by the naked eye. Thermal radiation can play an important role for scenarios when other energy transfer mechanisms, such as thermal conduction and convection are obstructed, intentionally or unintentionally, such as devices operating in space. Therefore, there is a demand for engineering the thermal radiation properties of an object to control heat dissipation via radiation. This requires understanding and application of precision-controlled energy and heat transfer mechanisms for the development of novel engineering platforms. At the nanometer scale, traditional heat transfer formulations cease to be valid. This deviation from the classical theory is due to so-called near-field effects and give rise to new phenomena, such as a drastic enhancement of energy transfer compared to known predictions. This has lead to considerable growth in research of radiative heat transfer at the nanoscale. Near-field effects in radiative heat transfer, open up new possibilities for many promising applications, such as radiative cooling(9) , nano-gap thermophotovoltaics (10) , thermal rectifications (11) , thermal transistors (12), thermal memory devices (13), etc.

The work presented in this thesis, we study the physical mechanisms underlying the phenomenon of near-field radiative heat transfer and optical properties in systems of interacting nanoparticles (NPs) and the dependence on the system parameters such as size, separation distances, and dielectric properties. First, a brief introduction to the physical phenomena underlying surface modes in dielectric and metallic nanostructures is given. Following this, the dissertation is then divided into two parts.

As an initial step to understanding radiative heat transfer in NP systems, in the first part of the thesis, the optical response and near-field enhancement in systems of metallic NPs are studied. The spectral representation of the dielectric response of a medium composed of the mixture of two materials is advantageous in the determination of the properties from their geometrical characteristics. Although the existence of the spectral representation of the dielectric response of any isotropic compound medium fostered by two phases has been demonstrated, its concrete form for a particular material has only been determined in some cases. Rigorously, the spectral representation has been found only for isolated particles, in various systems in the mean-field approximation and the cases of dielectric spheres, spheroides, and concentric nanoshell systems (14) . In the latter case, multipolar contributions were also included. The spectral representation allows us to determine the proper active modes through the diagonalization of a Hermitian matrix that incorporates all the geometrical properties of the system. It allows calculating the wavelength of the resonance that is observed in the optical spectra of particles on the substrate. The role of multipolar interaction is emphasized which allows tailoring of the systems optical properties. The case of a homogeneous and nonhomogeneous field that satisfy $\nabla \cdot \vec{E} = \text{const.}$, are studied and compared. We point out that understanding the interaction of NPs with non-homogeneous fields is a necessary step to understand the interaction of NPs with thermally excited fields, since it will be seen that random thermal movement excites all orders of multipolar EM fields.

In the second part, the physical mechanisms underlying the phenomenon of near-field radiative heat transfer in systems of interacting NPs is studied. A method is developed that takes into account full multipolar interaction of the thermal fields. This is achieved by introducing fluctuating thermal sources into the spectral representation. The manner which radiative heat transfer depends on the system parameters such as size, separation distances, and dielectric properties and the role of interaction effects, such as the coupling of the system's surface modes is also examined.

Chapter 2

Fundamentals of near-field radiation

In general, any propagating wave, whether EM, sound, etc., cannot be focused down to a spot smaller than about half its wavelength. This restriction is commonly referred to as the diffraction limit. In the optical and infrared frequencies, the wavelength is of the order of hundreds of nanometers. It would appear that the diffraction limit precludes the use of EM fields in the study of nanometric sized systems. However, it has come to be understood that this is not always the case and that the diffraction limit can be overcome (15). The central idea behind this is that EM fields are not restricted to freely propagating waves. These can also exist in the form of evanescent waves, which are localized near the surface of the objects. These fields are very intense near the object's surface and rapidly decay away from them, for which they are known as surface modes. The region near the surface of an object, where evanescent fields are still appreciable is referred to as the "near field" of the object. Conversely, the "far field" region is where evanescent fields are negligible and propagating waves dominate. Near-field radiation is not subject to the same diffraction limit as far-field radiation and can be used to confine EM fields to dimensions as small as the atomic scale (16).

Evanescent waves can be generated by different mechanisms, which are partially determined by the material of the body and on the type of excitation that an external EM field couples to. In this work, we are interested in the interaction of EM fields and matter at the optical and infrared spectra. It is, therefore, necessary to understand the physical phenomena underlying evanescent waves at this frequency range. Fig.2.1 presents a schematic representation of the different possible types of excitations that can couple to EM fields and the energy at which they are expected to appear. We point out two different types of excitations which are important to this work and which are found at the optical and infrared range, namely, plasmons and optical phonons. Plasmons are the collective oscillations of the nearly free electrons found in certain types of metals and are located in the visible part

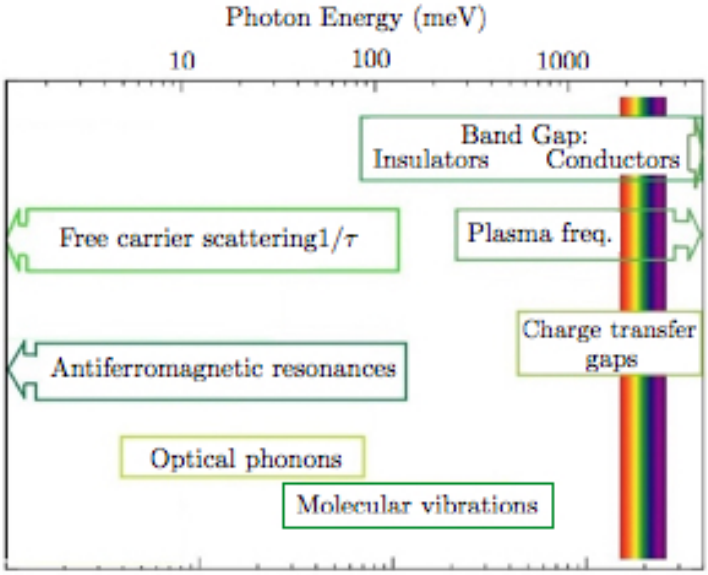

Figure 2.1: Chart showing optical processes in solids and the frequency and energy in which they are typically found. Image modified from (17)

of the spectrum. The incident field generates collective oscillations of the electrons, which move the electronic cloud with respect to the nuclei, generating a restitution force that acts against the force due to the incident field. Interaction between a driving force at a particular frequency and a restitution force gives rise to characteristic resonant frequencies, similar to the case of a driven harmonic oscillator. These characteristic frequencies of each system known as plasmonic resonances (18, 19). In conductive metals such as Au and Ag, plasmonic resonances are found at frequencies within the visible spectrum (20). On the other hand, phonons are the collective oscillations of the ions of a lattice. For example, in dielectrics such as SiC or SiO_2, resonant frequencies can be found in the infrared (21). The strong coupling between photons and plasmons (phonons)results in excitations being neither plasmons (phonons) nor photons but rather a mixed excitation, and modeled as a quasi-particle known as a polariton. Coupling of an EM wave and a charge density of the electrons within a metal is known as plasmon-polariton (19), while the coupling to a phonon is known as a phonon-polariton. When this excitation occurs at a surface between two bodies, they are known as surface-polaritons. Excitations of this kind create a charge density localized near the body's surface. This gives rise to intense EM fields that decay rapidly in the direction perpendicular to the surface. Many of the optical properties of a material will depend on the coupling of EM fields to either plasmons or phonons.

In the following section, we discuss and compare the physical phenomena responsible for surface modes in dielectrics and metals. We give a general introduction to the interac-

tion of optical and infrared EM fields with solid materials emphasizing the existence and characteristics of the surface modes of a given system. The basic concepts of the resonant character of plasmon and phonon modes are discussed. A review of how surface waves can be excited by external fields, including thermal radiation, is given. The dielectric functions necessary to describe both plasmonic and phononic resonances is also discussed. At the nanometric scale, optical properties are not solely determined by the material but become critically dependent on the geometrical structure. To illustrate this, the case of surface modes existing on a plane interface are considered as well as the case of spherical particles. Finally, the modification of surface modes in system's of NPs due to interaction with other polarizable structures is examined.

2.1 Surface modes and evanescent fields

In general, the interaction of EM waves with a material object can be described in terms of physical processes such as radiation, absorption, scattering, and propagation. Radiation refers to the manner through which energy, in the form of EM fields, emanates from a body. This occurs when charge carriers within the body are accelerated due to random thermal movement, converting internal energy into EM fields. Absorption can be seen as the inverse process: energy is taken from external EM fields and converted into internal energy. Scattering and propagation of EM fields refer to the redirection of incident fields and is related to the phenomena of refraction, reflection,transmission, absorption etc.. These physical processes define a system's optical properties, i.e., the manner in which EM fields interact with a particular body.

To calculate a system's optical properties, Maxwell's equations must be solved with the corresponding boundary conditions. In general, rigorous solutions of the Maxwell equations for an arbitrary configuration are not straightforward. In 1908, Gustav Mie found the exact solution to the Maxwell equations for the response of a homogeneous sphere of arbitrary size immersed in a homogeneous medium, subjected to a plane monochromatic wave (22). For non-spherical geometries, only a few exact solutions are known: the case of spheroids by Asano and Yamamoto (23) and for infinite cylinders by Lind and Greenberg(24). In this work, we consider nanostructures which are large enough to employ classical EM theory. However, they are small enough to observe the dependence of the optical properties with their size and shape. Each point of the system can be described in connection to a macroscopic dielectric function, which depends on the frequency and sometimes on its size.

As an illustrative example, consider the case of an interface between two semi-spaces of different local and homogeneous media with dielectric and magnetic functions $\epsilon_1(\omega), \mu_1(\omega)$ and $\epsilon_2(\omega), \mu_2(\omega)$ in the absence of sources. For simplicity we do not write the explicit spatial dependence in the fields and constitutive relations. Maxwell's equations in the frequency domain are (18)

$$\begin{aligned} \nabla \cdot \vec{D} &= 0 \qquad & \nabla \times \vec{E} &= -i\omega\vec{B} \\ \nabla \cdot \vec{B} &= 0 \qquad & \nabla \times \vec{H} &= i\omega\vec{D}, \end{aligned} \tag{2.1}$$

where $\vec{E}$ and $\vec{B}$ are the electric and magnetic fields. The constitutive relations can then be written as $\vec{D} = \epsilon_j(\omega)\vec{E}$ and $\vec{B} = \mu_j(\omega)\vec{H}$ with $j = 1, 2$. Maxwell's equations in semi-space j can be reduced to a wave equation

$$\frac{1}{\mu_j \epsilon_j} \nabla^2 \vec{E} = \omega^2 \vec{E}, \tag{2.2}$$

with an analogous equation for the magnetic field. Applying boundary conditions to the fields at the interface, two types of solutions are obtained: one solution describes EM fields that propagate perpendicular to the interface (18) and another that describes evanescent EM fields, strongly localized at the interface, propagating in the parallel direction and decaying exponentially in the direction to the interface. If the interface is taken to be localized in the x-y plane as shown in Fig.2.2, solutions to equation (2.2) can be cast in the form

$$\begin{aligned} \vec{E}_1(\vec{r}, \omega) &= (E_{x,1}, E_{y,1}, E_{z,1}) \exp\left[i\left(\vec{K} \cdot \vec{R} + \gamma_1 z\right)\right] \quad \text{(in medium 1)}, \\ \vec{E}_2(\vec{r}, \omega) &= (E_{x,2}, E_{y,2}, E_{z,2}) \exp\left[i\left(\vec{K} \cdot \vec{R} + \gamma_2 z\right)\right] \quad \text{(in medium 2)}, \end{aligned} \tag{2.3}$$

where $E_{\alpha,i}$ are the $\alpha = x, y, z$ component in the i-th half space and where a point in space is denoted by $\vec{r} = (x, y, z) = (\vec{R}, z)$ and $\vec{R} = (x, y)$ and a temporal dependence of the type is $e^{i\omega t}$ is assumed. Similarly, a wavevector $\vec{k} = (k_x, k_y, k_z)$ is denoted by $\vec{k} = (\vec{K}, \gamma)$, where $\vec{K}$ is the component parallel to the interface and $\gamma = k_z$ the component in the z direction. Considering a EM wave of frequency ω, the quantity $k_0 = \omega/c$ can be defined where c is the speed of light in vacuum. The terms γ_1 and γ_2 can be written as

$$\begin{aligned} \gamma_1^2 &= \epsilon_1 \mu_1 k_0 - \vec{K}^2 \quad , \\ \gamma_2^2 &= \epsilon_2 \mu_2 k_0 - \vec{K}^2 \quad . \end{aligned} \tag{2.4}$$

For simplicity, we assume a non magnetic media $\mu_1 = \mu_2 = 1$, and a p-polarized external EM wave, with wavevector localized in the y-z plane. Eq. (2.3) takes the form

$$\begin{aligned}\vec{E}_1(\vec{r},\omega) &= (0, E_{y,1}, E_{z,1}) \exp\left[i\left(\vec{K}\cdot\vec{R} + \gamma_1 z\right)\right], \\ \vec{E}_2(\vec{r},\omega) &= (0, E_{y,2}, E_{z,2}) \exp\left[i\left(\vec{K}\cdot\vec{R} + \gamma_2 z\right)\right],\end{aligned} \tag{2.5}$$

Surface modes are obtained when condition with $\mathrm{Im}(\gamma_j) > 0$ is satisfied, so that the electric field decays exponentially as distance from the interface increases. Applying boundary conditions, i.e., continuity of the tangential electric field yields and the z component of $\vec{D}$

$$\begin{aligned}E_{x,1} &= E_{y,2} \\ \epsilon_1 E_{z,1} &= \epsilon_2 E_{z,2}\end{aligned} \tag{2.6}$$

furthermore Maxwell's equation $\nabla \cdot \vec{E} = 0$ imposes a relation between the two components of the electric field

$$(K E_{y,2} - \gamma_2 E_{z,2}) = (K E_{y,1} + \gamma_1 E_{z,1}) = 0, \tag{2.7}$$

where $K = |\vec{K}|$. Using Eqs. (2.6) and (2.7), one obtains the surface wave dispersion relation at a material vacuum interface

$$K = \frac{\omega}{c}\sqrt{\frac{\epsilon_1\epsilon_2}{\epsilon_1 + \epsilon_2}}. \tag{2.8}$$

This equation is valid for an interface between two half-spaces. The particular form of Eq.(2.8) is a consequence of the boundary conditions imposed in Eq.(2.6), illustrating how the particular characteristics of the surface waves depend on the geometric configuration of the system and on its dielectric properties. If we consider a dielectric-vacuum interface, sucha that $\epsilon_1 = 1$, the norm of $\vec{K}$ becomes very large for a frequency ω_{res}, such that $\epsilon_2(\omega_{res}) + 1 = 0$. From Eq.(2.4) it can be seen that at frequency ω_{res}, the term γ_i is imaginary. Therefore, the electric field given in Eq.(2.5) is only different from zero in the vicinity of the surface. Therefore, $\epsilon_2(\omega_{res}) + 1 = 0$ defines a condition for the existence of an evanescent mode known as a resonance condition. It is important to point out that when a surface mode is excited, the concentration of the EM field at the interface is accompanied by a strong localization of bound charges, which are due to the discontinuity of dielectric properties of the system (16).

The surface modes of a system can be excited by coupling to an external EM field, including thermal EM fields emitted by a body at a temperature above absolute zero. An example of the excitation of a surface eigenmode can be seen in the phenomena of total internal reflection of an external wave at an interface between two half-spaces with refractive indexes $m_1 = \sqrt{\epsilon_1(\omega)}$ and $m_2 = \sqrt{\epsilon_2(\omega)}$ with $m_2 < m_1$. For simplicity we consider medium

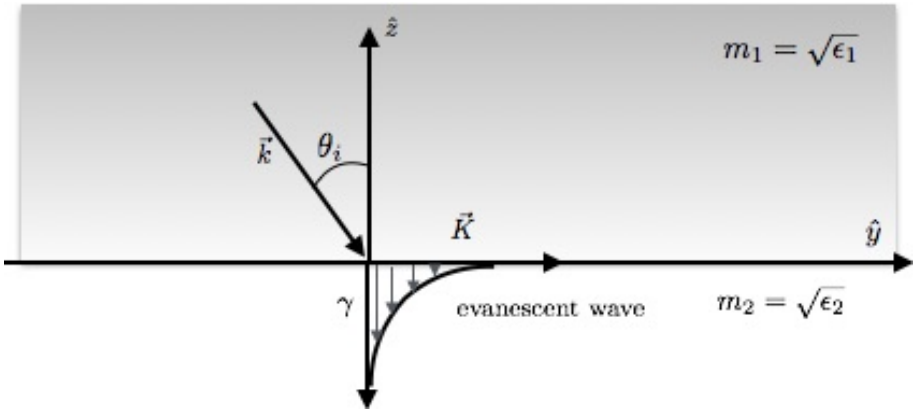

Figure 2.2: Schematic of a plane interface between two materials with dielectric function ϵ_1 and ϵ_2 and decomposition of the wavevector. Incidence of wave at an angle θ_i greater than or equal to the critical angle. The evanescent wave propagates in the y direction parallel to the interface and decays exponentially in the perpendicular direction z.

2 to be non absorbing so that m_2 is a real number. Using Maxwell's equations a relationship between the angle of incidence and angle refraction of an incident electromagnetic wave at the interface can be obtained.

$$\sin\theta_i m_1 = \sin\theta_r m_2, \tag{2.9}$$

where θ_i and θ_r are the angles of incidence and refraction respectively. From (2.9) it is seen that at an angle $\theta_r = \pi/2$ ($\sin\theta_r = 1$) the incident wave does not pass to half-space 2. This phenomena is achieved at a so called critical angle

$$\theta_i = \theta_c = \sin^{-1}\frac{m_2}{m_1}.$$

A wave traveling at an incident angle greater than or equal to the critical angle will not be transmitted to half-space 2. In these cases, the refracted wave propagates in a direction parallel to the interface and decays exponentially in the perpendicular direction as illustrated in the Fig.2.2. From Eq. (2.4) and Eq.(2.5), it can be seen that these waves decay exponentially $e^{-\gamma z}$ where z is taken perpendicular to the interface. The evanescent waves are confined to the surface since they decay rapidly in onlya few wavelengths. The localization of EM field and bound charge at the interface account for the name of surface mode. For example, in the optical spectrum glass can be characterized by a constant refractive index of $m_2 = 1.62$, while silver's refractive index will depend on the wavelength. At a glass- silver interface the average penetration distance, at which the intensity of the light decays $1/e$ from the original intensity, is158 nm for an incident wave of 532 nm (25).

Surface modes, very often play a key role in explaining many phenomena in materials science. For example, excitation of plasmon modes in metallic NPs is responsible for

phenomena such as transport and storage of EM energy (26), as well as localization and guiding of EM fields (27), and measuring intramolecular distances (28). Surface modes have been shown to influence Van der Waals forces between a molecule and an interface (21, 29). In Eq. 2.8 it was shown that at a vacuum-dielectric interface there is a resonance whenever $\epsilon = -1$. This condition coincides with resonance condition of the surface plasmon of the metal interface, so that Van der Waals forces between the molecule and interface can enhanced due to the excitation of surface waves. Excitation of surface plasmons in metals usually falls within the optical to ultraviolet spectrum; however, excitation of surface charges has been demonstrated for SiC in the infrared (30). Surface modes in dielectric crystals are typically found at infrared frequencies and are easily excited by thermal sources. Although the physical principle underlying the examples mentioned vary depending on the materials that compose the system, both can be understood in terms of the resonance of the system's surface modes.

2.2 Phonons

The importance of understanding phonon behavior stems from the fact that phonons are accountable for the infrared response in most solids; thus controlling the possible applications in the infrared range. This is particularly important when considering the interaction of a dielectric body with thermally emitted EM fields since at room temperature thermal emission is predominantly in the infrared. Phonon response is expressed in terms of the frequency dependent dielectric function of the material $\epsilon(\omega)$. Obtaining $\epsilon(\omega)$, either experimentally using infrared spectroscopy or by theoretical modeling, is of utmost importance not only for understanding interaction of matter with EM fields, but also because it impacts many of the physical properties of materials such as its thermal conductivity (31). For optical applications, a study of the physical mechanisms underlying phonon response in the infrared regime is essential.

To obtain a physical description of the lattice vibrations in solids, and how these relate to the dielectric function, a simplified model is presented. Assume that the mean equilibrium position of the i- th ion in the body is found at a lattice site $\vec{R}_n$ (32, 33). It is also assumed that the typical oscillation amplitude of each ion about the equilibrium position, u_n, is small compared to the interatomic spacing. The position of the n-th ion can be written as

$$\vec{r}_n = \vec{R}_n + \vec{u}_n$$

The potential of the system is

$$U = \frac{1}{2}\sum_{n,n'} \Phi(\vec{r}_n - \vec{r}_{n'}),$$

where we have assumed that a pair of atoms contributes an amount $\Phi(\vec{r}_n - \vec{r}_{n'})$ to the total crystal potential and where Φ is an interaction potential, for example, the Lennard-Jones potential (32). The total crystal Hamiltonian is

$$H = \sum_n \frac{P^2(r_n)}{2M} + U \tag{2.10}$$

Where $P(R)$ is the momentum of the atom whose equilibrium position is R and M is its atomic mass. Following the assumption that atoms will not substantially deviate from their equilibrium positions, and that the interaction potential acts between pairs of atoms, the potential energy U is approximated to a quadratic form $U \propto (r_n - r_{n'})^2$, using Taylor's theorem. Considering that solutions to u_n are in the form of traveling waves that propagate within the crystal with wavenumber k and frequency ω

$$u_n(t) \propto e^{i(kR_n - \omega t)},$$

a set of coupled equations for amplitudes $u_n(t)$, are obtained. To solve these equations, a set of boundary conditions must be chosen to specify how the ions at the boundaries behave. If the number of ions in the crystal is large compared to the ions at the boundaries, a convenient choice is the Born-von Karman periodic boundary conditions (32). Solving the equations for u_n, a relation for the angular frequency ω, as a function of, the wave vector $\vec{k}$ is obtained. This relation is usually referred to as the dispersion relation, and depends on the lattice symmetries and the lattice potential energy U.

It is illustrating to consider the dispersion relation of a simple case of a diatomic linear chain of atoms of mass M_1 and M_2 as shown in Figure (2.3). For this case, two dispersion relation branches are defined, known as optical and acoustic modes. Optical modes are atomic vibrations, where two different atoms in the unit cell vibrate out of phase, generating an oscillating dipole moment that can couple to an external EM field. Consequently, these modes are responsible for the optical response of a crystal. In general, the crystal must have some ionic character, such that small dipole moments within the crystal are formed, to enable the mode to couple to an external EM field.

When an EM wave passes through a polarizable medium, it couples to the induced polarizability, giving rise to a hybrid mode whose properties depend both on characteristics of the EM wave and the medium itself. A relatively simple model describing the coupling

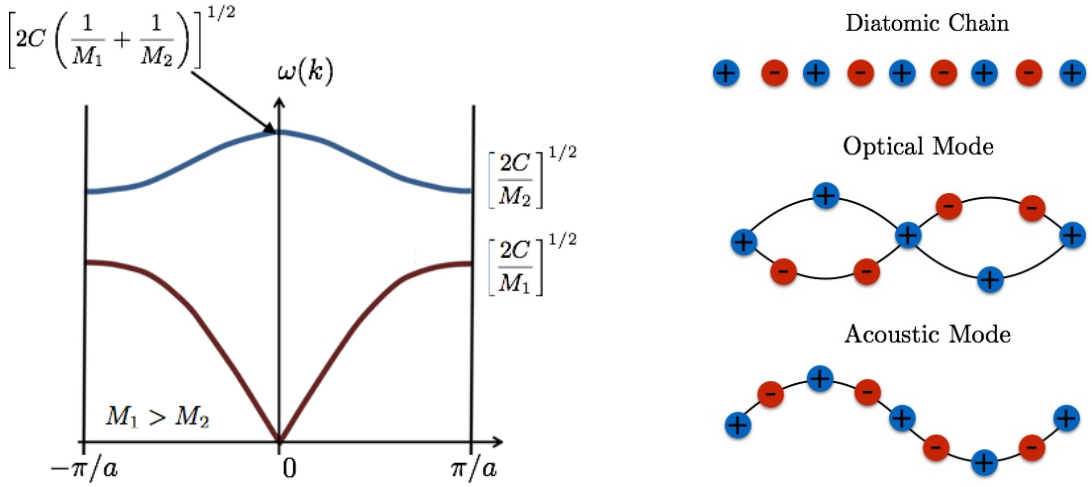

Figure 2.3: (left) Qualitative description of optical and acoustic branches of the dispersion relation for a diatomic linear lattice, showing the limiting frequencies at $k = 0$ and $k = k_{max} = \pi/a$, where C is a force constant and a the lattice parameter. (right) Transverse optical and acoustical waves in a diatomic linear lattice. Adapted from "Introduction to Solid State Physics" by C. Kittel (31).

of EM waves to phonons of a system can be established combining a harmonic oscillator for the description of mechanical waves, and the Maxwell equations for the description of EM waves. Consider an external electric field excitation which is monocromatich and spatially uniform, in $\hat{x}$ direction and of the form: $\vec{E} = E_0\hat{x}e^{-i\omega t}$, applied to the $\hat{x}$ axis of a harmonic oscillator, which in this case can represent phonon vibrations:

$$m^*\frac{d^2\vec{x}}{dt^2} + m^*\Gamma\frac{d\vec{x}}{dt} + \beta\vec{x} = -e^*\vec{E} \tag{2.11}$$

with $\vec{x}$ the displacement of the oscillator with respect to its equilibrium position, β is the restoring force per unit displacement, Γ is a damping constant, m^* and e^* are the effective mass and charge. Unlike metals and doped semi-conductors which involve free electrons, dielectrics have bound charges which experience a restoring force determined by a spring constant. As in the case of a damped harmonic oscillator, a resonant frequency exists when $\omega = \sqrt{\beta/m^*}$, which can be associated to the resonance of the optical mode ω_{TO}. Looking for solutions of the form $x = x_0e^{i\omega t}$, the displacement amplitude can be obtained

$$x_0 = \frac{eE_0}{m(\omega_{TO} - \omega - i\Gamma\omega)} \tag{2.12}$$

Associating the displacement amplitude with the dipole moment $\vec{P} = -e\vec{x}$, and using the constitutive relations $\vec{D} = \vec{E} + 4\pi\vec{P}$ and $\vec{D} = \epsilon(\omega)\vec{E}$, the lattice dielectric function follows

as

$$\epsilon(\omega) = \epsilon_\infty + \frac{Ne^2}{m\epsilon_0} \frac{1}{(\omega_{TO} - \omega - i\Gamma\omega)} \tag{2.13}$$

where N is the density of oscillators per unit volume and ϵ_∞ a high frequency the dielectric constant such that $\epsilon(\omega \to \infty) = \epsilon_\infty$. At low frequencies

$$\epsilon(0) = \epsilon_s = \epsilon_\infty + \frac{Ne^2}{m\epsilon_0\omega_{TO}}. \tag{2.14}$$

Finally, using the Lyddane-Sachs-Teller relation (33) which relates the longitudinal and transverse optical-mode frequencies to the dielectric constant $\omega_{LO}^2/\omega_{TO}^2 = \epsilon_s/\epsilon_\infty$, and follows from imposing the condition that $\epsilon = 0$ for the longitudinal mode to be consistent with $\vec{D} = \epsilon(\omega)\vec{E}$ (32). The dielectric function can be cast as

$$\epsilon(\omega) = \epsilon_\infty \left(1 + \frac{\omega_{LO}^2 + \omega_{TO}^2}{\omega_{TO}^2 - \omega^2 - i\Gamma\omega}\right) \tag{2.15}$$

In Figure(2.4) we show the dielectric function for SiC, with parameters taken from ref. (21). The peak in the imaginary part of the dielectric function corresponds to the resonant frequency of the transverse optical mode of the crystal. Adsorption in this frequency region will increase due to the excitation of this phonon mode. Under some conditions, such as the

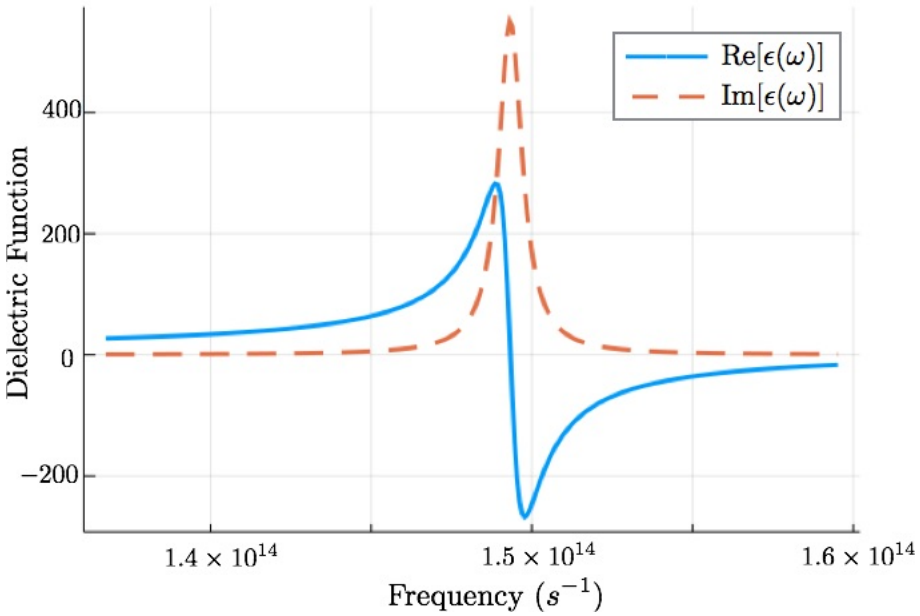

Figure 2.4: SiC dielectric functions Re[ϵ] and Im[ϵ]. Parameters taken from reference (21).

case of a dielectric interface considered in Eq.(2.8), the polarization wave associated with the polariton can be efficiently confined at the interface between two media giving rise to a surface phonon-polariton. The conditions when this occurs depend on the dielectric and geometric properties of the system (19). An important distinction is then made between

bulk polaritons, that propagate in a homogeneous medium, and surface polaritons that are confined at an interface.

2.3 Plasmon

The optical properties of metals in the visible regime are predominantly due to its conduction electrons, which act as nearly free particles. At optical frequencies, an external EM wave generates collective oscillation of its conduction electrons. The Drude model gives the most basic description of nearly free electrons in a material and describes the frequency-dependent conductivity of metals and can also be extended to free-carriers in semiconductors. This semiclassical model is obtained by applying kinetic theory to electrons in a solid, treating them much like colliding spheres, as detailed in many references (32, 33). Drude assumed the metal to be made up of a background of immobile positive ions, with a cloud of nearly free conduction electrons. Consider a free-electron gas with N carriers per unit volume, each with effective mass m and charge $-e$; the carriers are embedded in a uniform background of neutralizing positive charge. Assuming that in the whereabouts of some point x_0 , the condition $kx \ll 1$ is satisfied , the incident electric field acting on the x axis can be taken to be of the form $\vec{E}(\vec{r},t) = E_0\hat{x}\exp(-i\omega t)$ with frequency ω. The equation of motion of an electron is

$$m\frac{d^2x}{dt^2} = -\frac{m}{\tau}\frac{dx}{dt} + (-e)\vec{E}_0\exp(-i\omega t) \tag{2.16}$$

where $\vec{x}(t)$ is the position of the particle, and τ is a phenomenological relaxation time. The viscous damping term $-(m/\tau)\dot{x}$ is introduced without specifying the dissipative mechanisms; in a broad sense it is due to random collisions between the electron and whatever kind of impurities, ions, phonons and imperfections in the crystal. The displacement of an electron, with average Fermi velocity v_f, between two collisions is about the mean free path $\Lambda_f = v_f\tau$; the spatial variation of the EM field is therefore irrelevant if $\Lambda_f \ll \lambda$. For example, for Au and Ag the fermi velocity is of about 1.40×10^8 cm/sec, while there relaxation time is of the order of 10^-14s so that Λ_f can be estimated to be of the order of 10^-6cm $\approx$ nm. We can thus conclude that Eq. (2.16) is justified when this condition holds, such as is the case of the visible spectrum which is of the order of hundreds of nanometers.

Assuming a solution of the form $\vec{x}(t) = \vec{A}_0\exp(-i\omega t)$, where $\vec{A}_0$ is an oscillation amplitude, and inserting into Eq. (2.16)

$$\vec{A}_0 = \frac{e\tau}{m}\frac{1}{\omega(i+\omega\tau)}E_0\hat{x} \tag{2.17}$$

The amplitude of oscillation can be related to the current density by

$$\vec{j} = -eN\frac{d\vec{x}}{dt} = \frac{Ne^2\tau}{m}\frac{1}{1-i\omega\tau}E_0\hat{x}\exp(-i\omega t). \tag{2.18}$$

The complex conductivity is then obtained

$$\sigma(\omega) = \frac{ne^2\tau}{m}\frac{1}{1-i\omega\tau} \tag{2.19}$$

Notice that in general the conductivity $\sigma(\vec{k},\omega)$ should depend both on the frequency ω and on the wavevector $\vec{k}$ of the driving electric field;Drude theory neglects spatial dispersion and thus provides only $\sigma(k\to 0,\omega)$, also denoted $\sigma(0,\omega)$ or simply $\sigma(\omega)$. The conductiviy can be related to the dielectric function using the formula $\epsilon(\omega) = 1 + \frac{4\pi i\sigma(\omega)}{\omega}$ The obtained dielectric function is then

$$\epsilon(\omega) = 1 - \frac{\omega_p^2}{\omega(\omega + i/\tau)} \tag{2.20}$$

where $\omega_p = \frac{4\pi ne^2}{m}$, denotes the free electron plasma frequency. For ordinary metals, typical values of $\hbar\omega_p$ are in the range $[3-17]$eV while the quantity $\gamma = \hbar/\tau$ is of the order of 0.1eV.

In the study of the optical properties of free carriers in metals, we can roughly distinguish three frequency regions, called non-relaxation region $\omega \ll 1/\tau$, relaxation region $1/\tau \ll \omega \ll \omega_p$ and ultraviolet region $\omega \approx \omega_p$ and $\omega > \omega_p$. These regions are shown in Fig. 2.5. In the nonrelaxation region, at small energies, the term $\omega\tau$ is negligible compared to 1. The real part of the dielectric function is negative and tends to a constant while the imaginary part of the dielectric function is singular for $\omega \to 0$. In this regime, the reflectivity is almost 1 and the metal is strongly reflecting. In the ultraviolet regime for energies larger than, but still close to the plasma frequency, we see that $\mathrm{Re}[\epsilon(\omega)]$ is positive for $\omega \geq \omega_p$. The reflectivity changes from nearly one to almost zero, when ω is larger than the plasma frequency. The metal at these frequencies becomes transparent for $\omega > \omega_p$

The Drude model of intraband transitions describes an ideal system of free electrons, with spherical Fermi surface, a single relaxation time, in the local-response regime. Despite these restrictions, the Drude theory applies reasonably well to the description of the optical properties of many metals in the red and infrared region, sufficiently below the threshold of interband electronic transitions. However, when modeling the optical response of small metallic NPs, extra terms must be added to the Drude function to correctly describe interband transitions and spatial dispersion due to size effects of the particle, which is explained in Appendix A.

Summarizing, in this section the significance of the dielectric function and surface waves in near-field were discussed. The Drude and Lorentz models were analyzed because of their

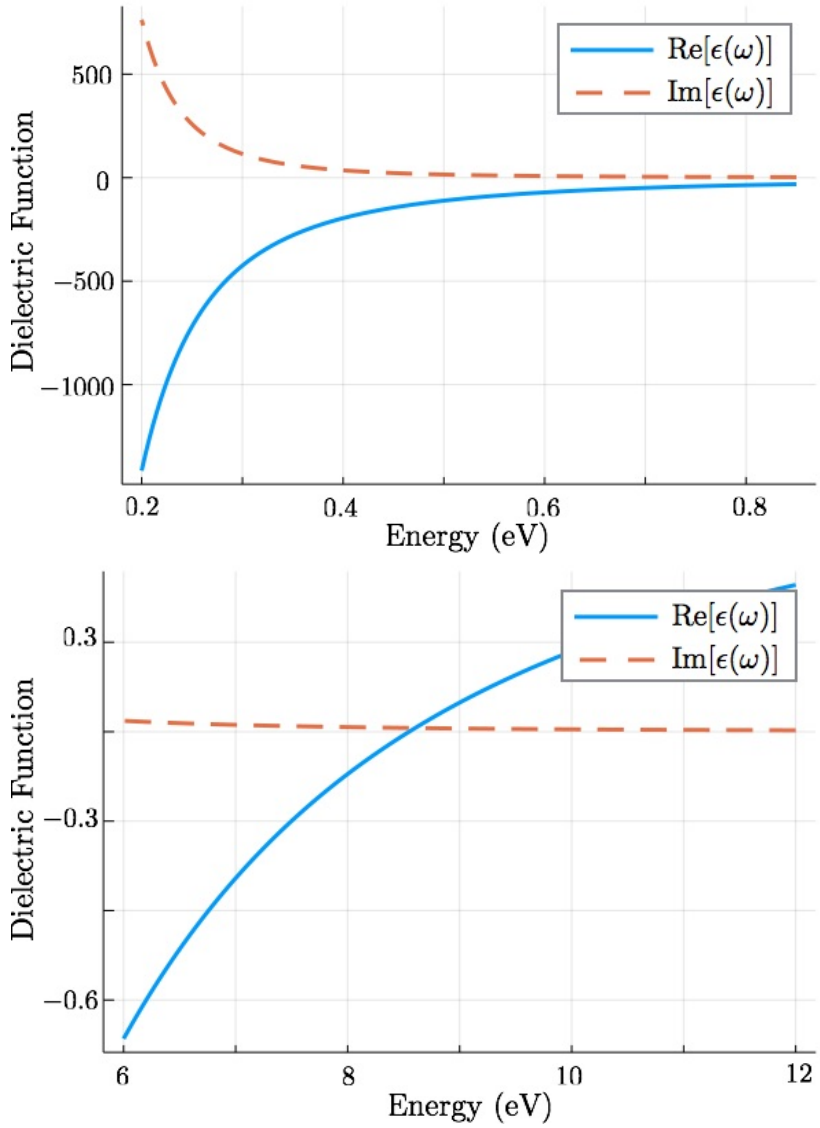

Figure 2.5: Drude dielectric functions $\mathrm{Re}[\epsilon(\omega)]$ and $\mathrm{Im}[\epsilon(\omega)]$ in the non relaxation (top) and ultraviolet region (bottom). Drude parameters for Au, $\hbar\omega_p = 8.55$ eV, $\gamma = 0.1077$

capability of describing the response of metals and dielectrics. A discussion was given on how the dielectric properties of a nanostructure determine the location of the surface modes. In the following section, the modification of surface modes due to interaction with polarizable bodies is discussed.

2.4 Surface modes in systems of interacting nanoparticles

In the case of metallic NPs, when in the presence of an external EM field, free electrons begin to oscillate and absorb energy from the field. When oscillation occurs coherently, the electronic cloud moves with respect to the positive charges of the nucleus. These oscillations generate a Coulomb attraction between positive and negative charges that acts as a restitution force, illustrated in Fig 2.6. The force generated between positive and negative charges acts against the force of the external field giving rise to characteristic resonant frequencies of the system. In the following section, we outline the principal physical concepts underlying surface modes in systems of NPs. The coupling between an EM field

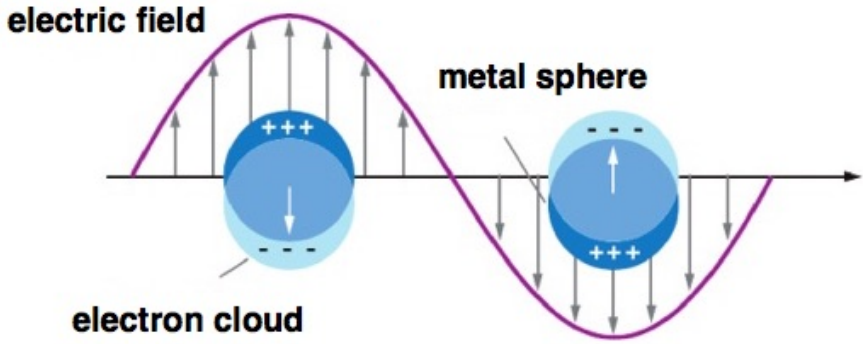

Figure 2.6: Schematic of the displacement of the electron cloud due to the interaction of a spherical metal NP with an external electric field.

and a particle is described by the particle's susceptibility, which can be written in terms of the dielectric function of the material. Within a homogeneous particle of susceptibility $\chi(\omega)$, the electric field generates a polarization field given by

$$\vec{P}(\vec{r},\omega) = \chi(\omega)\vec{E}(\vec{r}), \tag{2.21}$$

where $\vec{E}(\vec{r})$ is the field at point $\vec{r}$. Recall that the polarization field describes the dipole moment per unit volume inside the sphere. This polarization field characterizes the modes of the system.

To illustrate, consider an isolated homogeneous sphere with dielectric function $\epsilon(\omega) = 1 + 4\pi\chi(\omega)$, embedded in a matrix with dielectric constant ϵ_h, within the quasi-static approximation. When a mesoscopic particle of radius a is subject to an external field $E_{ext} = E_0\hat{e}e^{i\omega t}$ with direction $\hat{e}$, amplitude E_0 and frquency ω, a dipole moment is induced

in the sphere given by (18)

$$\vec{p}(\omega) = a^3 \left(\frac{\epsilon(\omega) - \epsilon_h}{\epsilon(\omega) + 2\epsilon_h} \right) E_0 \hat{e} = \alpha(\omega) E_0 \hat{e}, \tag{2.22}$$

where $\alpha(\omega)$ is the electric polarizability of the sphere. Notice that $\alpha(\omega)$ depends on the dielectric and geometric properties of the body and relates the external field to the dipole moment induced on the polarizable body. In contrast quantities $\epsilon(\omega)$ and $\chi(\omega)$ depend only on the material of the sphere and relate the electric field to the polarization field inside the medium. From Eq. (2.22) it can be seen that at frequencies where $\epsilon(\omega)/\epsilon_h = -2$, the denominator of the polarizability tends to zero. This resonant behavior leads to a large increase of the dipole moment induced on the sphere. Consequently, a resonant condition for a small dielectric sphere can be established whenever condition $\epsilon(\omega)/\epsilon_h = -2$ is satisfied. Due to the assumption of that the sphere is small compared to the wavelength, delay effects can be neglected and the polarization field satisfies $\nabla \cdot \vec{P} = \nabla \times \vec{P} = 0$ inside the particle, and $\nabla \cdot \vec{P} \neq 0$ on the surface (34, 35). This last condition implies that each mode has a characteristic surface charge distribution. The concentration of charge near the surface modifies the local field in the vicinity of the particle, which is the sum of the incident field and the field scattered by the dipole, denoted as $\vec{E}_s$

$$\vec{E}_{local} = \vec{E}_{ext} + \vec{E}_s. \tag{2.23}$$

The field scattered by the induced dipole at position $\vec{r}$ in the vicinity of the particle, can be written $\vec{E}_s \propto \vec{p}$ (18). Excitation by an external field at the resonant frequency will make the induced dipole moment increase, therefore increasing the magnitude of the scattered field $|\vec{E}_s|$. By defining an enhancement factor as $|\vec{E}_{local}|^2/|\vec{E}_{ext}|^2$ and using Eq.(2.22) we obtain

$$\frac{|\vec{E}_{local}|^2}{|\vec{E}_{ext}|^2} \propto |1 + \alpha(\omega)|^2. \tag{2.24}$$

It can be concluded that when a resonant mode of the sphere is excited, the enhancement of the electric field in its vicinity is maximum.

Resonant frequencies of a system can also be determined indirectly, by calculating the absorption spectrum and associating a resonant mode with the intensity peaks in the spectrum. In the case of small particles, the absorption coefficient is given by (36)

$$C_{\text{abs}}(\lambda) = \frac{4\pi\sqrt{\epsilon_h}}{\lambda} \text{Im}[\alpha(\lambda)] \tag{2.25}$$

where λ is wavelength of the exciting EM wave. From Eq.(2.25) it can be seen that the resonant condition of the particle will appear as a peak in the absorption spectrum. In

Fig.2.8 we show the peak in absorption and enhancement of the EM due to the excitation of an isolated particle. In general, the number, frequencies, and intensity of the resonant modes of a particle are determined by the dielectric, geometric and physical environment of the system such as interaction with other polarizable objects (14).

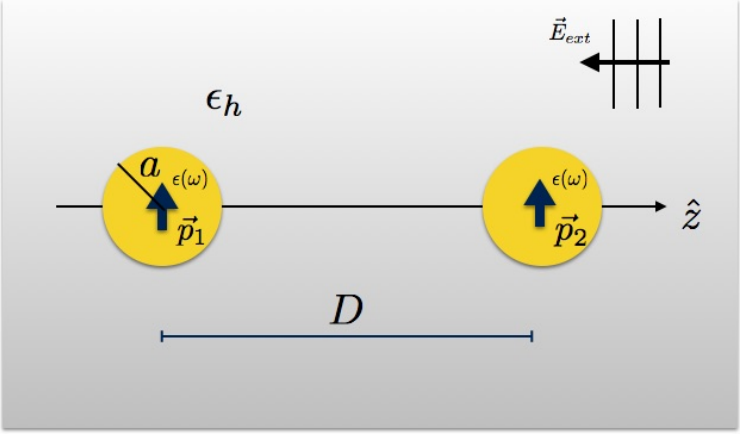

Figure 2.7: Schematic of two interacting nano spheres modeled as point dipoles, in the presence of an external field $\vec{E}_{ext}$.

In this work, we focus on the modification of a system's resonant modes, and optical properties, due to the interaction between particles. Physically, this modification is due to interaction between charge distributions in each particle. As a consequence, the resonant frequency and the ability to localize the EM field will depend on the configuration of the system such as particle radius and separation distance. To illustrate, the surface modes of an isolated particle are compared to those of an interacting dimer in vacuum, as shown in Fig.2.8. The particles are taken to be spheres of radius a separated a distances D, and modeled as interacting point dipoles in the quasistatic approximation in the presence of an external field $\vec{E}_{\text{ext}}$ with an EM response described by $\alpha(\omega)$ given in Eq.(2.22). The axis that joins the center of the spheres is aligned with the z-axis such that the vector that joins the centers of each sphere is $\vec{r} = D\hat{z}$. First, consider the case of an isolated particle in the presence of an external field, which is recovered when $D \to \infty$ and interaction is negligible. In this case, the induced dipole moment on the sphere is given by Eq.(2.22). The resonance condition is found when $\epsilon(\omega) = -2$, where the host mediums is take as $\epsilon_h = 1$. It is important to point out that in the case of an isolated sphere and due to the particle symmetry, Eq.(2.22) describes a triply degenerate resonant mode. Put in other words, the same resonant frequency is obtained for the three different possible orientations of the electric field $\vec{E}_{ext}$. As separation distance between particles decreases, it is expected that interaction between them will partially remove the degeneracy of surface modes. To

describe this at a first approximation, we consider dipole interactions. When interaction is non-negligible the induced dipole in particle i will depend on the local field, which is a sum of the external field and that produced by the neighboring particle. This interaction can be described as

$$\begin{aligned}\vec{p}_1(\omega) &= \alpha_1(\omega)\left[\vec{E}_{\text{ext}}(\omega) + \mathbf{T}_{12}\cdot\vec{p}_2(\omega)\right] \\ \vec{p}_2(\omega) &= \alpha_2(\omega)\left[\vec{E}_{\text{ext}}(\omega) + \mathbf{T}_{21}\cdot\vec{p}_1(\omega)\right],\end{aligned} \tag{2.26}$$

where $\mathbf{T}_{ij}$ are 3×3 coupling matrix given by

$$\mathbf{T}_{ij} = \frac{3\vec{r}\otimes\vec{r} - r^2\mathbf{I}}{r^5}. \tag{2.27}$$

This description is valid when both the size of the particles and their separation distances are small compared to the wavelength of the exciting field, but large compared to the particle radius (1, 37). Notice that the interaction matrix $\mathbf{T}_{ij}$ only depends on the separation distance. Considering identical particles, $\alpha_1 = \alpha_2 = \alpha$, we can solve for the induced dipole moments on particle 1

$$\begin{pmatrix} p_{1x} \\ p_{1y} \\ p_{1z} \end{pmatrix} = \begin{pmatrix} \frac{\alpha(\omega)}{1+\frac{\alpha(\omega)}{D^3}} & 0 & 0 \\ 0 & \frac{\alpha(\omega)}{1+\frac{\alpha(\omega)}{D^3}} & 0 \\ 0 & 0 & \frac{\alpha(\omega)}{1-\frac{2\alpha(\omega)}{D^3}} \end{pmatrix} \begin{pmatrix} E_{\text{ext,x}} \\ E_{\text{ext,y}} \\ E_{\text{ext,z}} \end{pmatrix}. \tag{2.28}$$

By looking at Eq.(2.28), a number of things can be said about the modification of resonant modes, due to dipole interaction, compared to the isolated case. First, we can identify an effective polarization in each direction given by $\alpha_x = \alpha_y = \frac{\alpha(\omega)}{1+\frac{\alpha(\omega)}{D^3}}$ and $\alpha_z = \frac{\alpha(\omega)}{1-\frac{2\alpha(\omega)}{D^3}}$. Resonant conditions will be obtained when the denominator of the effective polarizability goes to zero. These conditions are modified with respect to the case of an isolated, $\epsilon(\omega^{res}_{isol}) = -2$ sphere, and can be simplified to

$$\begin{aligned}\epsilon(\omega^{res}) &= -\frac{16\sigma^3 - 1}{8\sigma^3 + 1} \qquad \text{in the x-y direction} \\ \epsilon(\omega^{res}) &= -\frac{16\sigma^3 - 1}{8\sigma^3 - 1} \qquad \text{in the z direction,}\end{aligned} \tag{2.29}$$

where $\sigma = D/2a$. Second, due to interaction resonant conditions for the x, y excitations are degenerate, while the mode in the z direction is non degenerate. This causes the breaking of symmetry due to the dimer configuration. As particle separation decreases, shift in the resonant condition is larger, while as $D \to \infty$, the resonant conditions for all modes tend to that of the isolated sphere $\epsilon = -2$. This tendency can be observed indirectly by calculating

the absorption spectrum using Eq.(2.25). The absorption cross section for a Ag dimer of particles with 12 nm radius is shown in Fig.2.8. The absorption peak is seen to move from to larger wavelengths as the separation distances increases.

Furthermore, once induced dipoles are obtained, it is possible to calculate the electric near-field scattered by each particle. This can be found using (18)

$$\vec{E}_{\mathrm{s}}(\vec{r}) = \sum_{i=1}^{2} \frac{3\hat{n}(\vec{p}_i \cdot \hat{n} - \vec{p}_i)}{|\vec{x} - \vec{x}_i|^3} \tag{2.30}$$

where $\vec{x}_i$ is the location of particle i and $\hat{n}$ is a unit vector directed from $\vec{x}_i$ to $\vec{x}$. The induced field is directly proportional to the induced dipole moment, and an increase in field enhancement is expected at the resonant frequency of the system as can be seen in Fig.2.8. The symmetry of the induced field, as well as its intensity is modified due to interaction when compared to the case of an isolated particle.

This particular example allows an analytic description of the interaction and field enhancement of two spherical particles in the presence of an external homogenous EM field and illustrates the modification of the system's surface modes with the geometric parameters of the system. However, exact solutions of Maxwell's equations for particles in the presence of EM fields exist only for simple geometries such as spheres, spheroids, and infinite cylinders. For more complex systems, obtaining the optical response of a system requires numerical methods such as those based on finite differences(38) or the discrete dipole approximation(39), to mention some. In the following section, we present an analytical method that allows the calculation of the optical response and electric near-field due to a collection of spherical particles.

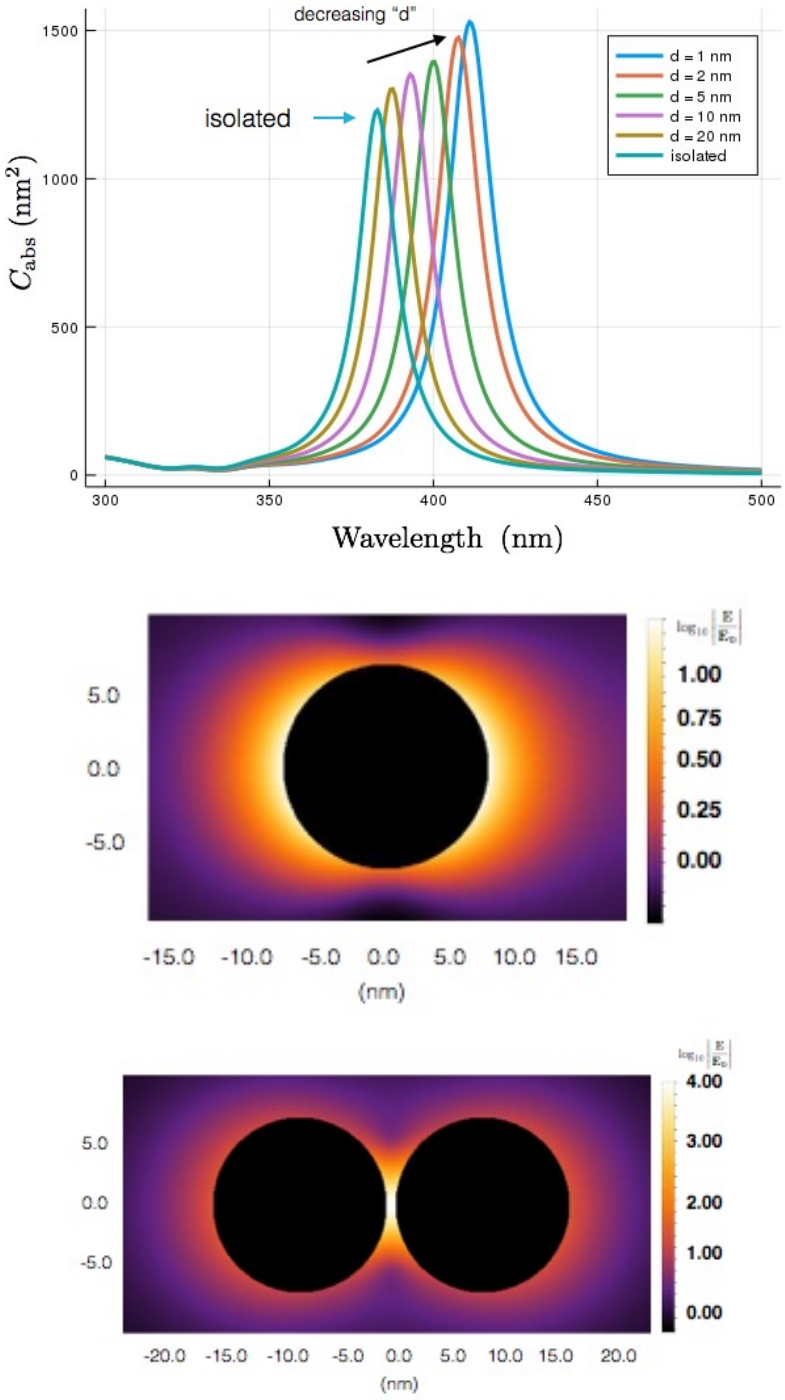

Figure 2.8: Absorption spectrum of two Ag nanoparticles of a = 12 nm for different gap separation, where center to center separation is given as $R = 2a + d$. The case of an isolated particle is also shown (top). Electric field enhancement of the isolated particle and the interacting particles separated by 1 nm (bottom).

Part I

Optical Properties of Interacting Metallic Nanoparticles

Chapter 3

Introduction

3.1 Background

It is known that nanostructured materials possess very distinct optical response when compared to their bulk properties. People had exploited this phenomenon long before it was understood. The bright and fascinating colors of noble metal NPs have attracted considerable interest since historical times as decorative pigments in stained glasses and artwork. In modern times, rapid advances in nanostructure synthesis and fabrication (40) have brought the study of the optical properties of nanostructured systems to the forefront of nanotechnology research, leading to possible applications ranging from photonics (41) to biomedicine (42). In Chapter 2, the optical response of nanostructured systems was discussed in terms of the excitation of localized surface modes, appearing in the extinction cross-section spectrum as peaks at discrete wavelengths. A description of was given of how surface modes determine a system's optical properties, such as the location of its resonant frequencies, absorption properties, field enhancement, etc..

This part of the work is focused on surface plasmons in metallic NPs. In particular, Ag and Au have been the subject of a large part of plasmonics research because they support high-quality plasmon resonances at the optical spectrum, and within this spectral range can be designed to produce resonances at any desired frequency. This is in part due because losses in silver and gold are relatively low compared to other metals. Copper, for example, can also support plasmon resonances at optical frequencies, but these resonances are weak because losses in the metal rapidly dissipate the plasmons. Silver has the lowest losses, and thus the strongest plasmon resonances, of all known materials. However, for practical applications, Au is more stable than silver, so it is often used instead (43). Other materials can produce plasmon resonances in other frequency ranges; aluminum, for example, supports plasmons at ultraviolet frequencies, but this work limits the study to plasmons at

optical and near-optical frequencies.

At the nanometric scale, the surface modes of a system are determined by the material and the geometrical structure, as well as on the interaction with its surroundings(37). This dependence allows the tailoring of the optical properties of a system for particular purposes. The dependence on particle shape has been studied in detail in previous work, including the cases of cubes, spheroids, icosahedrons, octahedral, wedges and coated NPs (14, 34, 37, 44, 45). For example, dependence on particle morphology, including truncated cubes, icosahedral and spheres, was thoroughly studied in Ref. (44) using a discrete dipole approximation. Authors found that as truncation of a cube increases, the main resonance is always blue-shifted and the width of the main SPRs decreases. Furthermore, it has been demonstrated that sharp points result in a larger concentration of fields (45). This nanoscale confinement of light does far more than merely reduce the size of optical components: it dramatically increases the interaction between light and matter. For instance, metal NPs focus light down to spots hundreds of times smaller than any ordinary lens; the light will thus interact with the material in that spot thousands or millions of times more strongly than it otherwise would. Consequently, effects that would previously be observable only with specialized, high power lasers can be reached with more conventional light sources.

Similarly, the sensitivity of surface modes to the body and host dielectric properties has also been exploited to tailor the optical properties of the system for specific purposes, as shown in Fig. 3.1. In metals, the density of conduction electrons partially determines the location of the resonant frequency: the larger the density involved in a plasmon oscillation, the higher the electrostatic restoring force, and thus the higher the resonant frequency. Partial screening due to the host mediums shifts the resonance frequency allowing the tailoring of resonances at any desired frequency within the optical range. Additionally, as was shown in Chapter 2, plasmons in separate NPs couple together when the particles are brought close to one another, leading to further shifts of the resonance to lower frequencies and further concentration of fields to small volumes. Design of nanostructured systems thus allows plasmon resonances to be tuned to match a given optical frequency and makes it possible to confine optical fields in three dimensions to length scales of only a few nanometers (46, 47).

This nanoscale control over light opens up many technological opportunities. To cite a few examples, plasmon resonances in metal nanoparticles allow for highly sensitive chemical sensing and identification, down to the level of single molecules. Luminescence from molecules or semiconductor nanostructures can be enhanced by nearby metal NPs, poten-

tially enabling a new generation of light-emitting devices (48). Metal NPs can reduce the size, and thus increase the performance, of photodetectors, and may improve the efficiency of solar-energy conversion (49). Metal NPs with resonances in the near infrared can be functionalized to attach to cancer cells selectively; illumination of these nanoparticles with resonant light heats the particles, eliminating tumors without damaging nearby tissue (50). The strong local electric field resulting from the excitation of a surface mode has been used, for example in metal plasmon enhanced fluorescence (51), which has a demonstrated utility in surface-enhanced Raman scattering (SERS) with enhancement factors large enough to possibly allow single molecule detection (48). Tunable absorption and scattering of noble metal nanocrystals have made them a novel class of optical and spectroscopic tags for biological sensing and imaging (52). Optical tuning obtained by combining materials with different electric permittivities in complex arrays leads to the development of metamaterials and photonic/plasmonic crystals, which allow the engineering of the optical response by tailoring the photonic energy bands (53). Metamaterials use non-diffractive arrays of coupled resonant nanoscatterers sustaining magneto-electric resonances (54) to achieve negative refraction (55, 56, 57), resonant absorption (58), cloaking (59). On the other hand, lattices of plasmonic structures, or photonic crystals, sustain hybrids photonic-plasmonic modes arising from the interaction of long-range radiative coupling of resonant scatterers and localized surface plasmons. These structures have been used, for example, to control the light emission of the photonic crystals (60, 61, 62).

3.2 Motivation

In section 2.4, the optical response of a dimer of nanospheres was modeled by point dipoles. The response of the system could be characterized by the induced dipole moments in each particle. In general, the optical response of a nanostructure can be classified in terms of the symmetry of the induced charge distribution, or multipolar charge distribution. The relevance of a multipolar response was already clear from the solution, found by Mie, to the problem of a metallic sphere illuminated by a plane wave when the long-wave condition is not met, further generalized to the case of aggregates of non-identical spheres. Multipolar resonances for many other geometries such as cubes, nanowires, nanorods, and dimers have also been studied (63), and have been shown to exist even in the long-wavelength limit (64). Electric quadrupoles and octupoles moments, and magnetic dipoles also emerge in plasmonic lattices and assemblies of nanoparticles where they give rise to bright and dark

modes and are responsible for phenomena such as electromagnetically induced transparency (65, 66), lasing (67), superradiance (68, 69) and non-linear effects (70). Furthermore, by coupling the external field to the different modes of the system, it is possible to modify the symmetry and spatial distribution of the total electric field intensity in the system, which can be useful to focus light and localize energy to subwavelength hot spots (45, 46). Strong field gradients associated with high order multipoles can be also beneficial for optical tweezing (71).

Rational design of resonant nanostructures is typically achieved by varying the geometrical parameters and composition of the system (14, 72). The efficiency of the optical resonances is predetermined by the geometrical parameters of the system, such as lattice constant, dimensions and shape of the scatterers. Therefore, after the fabrication no active control on the optical response is possible. Recently it has been proposed and experimentally demonstrated that structuring the incident field leads to an externally tuneable, dramatic change in the optical response of the illuminated object (73). However, little attention has been paid to the relation between the symmetry of the incident field and the resulting excitation of the resonances of a system (62, 74). Different methods have been introduced to achieve this, such as wavefront shaping (75) and coherent control of absorption and scattering via multiple beam illumination. (76, 77) Polarization of the incident light also plays an essential role in selecting the available modes of the nanostructure (74, 78).

The combination of the geometrical design of the nanostructure with a proper symmetry of the illumination field can result in an intriguing additional degree of freedom to tailor the optical response of nanostructures which has not been sufficiently studied. In the following section, we propose a general analytical model able to compare and isolate the contributions of the geometry, dielectric response and excitation field in the extinction cross-section. The method quantifies the coupling strength of the incident field to a specific multipolar resonance in the quasi-static limit. To present the method, we make use of a dimer of metallic nanospheres placed in proximity to each other, the most straightforward system used in the generalized multiparticle Mie (GMM) solution and the technique developed in Refs. (74, 79). However, our method shows how specific plasmonic multipolar modes are excited by using a spatially non-uniform incident field. Our method fills the gap between other solutions valid for nanospheres of arbitrary dimension but placed at arbitrary distances and in the presence of a spatially uniform incident field. Our method adequately accounts for Coulomb interactions and evanescent fields between the particles which are responsible for the excitation and the mutual coupling of multipoles under uniform and

non-uniform incident fields.

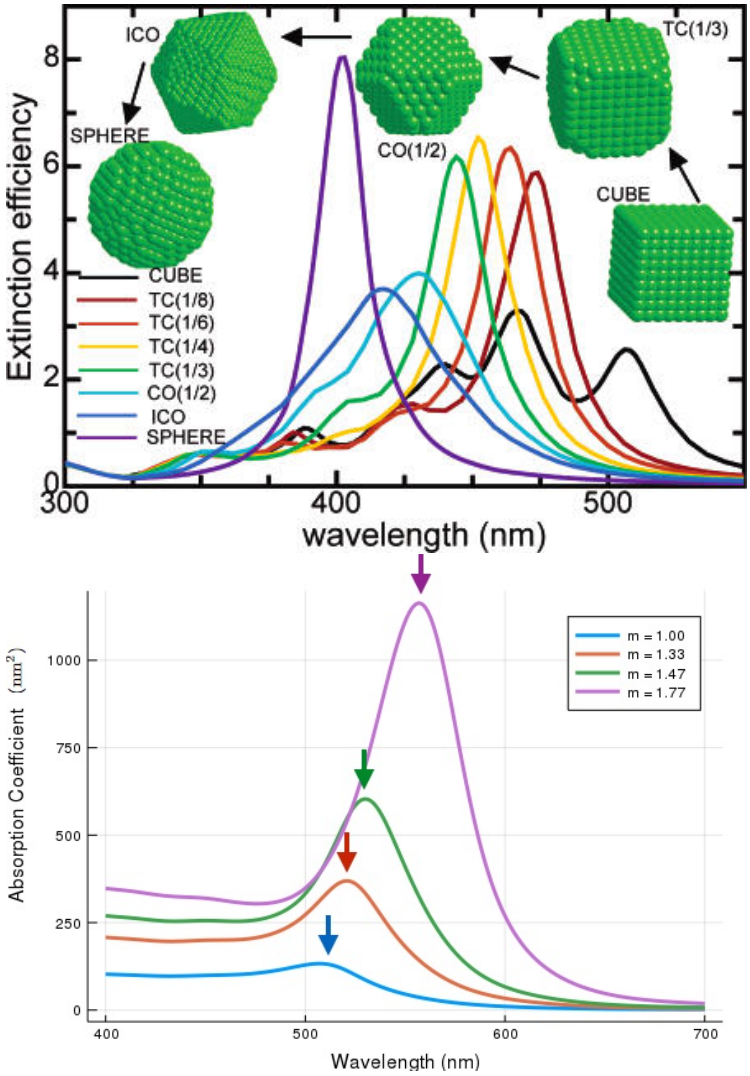

Figure 3.1: (top) Extinction efficiency for silver NPs with varying shape, in host medium $m_h = 1.47$. Image taken from Ref. (37) .(bottom) Absorption efficiency for 10 nm isolated spherical Au NPs with varying host medium $m_h = 1.00, 1.33, 1.47, 1.77$ corresponding to vacuum, water, dimethyl sulfoxide or silica glass and sapphire .

Chapter 4

Spectral Representation Method

The spectral representation (SR) is a formalism that allows the calculation of plasmonic resonances of a system separating its geometric and dielectric properties which was introduced by R. Fuchs (34) who showed that the effective polarizability of a system composed of polarizable entities can be written as a sum over its normal modes

$$\alpha(\omega) = -\frac{v}{4\pi}\sum_{s}\frac{C(s)}{u(\omega)-n_s}, \tag{4.1}$$

where $C(s)$ are real values, n_s the eigenvalue of mode s, v the particle volume and $u(\omega)$ is a complex spectral variable defined by

$$u(\omega) = \frac{1}{1-\epsilon(\omega)/\epsilon_h},$$

where $\epsilon(\omega)$ is the dielectric function of the particles and ϵ_h the dielectric constant of the medium. Fuchs also showed that eigenvalues n_s satisfy

$$0 < n_s < 1,$$

and that $C(s)$ is a real term that satisfies the sum rule

$$\sum_{s} C(s) = 1, \tag{4.2}$$

such that $C(s)$ can be interpreted as the coupling weights of s mode to the external field. Eq. (4.1) allows calculation of the optical response of the system, separating geometrical parameters such as $C(s)$ and n_s, and dielectric parameters $u(\omega)$. In the case of small particles, the polarizability is related to the absorption cross section $\mathrm{C_{abs}}$ of the system by means of (14, 36)

$$\mathrm{C}_{abs} = \frac{8\pi^2 m_h}{\lambda}\mathrm{Im}[\alpha](\omega)], \tag{4.3}$$

where $m_h = \sqrt{\epsilon_h}$ is the refraction index and $\lambda = 2\pi c/\omega$ is the wavelength of the incident field in vacuum. By separating the imaginary part of Eq. (4.1)

$$\mathrm{Im}\left[\alpha(\omega)\right] = \frac{v}{4\pi}\sum_{s}\frac{C(s)u_2(\omega)}{(u_1(\omega)-n_s)^2+u_2^2(\omega)}, \tag{4.4}$$

where u_1 and u_2 are the real and imaginary part of the spectral function. From Eq.(4.4) it is observed that there are poles in the polarizability of the system, which correspond to peaks in the absorption cross section, found when

$$u_1(\omega) = n_s \qquad \text{and} \qquad u_2 \ll 1. \tag{4.5}$$

Eq.(4.5) defines resonant conditions of the system. For a given resonance, absorption cross-section will be given by a single term in the sum (4.4)

$$\mathrm{C}_{abs} \propto \mathrm{Im}[\alpha(\omega)] = \frac{vC(s)}{u_2(\omega)}, \tag{4.6}$$

so that it will be more intense when the coupling weight of the mode is large and the imaginary part of the spectral variable is small (14). Eq. (4.1) is applicable for any system, allowing the identification of the surface modes of a system by separating its geometric and dielectric properties. However, the explicit form of $C(s)$ and n_s depends on the system under consideration. In the following section, we present a methodology to obtain the effective polarizability of a system of spheres interacting through Coulomb forces.

4.1 Multipolar spectral representation

Consider the case of a system of N non-overlapping dielectric spheres located in positions $\vec{R}_i$ with $i = 1, 2..., N$, of the same radius a in the presence of an external electric field. The spheres dielectric properties are described by a frequency dependent complex dielectric function $\epsilon(\omega)$ and are embedded in a non-absorbing matrix with dielectric constant ϵ_h. The multipolar moment of order lm induced in particle i -th, located in the position $\vec{R}_i$ is written as

$$Q_{lmi} = -\frac{2l+1}{4\pi}\alpha_{lmi}(\omega)V_{lm}(i), \tag{4.7}$$

where $\alpha_{lmi}(\omega)$ is the multipolarizability and $V_{lm}(i)$ is the lm-th term of the expansion of the local potential, which consists of the external potential and a term due to the multipolar charge distributions induced on the other spheres

$$V_{lm}(i) = V_{lm}^{ext}(i) + \sum_{j\neq i} V_{lm}^{j}(i), \tag{4.8}$$

where term V_{lm}^{ext} is the external potential, $V_{lm}^{j}(i)$ describes the potential generated in the particle i by the multipoles of the particle j. This interaction term can be written as

$$V_{lm}^{j}(i) = \sum_{l'm'} A_{lmi}^{l'm'j} Q_{l',m'j}$$

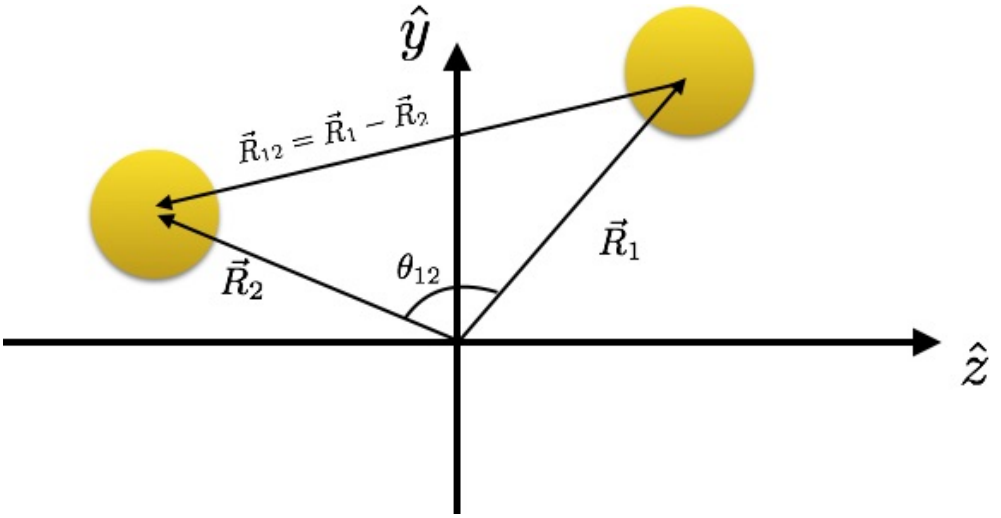

Figure 4.1: Schematic of a configuration of two spherical NPs showing the definition of vectors $\vec{R}_{12}$ and the corresponding angle θ_{12}

where $A_{lmi}^{l'm'j}$ is a coupling matrix that allows the potential in i to be expanded in terms of the multipolar charge distribution found in particle j. The induced charge in particle i, whose multipolarizability is $\alpha_{lm,i}(\omega)$ is written as

$$\begin{aligned} Q_{lmi} &= -\frac{2l+1}{4\pi}\alpha_{lm,i}(\omega)V_{lm}(i) \\ &= -\frac{2l+1}{4\pi}\alpha_{lm,i}(\omega)\left[V_{lm}^{ext} + \sum_{l'm'j} A_{lmi}^{l'm'j}Q_{l'm'j}\right], \end{aligned} \tag{4.9}$$

For this system it is convenient to use spherical coordinates, so that the lm-th moment on the i -th sphere located at the position R_i is defined as

$$Q_{lmi} = \int_v |\vec{r} - \vec{R}_i|^l \rho(\vec{r} - \vec{R}_i) Y_{lm}^*(\theta, \phi) d^3r \tag{4.10}$$

where $\rho(\vec{r} - \vec{R}_i)$ is the induced charge on the i-th sphere, $Y_{lm}(\theta, \phi)$ are the spherical harmonics of order lm; θ, ϕ are the angles given by $\hat{r}_i = (\vec{r} - \vec{R}_i)/|\vec{r} - \vec{R}_i|$, and the integral is carried out over spheres volume v_s.

Components of the coupling matrix written in spherical coordinates are (80)

$$\begin{aligned} A_{l'm'j}^{lmi} &= (-1)^{m'} \frac{\left[Y(\theta_{ij}, \phi_{ij})_{l+l'}^{m-m'}\right]^*}{R_{ij}^{l+l'+1}} \times \\ &\times \left[\frac{(4\pi)^3}{(2l+1)(2l'+1)(2l+2l'+1)} \frac{(l+l'+m-m')!(l+l'-m+m')!}{(l'+m')!(l+m)!(l'-m')!(l-m)!}\right]^{1/2}, i \neq j \end{aligned} \tag{4.11}$$

where $\vec{R}_{ij} = \vec{R}_i - \vec{R}_j$ is the vector that joins the center of particle i and j, and θ_{ij} and ϕ_{ij} are the spherical angles corresponding to $\vec{R}_{ij}$. Note that this matrix only depends on

geometric parameters of the system such as the distance and angles between particles and radii of the spheres. It has been shown that the matrix $A^{lmi}_{l'm'j}$ is a hermitian matrix (80). Due to symmetry of the particle, multipolarizability α_{lmi} in the quasi-static approximation does not depend on the m index (81)

$$\alpha_l = \frac{l(\epsilon(\omega) - \epsilon_h)}{l(\epsilon(\omega) + \epsilon_h) + \epsilon_h} a^{2l+1} = \frac{n_{0l}}{n_{0l} - u(\omega)} a^{2l+1}, \tag{4.12}$$

where $n_{0l} = \frac{l}{2l+1}$ and ϵ_h is the dielectric constant of the host matrix. The expression (4.9) defines the system of equations that must be solved to obtain the multiples induced in the spheres. Thus, replacing (4.11) and (4.12) in (4.10) gives you a system of equations for moments Q_{lmi}

$$\sum_{l'm'j} \left[-u(\omega)\delta_{ll'}\delta_{mm'}\delta_{ij} + H^{l'm'j}_{lmi} \right] x_{l'm'j} = f_{lmi}, \tag{4.13}$$

where $u(\omega)$ is a spectral variable, $\delta_{\alpha\beta}$ the Kronecker delta and

$$x_{lmi} = \frac{Q_{lmi}}{(la_i^{2l+1})^{1/2}}, \qquad f_{lmi} = -\frac{(la_i^{2l+1})^{1/2}}{4\pi} V^{ext}_{lm},$$

$$H^{l'm'j}_{lmi} = n_0^l \delta_{ll'}\delta_{mm'}\delta ij + (-1)^{l'} \frac{(ll' a_i^{2l+1} a_j^{2l'+1})^{1/2}}{4\pi} A^{l'm'j}_{lmi}, \tag{4.14}$$

This can be written In matrix notation as

$$[-u(\omega)\mathbf{I} + \mathbf{H}]\, \vec{\mathrm{X}} = \vec{\mathrm{F}}, \tag{4.15}$$

where $\mathbf{H}$ is a hermitian matrix, $\mathbf{I}$ is the identity matrix , and $\vec{X}$ and $\vec{F}$ are vectors. A method to solve this type of equations is through the Green function which is outlined in Appendix C. A solution can be found by diagonlazing matrix $\mathbf{H}$, so that

$$\vec{X} = (-u(\omega)\mathbf{I} + \mathbf{H})^{-1}\vec{F} = \mathbf{G}(\omega)\vec{F},$$

where $\mathbf{G}(\omega)$ is the Green matrix corresponding to Eq.(4.15). Matrix $\mathbf{G}$ is written in terms of the unitary matrix $\mathbf{U}$ which diagonalizes $\mathbf{H}$, so that

$$\mathbf{UHU}^{-1} = \mathbf{n},$$

where $\mathbf{n}$ is a diagonal matrix whose components n_{lmi} are eigenvalues of $\mathbf{H}$. The Green matrix can be written as

$$\mathrm{G}^{\mu' i'}_{\mu i} = -\sum_{\mu'' i''} \frac{\mathrm{U}^{\mu'' i''}_{\mu i} (\mathrm{U}^{-1})^{\mu' i'}_{\mu'' i''}}{u(\omega) - n_{\mu'' i''}} = -\sum_{\mu'' i''} \frac{\mathrm{C}^{\mu' i'}_{\mu i, \mu'' i''}}{u(\omega) - n_{\mu'' i''}}, \tag{4.16}$$

where we use μ for the set of indexes (l, m) and, where the terms $\mathrm{C}^{\mu' i'}_{\mu i, \mu'' i''} = \mathrm{U}^{\mu'' i''}_{\mu i} (\mathrm{U}^{-1})^{\mu' i'}_{\mu i''}$ are the coupling weights of the external field with the μi mode. In accordance with Eqs. (4.2) and (4.6), the terms $\mathrm{C}^{\mu' i'}_{\mu i, \mu'' i''}$ describe the coupling of the μ' term of the external field to the μ-th multipole moment and satisfy the sum rules (34)

$$\sum_{\mu'' i''} \mathrm{C}^{\mu' i'}_{\mu i, \mu'' i''} = \delta_{\mu i, \mu' i'} \tag{4.17}$$

Using the Green matrix, the induced multipoles can me obtained

$$Q_{\mu i} = -(l a^{2l+1})^{1/2} \sum_{\mu'' i''} \frac{\mathrm{C}^{\mu' i'}_{\mu i, \mu'' i''}}{u(\omega) - n_{\mu'' i''}} f_{\mu' i'}. \tag{4.18}$$

4.2 Optical response and near-field enhancement

Once the induced multipolar moments, Q_μ, are found, the spatial distribution of the multipolar electric near-field intensity is calculated by taking minus the gradient of the electric potential outside of the nanospheres:

$$\mathbf{E}(\mathbf{r}) = -\nabla \left[\sum_{\mu} g_\mu(\mathbf{r}) Q_\mu \right], \tag{4.19}$$

where components of the spatial function $g_\mu(\mathbf{r})$ in spherical coordinates are given by

$$g_{lm,i}(\mathbf{r}) = \frac{4\pi}{2l+1} \frac{Y_{lm}(\theta_i, \phi_i)}{|\mathbf{r} - \mathbf{R_i}|^{l+1}} \tag{4.20}$$

with (θ_i, ϕ_i) being the angles corresponding to the vector $(\mathbf{r} - \mathbf{R_i})$. For a certain multipolar excitation field, $V^{\mu'}_{ext}$, by using Eq. (4.18) the multipolar moments, Q_μ, along with their excitation efficiency coefficients, $\mathbb{C}_s$, can be obtained.

It is possible to relate the induced multipole moments with the absorption and scattering cross section of the system. This is done by noting that the scattering and absorption coefficients are written in terms of the induced dipole moments of the particles (36). These are calculated using the relations (18)

$$Q_{10} = \sqrt{\frac{4\pi}{3}} p_z$$

$$Q_{1,m=\pm 1} = \sqrt{\frac{2\pi}{3}} (p_x \mp i p_y),$$

Using Eq. (4.18) and the symmetry properties previously mentioned we write the dipole moment $(l = 0)$ for $m = 0$, along the z axis in cartesian coordinates, to obtain (18)

$$p_z(\omega) = -\sqrt{\frac{4\pi a^3}{3}} \sum_s \frac{\mathrm{C}^{l'}_{1,s}}{u(\omega) - n_s} \mathrm{F}^{l'}. \tag{4.21}$$

In this work, we consider the excitation with $l' = 1$ for the case of a dipole excitation and $l' = 2$ for a quadrupole excitation. For a given excitation l', its frequency-dependent scattering cross-section depends on the value of the induced dipole moment of the system, and can be evaluated as (18):

$$\begin{aligned} C_{\text{sca}}(\omega) &= \frac{16\pi}{3}\frac{k^4 v}{E_0^2}\left|p_z\right|^2 \\ &= \frac{16\pi}{3}\frac{k^4 v}{E_0^2}\left|\sum_s \frac{\mathrm{C}_{1,s}^{l'}}{u(\omega)-n_s}\mathrm{F}^{l'}\right|^2 \end{aligned} \tag{4.22}$$

sss

where v is the volume of the nanosphere and the term between bars is an effective Cartesian dipole moment of the system and E_0 is the magnitude of the incident field. Furthermore, from Eq. (4.22), resonance conditions can be defined when $\mathrm{Im}[u(\omega)] \simeq 0$ and $\mathrm{Re}[u(\omega)] = n_s$, from this latter the resonant frequency is found. At the resonant frequency, the intensity of the scattering cross section will depend primarily on the value of two parameters, the coupling strength and the value of $\mathrm{Im}[u(\omega)]$. Therefore, a larger value of $\mathrm{C}_{1,s}^{l'}$ and small values of $\mathrm{Im}[u(\omega)]$ cause a more intense peak in the scattering cross-section.

In principle, all the matrices in the previous equations are infinite-dimensional, $L \to \infty$ and $M \to \infty$. Since the larger l is, the weaker the coupling between multipolar moments, numerically, we introduce a cut off at $L = l_{max}$. For $l_{max} = 1$ we recover the dipole approximation, which is expected to be good only for large particle separations. For $l_{max} = 2$ the quadrupole approximation is obtained in which dipole-dipole, dipole-quadrupole, and quadrupole-quadrupole moments interactions are taken into account. In general, for a given particle separation an appropriate l_{max} must be chosen to ensure convergence of the physical properties. (14)

4.3 Method outline: optical response and near-field enhancement

In this section, we outline the procedure to obtain the optical response and near-field enhancement of a configuration of NPs utilizing the SR method.

1. Dielectric parameters: Choose the NPs and host matrix material and the corresponding model dielectric function. For metallic NPs, it is often necessary to modify the common Drude dielectric function to include dispersion effects due to interband transitions and surface scattering for particles of sizes comparable to the mean free path

of its charge carriers(47). These modifications are further explained in the Appendix A. Once the NP and host dielectric parameters are chosen, the spectral variable $u(\omega)$ can be defined.

2. Geometric parameters: The number of particles, particle radius and positions are defined. We point out that the SR allows the modeling of particles of different particle sizes, as long as radii are smaller than the exciting wavelength.

3. Calculation of geometric matrices: Once the geometric parameters are defined, the matrices **A** and **H** can be calculated using Eqs. (4.11) and (4.14) respectively. These matrices only depend on the geometric parameters of the system and are completely defined once the particle radii and positions are chosen.

4. Calculation of Green's Matrix: Once matrix **H** is obtained, its eigenvectors and eigenvalues are calculated via an eigendecomposition method.

5. Using the spectral variable, eigenvectors, and eigenvalues, Eq. (4.16) are used to calculate the Greens matrix at a given frequency. The Green matrix holds the information of the system's normal modes, and resonant frequencies of the system can be found by calculating the poles of the matrix. Using the eigenvalues obtained in the previous step and the spectral variable, resonant frequencies can be obtained using Eq.(4.5). Furthermore, coupling strengths to the external fields can be obtained using the unitary matrix that diagonalizes **H**.

6. Calculation of induced multipoles: In order to calculate the induced multipoles in the system, the form of the exciting field must be determined. The multipolar SR allows excitation by spatially homogeneous as well as multipolar fields. Once this is defined, using the Green matrix **G** and Eq.(4.18), the induced multipoles in the system can be calculated, $Q_{lm,i}$.

7. Calculation of optical response: Using the Green matrix and the induced multipoles, it is possible to define the system's polarizability. Optical properties such as the absorption cross section can be written in terms of this quantity. To obtain the absorption spectrum, steps four and five must be repeated for each frequency.

8. Calculation of scattered field: Using the calculated multipole moments and Eq. (4.19), the induced electric field can be obtained. By comparing this to the exciting field, the total local electric field, an enhancement factor can be calculated.

Chapter 5

Results

To demonstrate our method we use the archetypal system made of two identical spheres of radius a, whose centers are separated by a distance D. We take the axis that joins the centers of the spheres as the z axis. Remember that under this condition there is no coupling between multipole moments with different m index. Moreover, the sign of the multipole moments in the two identical spheres satisfy the relation (82): $Q_{lm,2} = (-1)^{l+1} Q_{lm,1}$. Therefore, by exploiting symmetry, equations for the multipolar moments can be considerably simplified. Additionally, the high symmetry of our system allows us to parameterize the solution regarding only one geometrical parameter, defined in terms of center to center separation distance D, and the particle radius a, as $\sigma = D/2a$. Defined in this manner, when the spheres are in contact $D = 2a$ and $\sigma = 1$, as separation distance increases σ will also increase.

In the quasi-static limit, NPs of sizes of 40 nm and smaller can be considered, since it has been shown that for these sizes retardation effects are negligible (83). The separation between NP is also an essential factor since quantum effects may play an important role. The tunneling current may partially quench the excitation of multipolar modes and limit the possible near-field intensity enhancement. However, quantum effects are significant for distances below 0.5 nm. (84) Therefore, the geometric parameter can take values as small as $\sigma = 1.0125$ for the largest nanoparticles and shortest distances. One of the advantages of this formalism is that it makes explicit that the coupling mechanism of the particles through the excitation of multipoles solely depend on σ. Therefore, it is sufficient to rescale the nanosphere's diameters and distances by a factor to keep σ, retaining all the results and the physics of the multipolar coupling. Here, we discuss the results for nanospheres with a radius of 12.5 nm and interparticle distances of 0.5 nm and larger., i.e., $\sigma \geq 1.02$. For these values, we see that the influence of the multipolar coupling is still considerable, quantum effects are negligible, and that the quasi-static approximation still holds.

The number of multipolar moments, i.e., l_{max}, needed to ensure convergence in the solutions depends on the configuration of the system, or equivalently on the value of σ, with a more significant value of l_{max} needed for a smaller geometric factor, σ. We found that to ensure convergence within the 1% of the solutions for the configurations considered in this work, a cut-off equal to $l_{max} = 150$ is needed. In principle, the formalism outlined in the previous section can be used for any material once the dielectric function is known. In this work, we present results for silver nanospheres,(85) since these have shown to produce more considerable field enhancement than gold, for example, (86).

In the following section, we discuss the principal result of the model, i.e., the introduction of a proper multipole excitation field in Eqs. (4.14). Combining geometry and symmetry of illumination, it is possible to modify the spectrum further, the number of excited modes, and the near field of a nanostructure.

5.1 Excitation of Multipolar Modes as a Function of the External Field

We consider two different types of external fields, first the case of a spatially homogeneous external field with a parallel polarization to the axis that joins the centers of the spheres. This is achieved by taking $F^{\mu'} \neq 0$ in Eq. 4.14 with $\mu' = (l' = 1, m' = 0, i)$. As a second case, we consider a spatially inhomogeneous external field such that if felt by an isolated sphere induce a quadrupole charge distribution. This is achieved by taking $F^{\mu'} \neq 0$ with $\mu' = (l' = 2, m' = 0, i)$, and is shown in Fig. 5.1

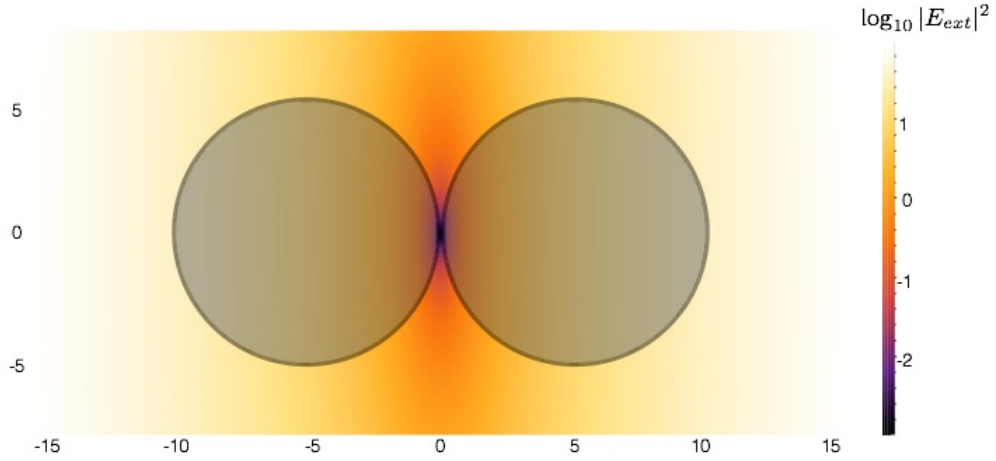

Figure 5.1: Quadrupolar external field in the presence of spherical a = 12.5 nm NPs with a 1 nm gap .

In Fig. 5.2 we plot the coupling strengths $C^1_{1,s}$ with $s = 1, ..., 5$, as a function of σ for the homogeneous external field $F^{1,0,i}$. Each curve represents the coupling strength of the dipole moment to the external field $F^{1,0,i}$, through each corresponding $s-$mode. For a given geometric factor, σ, the coupling strength to each available mode varies, subject to the constraints imposed by sum rule,(34) $\sum_s C^1_{1,s} = 1$. This can be thought of as a a distribution of the coupling strengths among all the available modes of the dimer. For this case, at large σ, the excitation efficiency coefficients of the mode with $s = 1$ dominates, i.e. $C^1_{1,1} \to 1$, while coupling strengths associated to $s = 2, 3, \ldots$ vanish, $C^1_{1,s} \to 0$. At large interparticle distances, the optical response of the dimer is dominated by the dipole mode of the isolated nanospheres, as expected. Thus, the mode $s = 1$ is identified with the dipole response of the dimer. As σ decreases, coupling strengths to higher order multipole modes become more important. By accurately selecting σ, we modify the eigenvalues of the system and the coupling strengths and therefore, the resonant frequencies and optical response of the dimer. Thus, it is possible to tune the spectrum of the dimer, i.e., enhance, suppress or shift the resonant peaks by considering only the geometric parameter σ. Fig. 5.2

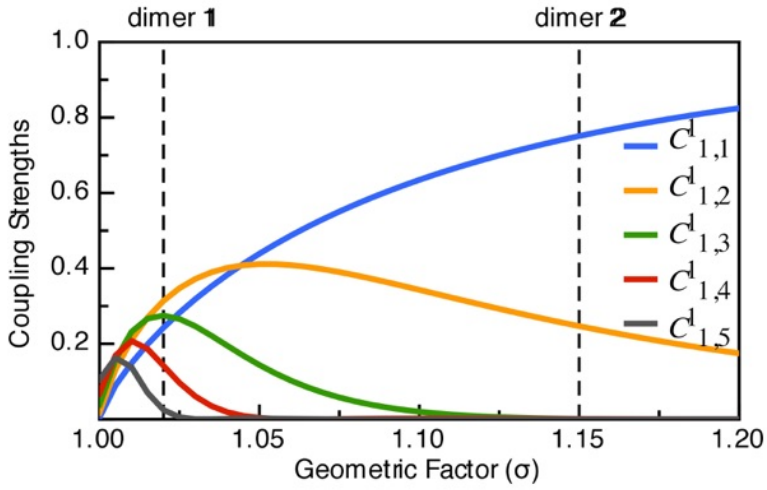

Figure 5.2: Coupling strengths $C^1_{1,s}$ for $s = 1, ..., 5$.

From Fig. 5.2, is can be seen that for geometric factors smaller than approximately $\sigma \approx 1.05$ the coupling strength of the dipolar mode becomes lower than that of the quadrupolar mode. Therefore condition $\sigma < 1.05$, defines the regime where higher order multipolar modes arise and eventually dominate. With this in mind, we concentrate our study on two cases that fall into the different coupling regions. We label with **1** the dimer with $\sigma = 1.02$ which falls within the region with strong multipolar coupling and with **2** the dimer with $\sigma = 1.15$ that falls in the region where the dipolar response is expected to dominate. In

	σ	s	λ_s (nm)	Im$[u(\lambda_s)]$	$C^1_{1,s}$	$C^2_{1,s}$	n_s
Dimer 1	1.02	1	444	0.015	0.242	0.212	0.130
		2	375	0.037	0.314	0.124	0.241
		3	355	0.067	0.275	-0.067	0.313
		4	348	0.097	0.141	-0.179	0.361
		5	344	0.113	0.024	-0.094	0.392
Dimer 2	1.15	1	370	0.043	0.751	0.346	0.251
		2	350	0.087	0.247	-0.328	0.361
		3	342	0.117	0.001	-0.020	0.408

Table 5.1: Resonant wavelengths (λ_s), imaginary part of the spectral function (Im$[u(\lambda_s)]$) evaluated at the resonant wavelength and strongest coupling strengths ($C^{l'}_{1,s}$ with $l' = 1$ and 2) to the modes of the two dimer configurations considered.

Fig. 5.2 these specific geometric parameters are indicated with vertical dashed lines. Once the geometric parameters are fixed, we can calculate the eigenvalues and coupling strengths for both dimers.

The most significative values of n_s and $\mathrm{C}^{l'}_{1,s}$ for the two dimers are listed in Table 5.1. For dimer **1** ($\sigma = 1.02$) the nanospheres are very close, resulting in the strongest coupling for mode $s = 2$, with $C^1_{1,2} = 0.314$, followed by $s = 3$ with $C^1_{1,3} = 0.275$ and then by $s = 1$ with $C^1_{1,1} = 0.242$. Modes with $s = 4$ and $s = 5$ have significant coupling, the first five modes account for the 99.6% of the total coupling with the homogeneous external field. For dimer **2** ($\sigma = 1.15$) illuminated by an external field with $l' = 1$, we found $C^1_{1,1} = 0.751$ when $s = 1$ and $C^1_{1,2} = 0.247$ when $s = 2$. Both modes account for the 99.8% of the total coupling strength to the external field, thus modes with $s > 2$ become irrelevant at this particular σ. Here, the $s = 1$ mode, corresponding to the dipole mode of the dimer at large interparticle distances, dominates.

Once eigenvalues and coupling strengths are calculated, we fix the dielectric function of the material to calculate first the spectral variable $u(\omega)$, and then, the resonant frequencies or wavelengths ($\lambda_s = c/\omega_s$) from the condition, Re$[u(\omega_s)] = n_s$, imposed in Eq. (4.22). The obtained values for both dimers are listed in Table 5.1, as well as the corresponding values of Im$[u(\omega_s)]$. It is worth pointing out that the eigenvalues, and therefore the calculated resonant frequencies, are independent of the external field, being equal for both types of external fields considered. In Fig. 5.3, we plot the scattering cross section spectrum

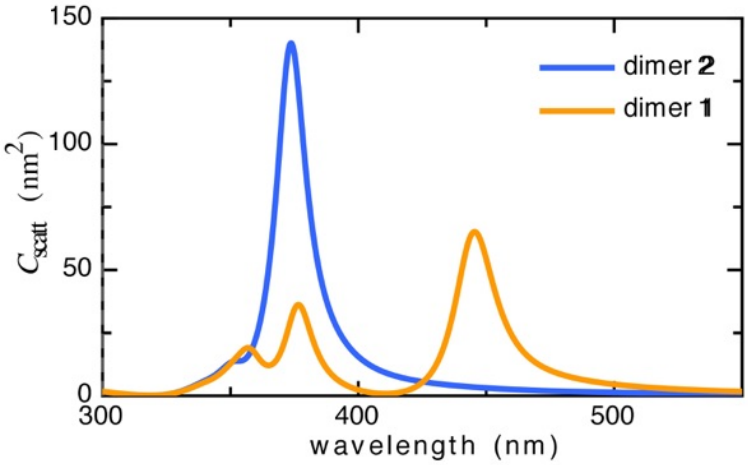

Figure 5.3: Scattering cross sections for dimers **1** and **2** made by silver nanospheres with $a = 12.5$ nm.

calculated with Eq. (4.22) for dimers **1** and **2**. The peaks and resonant frequencies in the scattering cross section can be understood in terms of the coupling strengths $C^1_{1,s}$ and eigenvalues n_s. For dimer **2** ($\sigma = 1.15$), the intense peak around $\lambda_1 = 370$ nm is associated to the dipole mode of the dimer ($s = 1$). For this configuration, higher order multipole modes are not appreciated because the corresponding coupling strengths are small and located in a range with large values of $\mathrm{Im}[u(\omega_s)]$, compared with $s = 1$. In general, as $\mathrm{Im}[u(\omega_s)]$ is larger, the energy dissipation increases and the intensity of the resonances diminishes, in agreement with Eq. (4.6). Consequently, even though $C^1_{1,2} \simeq (1/3)C^1_{1,1}$, only a small shoulder associated with the quadrupole mode is observed around $\lambda = 350$ nm.

For dimer **1** ($\sigma = 1.02$), in Fig. 5.3 we observe 3 distinct peaks and a redshift of all the resonances. The redshift can be understood in the following manner: because the external field is parallel to the axis that joins the nanospheres, the field polarizes the particles, such that, the induced local-field is in the same direction as the applied field. Both induced and applied fields are contrary to the restoring force acting on the electron cloud, therefore reducing the resonant frequency causing the redshift. (47). An analogous argument can be used for the redshift of the multipole resonances. As expected, higher order modes beyond the dipole mode have smaller resonant wavelengths, as they require larger energies to be excited. Comparing the peaks of dimer 1 and 2, it can be seen that the intensity of the dipole peak reduces in dimer 1 compared to dimer 2. This is because in dimer 2, the dipole mode has a larger coupling strength than in dimer 1 as shown in table (5.1). Since the coupling strengths of the quadrupolar (s=2) and octupolar (s=3) modes increase in dimer 1, and since the sum rule $\sum_s C^1_{1,s} = 1$ must be satisfied, the coupling strength to the dipolar

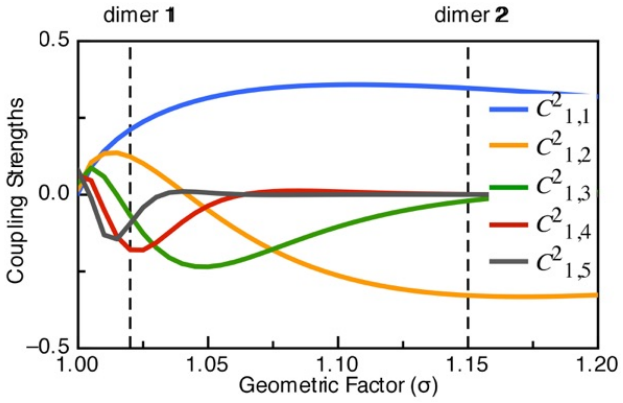

Figure 5.4: Coupling strengths efficiency coefficients $C^2_{1,s}$ for $s = 1, ..., 5$ plotted against he dimensionless geometric factor σ.

mode decreases. However, as seen in Eq. (4.6) peaks in the spectrum are proportional to $C^1_{1,2}/\mathrm{Im}[u]$. Therefore, it is not always true that a larger coupling coefficient leads to a stronger peak. For example, in spectrum of dimer 1, even though the coupling strength to the dipolar mode (s=1) is smaller than that to the quadrupolar (s=2) and ocutupolar (s= 3) mode, $C^1_{1,1} < C^1_{1,2}$ and $C^1_{1,1} < C^1_{1,3}$, the dipole peak is still more intense because the corresponding $\mathrm{Im}[u(\omega_s)]$ value is smaller at the resonant frequency, as shown in table (5.1).

Next, we consider the case of the spatially non homogeneous exciting field, $F^{\mu'} \neq 0$ with $\mu' = (l = 2, m = 0)$. In Fig. 5.4 the coupling strengths to the second type of external field with $l' = 2$ are shown. Interestingly, we observe that the coupling strengths $C^2_{1,s}$ for all modes s qualitatively differs from those for an external field with $l' = 1$. For instance, all the curves exhibit a maximum and/or a minimum value at a particular σ and eventually all excitation efficiency coefficients go to zero for large σ. This is consequence of the sum rule $\sum_s C^2_{1,s} = 0$. (34) Recall that the $C^1_{2,s}$ describe the coupling strengths of the external field, $F^{\mu'} \neq 0$ with $\mu' = (l = 2, m = 0)$, with the dipole moments induced on the particles. The sum rule ensures that at large separation distances the only induced multipolar moment is of the same order as the exciting field, which in this case is the quadrupolar mode, and that the total induced dipole moment is zero. Fig. 5.4 displays $C^2_{1,s}$ with $s = 1, ..., 5$, as a function of σ for an external field with $l' = 2$ and $m = 0$. Distinctly, negative values are allowed for some modes, which can be interpreted as an excitation of a given moment opposing the external field. In Table 5.1 also $C^2_{1,s}$ with $s = 1, ..., 5$ are listed. As previously mention, the eigenvalues do not depend on the type of exciting field, the resonant frequency remain the same, independently of the exciting field.

The scattering cross section for dimer **1** ($\sigma = 1.02$) and dimer **2** ($\sigma = 1.15$) is shown

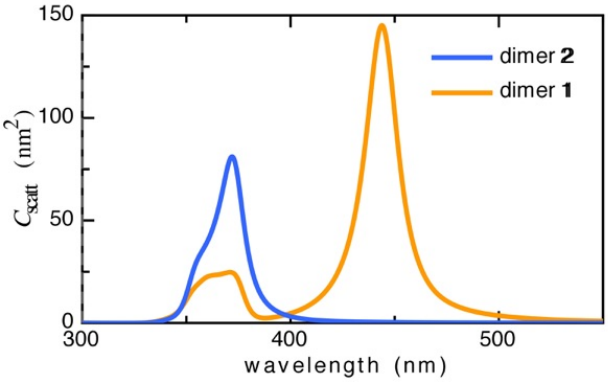

Figure 5.5: Scattering cross sections for dimers **1** and **2** made by silver nanospheres with $a = 12.5$ nm.

in Fig.5.5. For the case of dimer **1** ($\sigma = 1.02$), the smaller peak found at $\lambda = 370$nm, represents an overlap of many high order modes which are spectrally too close to be resolved. Differences in intensity obtained with a $l' = 1$ and $l' = 2$ external field can be explained by comparing coupling efficiencies. For example, consider dimer **1** ($\sigma = 1.02$), with a plane wave external field ($l' = 1$), as shown in Fig. 5.3. For this configuration, coupling strengths to the quadrupole and octupole modes are larger than in the dipolar mode. Therefore, although there is more dissipation at the quadrupole and octupole resonances, the three peaks are still clearly distinguished. For dimer **2**, the coupling strengths to the quadrupole field, $C^2_{1,1}$ and $C^2_{1,2}$ are comparable but of opposite sign. These give rise to an uneven peak structure in the scattering cross section spectrum, shown in Fig. 5.5. Notice that this peak is half as intense when compared with the one shown in Fig. 5.3, for an homogeneous external field. This feature arises from the differences in the coupling strength to the different external fields, so that there is much larger coupling to dipole mode in the case of an homogeneous field. As in the cases of plane wave illumination ($l' = 1$), higher multipole modes ($s > 1$) are not appreciable in the spectrum as a consequence of the small values of the corresponding coupling strengths for those modes and large $\mathrm{Im}[u(\omega)]$.

Summarizing, it has been shown that for a given geometric factor and dielectric function, the resonant wavelengths and therefore the value of $\mathrm{Im}[u(\omega)]$ are fixed, and independent of the external field. On the other hand, peak intensities are inversely proportional to $\mathrm{Im}[u(\omega)]$ and directly comparable to the coupling strengths of the mode, whose coupling strength depends on the symmetry of the external field being used.

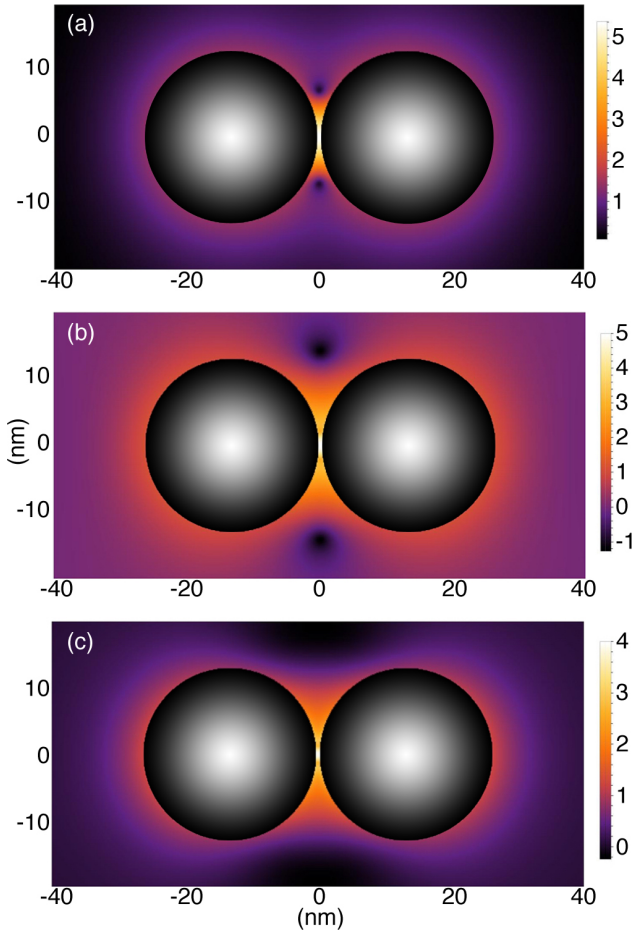

Figure 5.6: Normalized near field intensity, $\log_{10} \frac{|E|^2}{|E_0|^2}$, for dimer 1 illuminated by an external field $l' = 1$, at the (a) dipole (s=1), (b) quadrupole (s=2) and (c) octupole (s=3) resonances at $\lambda_1 = 444$, $\lambda_2 = 375$ and $\lambda_3 = 355$ nm, respectively.

5.2 Multipolar contribution to the near field

Once the multipolar moments are obtained, it is possible to calculate the electric near-field intensity outside the nanospheres and separately analyze the contribution of each multipolar moment by using Eq. (4.19). Notice that all the multipolar moments contribute to the induced field, as explicitly shown in Eq. (4.19). This means that when a given mode of the dimer s is excited, the spatial distribution of the charge density and electric field are not only determined by the $s-$ multipolar moment but also by all the other excited moments that can couple to it.

First we analyze the case of an homogeneous external field. Fig. 5.6 displays the spatial distribution of the near field intensity normalized by the intensity of the incident field for the dipole, quadrupole and octupole modes of dimer **1** ($\sigma = 1.02$) with an external field

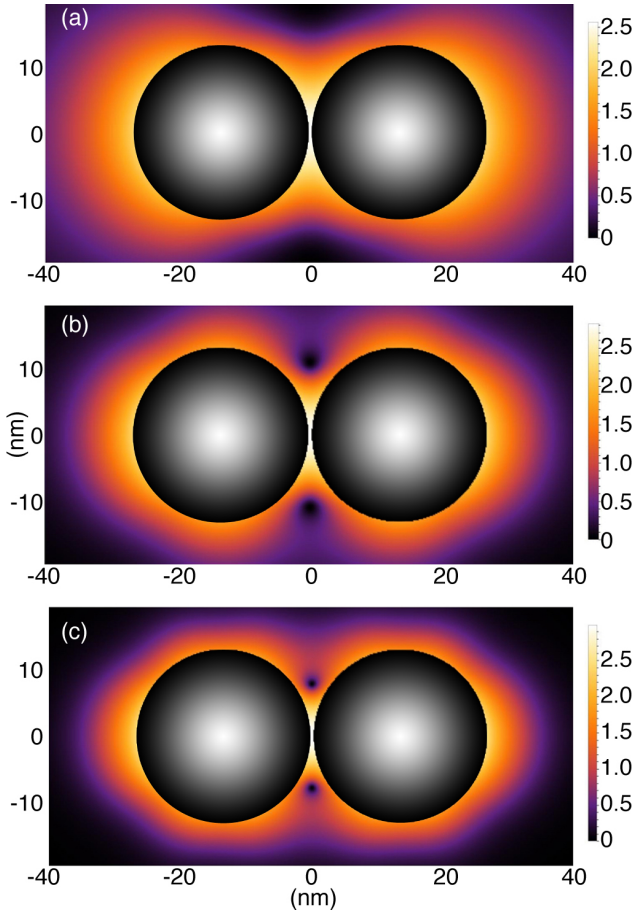

Figure 5.7: Dipole $l = 1$ (a), quadrupole $l = 2$ (b) and octupole $l = 3$ (c) contributions to the electric near field intensity, $\log_{10} \frac{|E|^2}{|E_0|^2}$, for a quadrupole mode $s = 1$ at $\lambda_1 = 444$ nm and an external field $l' = 1$.

with $l' = 1$. This configuration is equivalent to taking nanosphere's radius of 12.5 nm and a separation distance of 0.5 nm. All modes exhibit the maximum of field intensity in the gap of the dimer, which can be enhanced more than four orders of magnitude for modes $s = 1$ and $s = 2$. For both types of external fields, we observe that for all modes, the most significant contribution to the field enhancement and its overall shape are given by the dipole moment, which in the induced field which can be seen to have a symmetry similar to that of interacting dipoles.

Fig. 5.7 displays the multipolar decomposition of the electric near field intensity of mode $s = 1$ of dimer **1** at $\lambda_1 = 444$ nm into the first and most significant components with $l = 1$, $l = 2$ and $l = 3$. That is, in Fig. 5.7 we show the multipolar decomposition of the field of mode $s = 1$, shown in Fig. 5.6. The near field plots are obtained by selecting the corresponding l in Eq. (4.16) for a given wavelength and then, calculating the field of each component using Eq. (4.19). We found that as l increases the intensity of the field associated with each

component decreases. This fact follows from the coupling of the external field to high order moments, which is achieved indirectly via Eq. (4.16), so the field intensity enhancement associated with them is weak. In Fig. 5.7 we can also observe the spatial distribution of the near field for each l, which shows a symmetry related to the corresponding component. Higher multipole moments are characterized by pronounced spatial modulations and strong confinements of the electric field intensity around the nanospheres. For example, for $l = 1$ the two darker spots or nodes are along the azimuth, while for $l = 2$ there are three dark spots for each nanosphere, and for $l = 3$ we found four dark spots for each nanosphere. The decomposition of the near-field allows us to follow the contributions to the total field. The total enhancement is shown in Fig. 5.6 is obtained by adding these fields as well as contributions from the rest of the components up to l_{max}.

Now, we want to analyze the dimer near field when the spatially structured external field is applied. Fig. 5.8 displays the spatial distribution of the total electric near-field intensity for the dipole ($s = 1$), quadrupole ($s = 2$) and octupole ($s = 3$) modes of dimer **1** at their corresponding resonant wavelengths: $\lambda_1 = 444$ nm, $\lambda_2 = 375$ nm and $\lambda_3 = 355$ nm respectively. As in the case of plane wave excitation ($l' = 1$), for small values of σ the electromagnetic near-field is strongly inhomogeneous. Also for this type of illumination, the enhancement decreases as the order of the mode increases. The effect of illumination with $l' = 2$ is to increase the overall field enhancement by up to 2 orders of magnitude concerning the $l' = 1$ illumination, as one can observe by comparing Fig. 5.8 and Fig. 5.6 at all resonant wavelengths. The total area where the near field is enhanced displays a pattern in the induced field which is partially due to the spatial inhomogeneity of the incident field. Simultaneously, the intensity enhancement in the regions of the dimer outside the gap decreases more rapidly. Therefore, multipolar illumination might be useful to increase the light-matter interaction in nano-optics experiments or to increase the sensitivity of devices. Notice that even though the intensity of the peaks in the scattering cross-section spectrum in Fig. 5.5 are smaller (less than half the intensity) than in Fig. 5.3, field enhancement for the $l' = 2$ illumination is still more considerable even at the quadrupole and octupole resonances. This result suggests that to perform spectroscopic experiments which require large field enhancement, such as Raman spectroscopy, it is convenient to use the symmetry of the exciting field. Moreover, for experiments, it might prove more useful to tune the emission spectrum to low-intensity high multipole peaks rather than to the more intense dipolar one.

In Fig. 5.9 we show the contributions to the near electric field in the wavelength of the

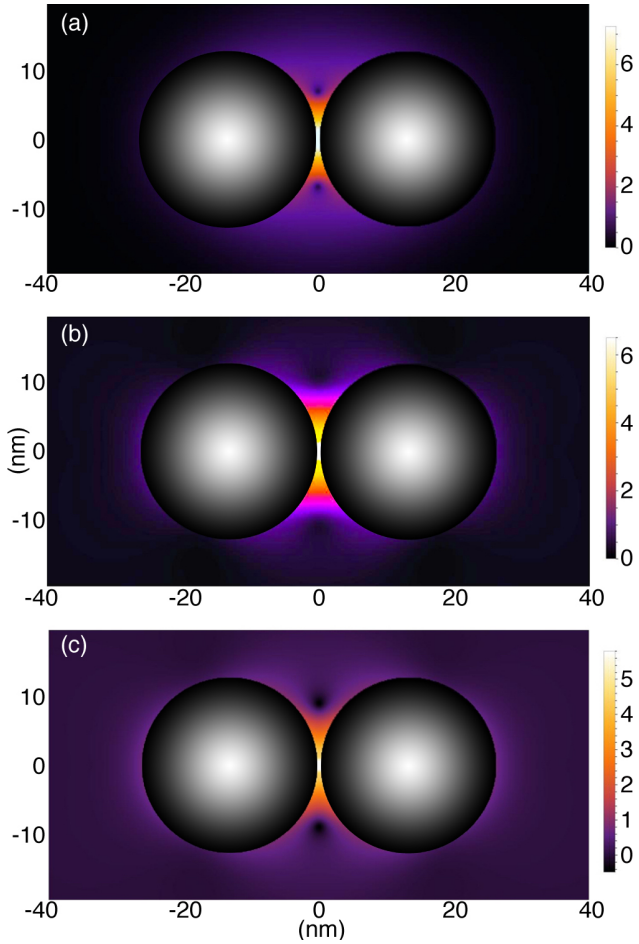

Figure 5.8: Normalized electric near field intensity, $\log_{10} \frac{|E|^2}{|E_0|^2}$, for an external field $l' = 2$, at the (a) dipole (s=1), (b) quadrupole (s=2) and (c) octupole (s=3) resonances at $\lambda_1 = 444$, $\lambda_2 = 375$ and $\lambda_3 = 355$ nm, respectively.

quadrupole resonance at $\lambda_2 = 375$ nm for excitation with $l' = 2$. In other words, we show the decomposition of the field shown in Figure (**??**). In Fig. 5.9 it can be seen that the most significant contribution comes from the quadrupole moment followed by the dipole moment that shows a similar maximum intensity as the octupole. However, the symmetry of the induced field does not always correspond to the order of the mode that is excited. In general, the dominating contribution to the induced field will depend on the chosen external field, the excitation wavelength through eigenmodes and the system's geometry through the excitation efficiency coefficients.

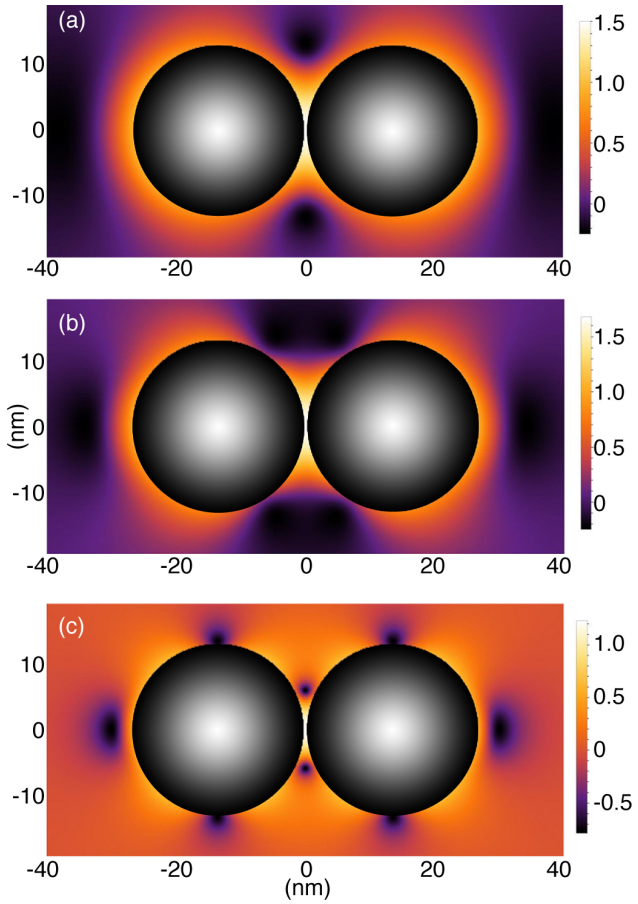

Figure 5.9: Dipole $l = 1$ (a), quadrupole $l = 2$ (b) and octupole $l = 3$ (c) contributions to the normalized near field intensity, $\log_{10} \frac{|E|^2}{|E_0|^2}$, for a quadrupole mode $s = 2$ at $\lambda_2 = 375$ nm and an external field with $l' = 2$.

Chapter 6

Conlusions

A general analytical framework to describe the optical response of nanostructures in the quasi-static limit that treats on the same footing their geometry, dielectric properties, and incident electromagnetic field, being able to isolate the role of each of them precisely was presented. The method is based on the multipole decomposition of both the incident field and the polarizability of the nanostructure. The symmetry of a multipole incident field provides an additional parameter through which it is possible to change the optical response, spatial distribution and near-field enhancement of the illuminated system. Our formalism gives compelling insights into the coupling efficiency of the incident field to the optical modes of the nanostructure, facilitating the analysis of the relative interaction between the mentioned variables. To illustrate the method two limiting geometrical configurations, that of a dimer of metallic nanospheres and two symmetries of the external incident field were used. It was shown that for the configuration with large separation, both types of external fields couple mainly to the dipole mode. However, for a small separation, the spatially modulated field strongly couples to more modes than the homogeneous external field and therefore produces less defined peaks in the scattering spectrum, but larger field enhancements which are covering more area.

Part II

Near-field radiative heat transfer between dielectric nanoparticles

Chapter 7

Introduction

In the previous section a study of the interaction of dielectric particles with multipolar external fields was presented. In this section, we will study the interaction of dielectric particles with thermally emitted EM fields. It will be shown that thermal EM fields are generated by fluctuating charge distributions, and therefore thermal fields will be composed of, not only by spatially homogeneous and quadrupole fields as those considered in the previous section, but by all orders of multipolar fields. Consequently, each mode in the system can be excited by any of the multipolar components of the thermal field. In this way, the tools developed in the previous section will be used and further modified to study thermal radiation. For example the spectral representation, which allows a calculation of the coupling strengths of each particle to the different multipolar external fields, and the charge induce on each particle by the fields will be modified to describe the interaction with thermal fields. To begin, we first present a background of the classical theory of thermal radiation and recent work carried out in the field of near-field energy transfer.

7.1 Motivation

Classical theory of thermal radiation

It is known that a body at a temperature higher than absolute zero emits energy through EM fields. If the object has a higher temperature than its environment, it emits more energy than it absorbs from its surroundings. Conversely, if the object has a lower temperature than its environment, it absorbs more energy than it emits. From this point of view, thermal radiation is a mechanism by which an object reaches thermodynamic equilibrium with its environment. Conceptually, emission of thermal radiation can be understood in the following manner: when a body is at a temperature higher than absolute zero, the atoms

and electrons that make up the body undergo random thermal motion. This accelerates the charge carriers, which emit EM fields that can be described by EM waves over a wide range of frequencies. The EM fields generated through this mechanism transport energy from the body to its environment. It is clarifying to compare thermal radiation with other mechanisms of energy transfer, such as conduction and convection. Conduction is an energy transfer mechanism by which kinetic and potential energy is transmitted among the microscopic constituents of a system. For example, in a solid, it can be carried out by free electrons or by excitations of the system's vibrational modes (phonons). Convection can be observed in gases and liquids, where molecules with high kinetic energy are dragged by currents generated due to temperature gradients and are replaced by molecules with low kinetic energy, giving rise to a net energy transfer (87). Unlike convection and conduction, radiative heat transfer is carried out by EM fields, which do not require a propagation medium or contact between bodies.

Emission of thermal radiation is a phenomenon that has been studied since the nineteenth century. In 1897, Slovenian physicist Jozef Stefan established an empirical law describing the total energy emitted by a surface at temperature T. He based his law on experimental measurements of thermal radiation emitted by platinum wires at different temperatures (88). Stefan proposed that the total energy radiated by a surface, per unit area and per unit time, $u(T)$, is proportional to the body's temperature raised to the fourth power

$$u(T) = \sigma \cdot e \cdot T^4, \tag{7.1}$$

where T is the body's temperature and e its emissivity, a property of the material that takes values between 0 and 1, while $\sigma = 5.6703 \times 10^{-8}\text{W m}^{-2}\text{K}^{-4}$ is Stefan's constant. Employing thermodynamic arguments, Eq.(7.1) was independently derived by Austrian physicist Ludwig Boltzmann in 1884 (88), for which it is known as the Stefan-Boltzmann law. Furthermore, German physicist Gustav Kirchoff discovered a useful relationship between a bodies emission e and absorption efficiency a. Kirchoff determined that in thermodynamic equilibrium, the emissivity of a body equals its absorptivity $e = a$ (87, 89). A body that absorbs all radiant energy that it is exposed to, has emissivity and absorptivity equal to one $e = a = 1$, so that it receives the name of black body. At the end of the 19th century, the radiation spectrum of a black body was a subject of intense research, with several attempts to formulate a theory that correctly described the phenomenon. It was not until 1900 that Max Planck obtained the spectral distribution density, $\rho(\nu, T)$, of the thermal radiation of black body (89)

$$\rho(\nu, T) = \frac{8\pi h\nu^3}{c^3} \frac{1}{e^{\frac{h\nu}{k_B T}} - 1}, \tag{7.2}$$

where ν is the frequency, h the Planck constant, c the speed of light and k_B the Boltzmann constant.

To obtain Eq.(7.2) Planck modeled the black body as a box with isothermal walls of length L, with a small hole, so that any light entering the box remains trapped inside. He modeled the oscillating electrons in the walls of the blackbody as harmonic oscillators, vibrating at frequency ν that could only have discrete energies ϵ which satisfy

$$\epsilon = nh\nu, \tag{7.3}$$

where n is a natural positive number. A statistical average of the energy of oscillators inside the box was calculated assuming the Boltzmann probability distribution

$$\langle \epsilon(\nu, T) \rangle = \frac{\sum_{n=0}^{\infty} h\nu e^{-\epsilon/kT}}{\sum_{n=0}^{\infty} e^{-\epsilon/kT}} = \frac{h\nu}{e^{\frac{h\nu}{k_B T}} - 1}, \tag{7.4}$$

where $\langle .. \rangle$ indicates a statistical average over all possible energy values that satisfy Eq.(7.3). To carry out the sum in Eq.(7.4), it is necessary to count the number of modes at each frequency ν that exists within the box, that is, the number of modes that satisfy the boundary conditions. Thus, a spectral density of modes is obtained

$$N(\nu)d\nu = \frac{8\pi a^3 \nu^2}{c^3} d\nu. \tag{7.5}$$

The spectral energy density per unit volume at a frequency ν is obtained in terms of the density of modes Eq.(7.5), and the average energy of a harmonic oscillator of frequency ν Eq.(7.4)

$$\rho(\nu, T)d\nu = \frac{\langle \epsilon \rangle N(\nu)}{L^3} = \frac{8\pi h\nu^3}{c^3} \frac{d\nu}{e^{\frac{h\nu}{k_B T}} - 1}. \tag{7.6}$$

Figure 7.1 shows the energy spectra radiated by a black body at different temperatures. It can be seen that radiated energy is an incoherent phenomenon, in the sense that fields are radiated over a wide spectral band. At a given temperature, the wavelength at which maximum energy is radiated can be described by Wien's law (89)

$$\lambda_w = \frac{c\hbar}{k_B T}, \tag{7.7}$$

where $\hbar = h/2\pi$. Clearly, at higher temperatures, Wien's wavelength decreases. For example, at $1K$ Wien's wavelength is $2229.8\mu m$ as can be seen in Table 7.1. At a temperature

$T(K)$	$\lambda_w(\mu m)$
1	2298.8
100	22.9
273	8.4
1000	2.3
6000	0.38

Table 7.1: Wien wavelength as a function of temperature λ_W.

of $6,000K$ (approximate temperature of the surface of the sun) the Wien wavelength is approximately 0.38 μm = 380 nm, within the range of visible light To obtain the Stefan-Boltzmann law from planks spectral density, assume that a small hole is cut into the black body box. All radiation emanating from this hole will be moving at the speed of light c. Also, the radiation will be uniformly distributed throughout the hemisphere of solid angles, and one half of the energy will be oriented such that it can move outward through the hole. The spectral radiation intensity is defined as the rate of energy emitted per unit area per unit solid angle and per unit wavelength. The rate of energy emitted per area, $B(\nu)$ is simply the product of the energy density derived above multiplied by $c/4\pi$:

$$B(\nu, T)d\nu = \frac{2h\nu^3}{c^2}\frac{d\nu}{e^{\frac{h\nu}{k_B T}} - 1}. \tag{7.8}$$

The total power emitted per unit area at the surface of a black body may be found by integrating the black body spectral flux found over all frequencies, and over the solid angles corresponding to a hemisphere above the surface

$$u(T) = \int_0^\infty \int_{hemisphere} d\Omega B(\nu, T) = \sigma T^4 \tag{7.9}$$

Once the radiation spectrum of a blackbody has been correctly described, it is possible to calculate radiative energy transfer between two black bodies. Furthermore, since a blackbody is an ideal emitter and absorber, with $e = a = 1$, energy transfer between blackbodies establishes a maximum limit to the amount of energy that can be exchanged via thermal radiation between any two bodies. Assuming that blackbody radiation is spatially isotropic, it is possible to derive the Stefan-Boltzmann law from Planck's spectral distribution by integrating over the frequency spectrum. It is then possible to calculate radiative energy transferred between two blackbody surfaces at temperatures T_1 and T_2, with $T_1 > T_2$. Considering that energy radiated from one blackbody surface is perfectly

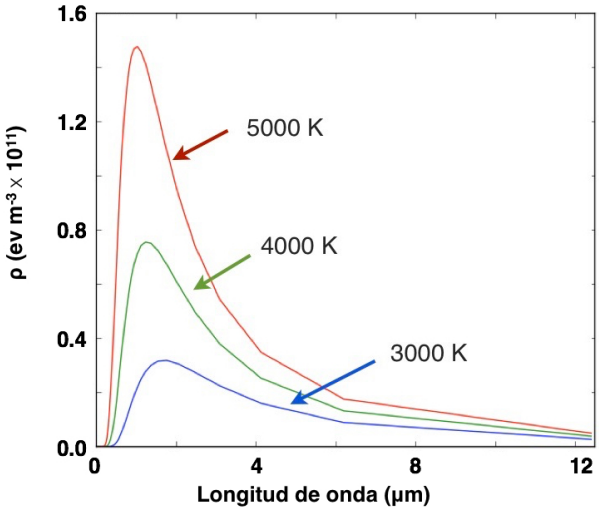

Figure 7.1: Plank's spectral density of black body radiation at different temperature.

absorbed by the other, energy transfer is given by

$$q = \sigma(T_1^4 - T_2^4) = \frac{\pi^2 k_B}{60\hbar^3 c^2}(T_1^4 - T_2^4), \tag{7.10}$$

where the Stefan constant has been written in terms of universal physical constants $\sigma = \frac{\pi^2 k_B}{60\hbar^3 c^2}$, which are obtained from Planck's law. From Eq.(7.10) it can be seen that radiative energy transfer only depends on the bodies' temperatures and not on the separation distance between the surfaces. This is a direct consequence of equations (7.2) - (7.7), which do not depend on separation distances. However, given that the Wien wavelength defines a characteristic distance of a system (see Table 7.1), the following question arises: Is there a modification to the radiation spectral density at distances comparable to the Wien wavelength? The differences in thermal radiation emitted at distances comparable to the Wein wavelength are discussed in the following section. Afterward, a review is given on some experimental measurements of radiative energy transfer between bodies separated by distances smaller than the Wien wavelength.

Near-field vs. far-field thermal radiation

Planck's theory describing the thermal emission of a black body is grounded on a critical assumption, which is given in the first chapter of his book "Theory of Thermal Radiation" (Theorie der Wärmestrahlung) (90):

"Throughout the following discussion, it will be assumed that the linear dimensions of all parts of the system, [...], are large compared to the wavelength of the considered rays ."

As a consequence, Planck's theory is valid when typical dimensions of the system under consideration, including size and separation distances, are large compared to the wavelength of emitted fields. Therefore, the term *far-field regime*, in the context of thermal radiation, is used for cases in which Planck's theory is applicable. In this regime, geometric optics is valid. This can be attributed to the fact that the coherence length is of the same order of magnitude as the Wien wavelength, and energy transport by EM fields is incoherent at these distance. Consequently, interference effects between waves are neglected (21), and energy transfer due to two incident rays is merely the sum of the energies of each ray, regardless of their respective phases.

As distances of the system decrease to sizes comparable with λ_w, Planck's theory is no longer expected to be valid, and phenomena not considered in Planck's theory, must be taken into account. These cases fall into what is known as the *near-field regime*. To continue the discussion of the characteristics of thermal radiation and energy transfer at separation distances from the emitting body comparable to the Wien wavelength, it will useful to keep in mind these two limiting regimes. The transition from the far-field to the near-field regime is determined by comparing dimensions of the system with a given paramete., Traditionally, this critical length scale is determined from the Wien law, and corresponds to the wavelength of the peak emission according to the Planck blackbody distribution (91). At room temperature, thermal wavelengths are of the order of micrometers, consequently, when distances of this order of magnitude separate bodies, near-field effects arise and eventually can dominate. Therefore, at small distances, it is necessary to rethink the problem of thermal radiation and to resort to Maxwell's equation to obtain an accurate description.

Measurments of near-field heat transfer

One of the principal difficulties in experimental setups is maintaining a fixed separation distance between bodies. In past years three main experimental configurations have been used to measure radiative heat transfer in the near-field: plate-plate (92), tip-plate (93), and sphere-plate configurations (94), these are shown in Fig. 7.2. Near-field heat transfer between parallel media is the most well-studied geometry since analytical expressions for the heat flux can be derived from first principles (95). However, the parallel plate configuration is the most experimentally challenging of the different geometries due to the difficulty in keeping surfaces parallel at submicrometer vacuum gaps, as well as surface roughness effects at such length scales. Tip-plate and sphere-plate configurations are easier to set up,

however, the smaller volume of the emitter and receiver, significantly reduces the near-field heat flux and makes it difficult to distinguish true heat transfer signals from surrounding noise.

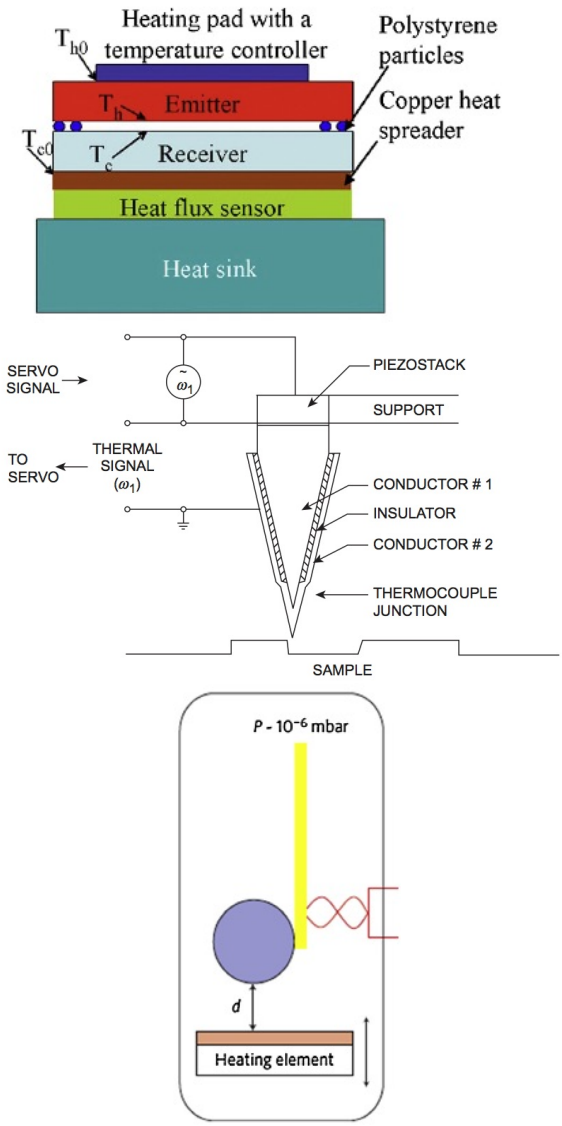

Figure 7.2: Schematic of the three main experimental setups (from top to bottom): plate-plate, tip-plate, and sphere-plate.

The first measurements of near-field radiative heat transfer were reported by Hargreaves in 1969, between two flat parallel chromium plates at room temperature separated by distances of about 1μm (96). These separation distances fall within the near-field regime, as can be seen from Table (7.1), so that Plank's radiation law is not expected to hold. The emitter and receiver temperatures were 323 and 306 K, respectively. The parallelism of the plates was evaluated using both optical interferometry and by measuring the electrical

capacitance of three individual capacitors created by three pairs of metallic plates integrated into the emitter and receiver. Changes in parallelism of the plates resulted in a change in the capacitance. With the emitter heated resistively, the radiative heat flow to the receiver was calculated as the additional heat input required for maintaining the temperature of the emitter at a constant value as the gap size was varied. Hargreaves found a strong distance dependence of radiative heat transfer, with a noticeable increase starting at a gap of $\approx 2.5mm$, contrary to what is predicted by the Stefan-Boltzmann law.

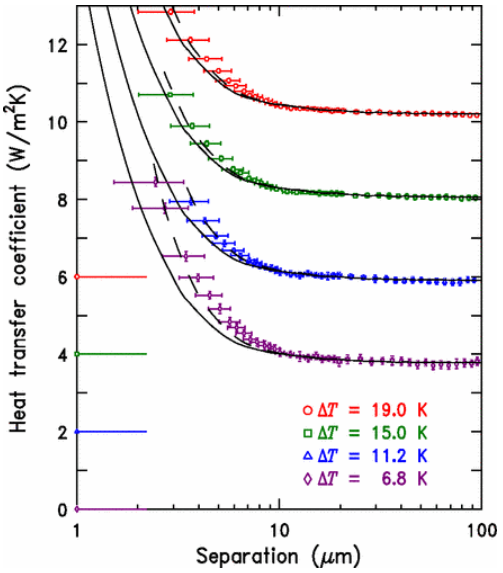

Figure 7.3: Energy per unit area, time and degree Kelvin transmitted (transfer coefficient) between sapphire plates separated by vacuum for different temperature gradients as measured by Ottens (97). The solid lines represent theoretical predictions and the curves are each offset vertically, their zeros are indicated by the horizontal lines extending from the left axis.

Later on, Ottens et al. found more conclusive evidence using parallel sapphire plates in a vacuum chamber at $303.2°K$ (97). Ottens measured the energy transfer per unit area and temperature unit, known as transfer coefficient, for separation distances between $2\mu m - 100\mu m$ at different plate temperatures, shown in Figure 7.3. The emitter had a heater wound on a copper ring attached to the back of the plate. The heater current and voltage can be used to calculate the power required to keep the plates at a given temperature difference and therefore measure radiative heat transfer. At distances greater than 10μm, the transfer coefficient tends to the constant value predicted by the Stefan-Boltzmann law. The authors point out that at lower distances energy transfer increases, exceeding that predicted between black bodies. The transition from far-field to a near-field regime is evident when the heat transfer coefficient starts increasing with decreasing gap.

An increase in energy transfer of over an order of magnitude can be seen for the considered separation distances.

Measurements of heat transfer at nanometric separation distances were finally obtained by Müller-Hirsch et al. (1999) (98) and Kittel et al. (99). These experiments used the tip-surface configuration to measure Near-field thermal radiation. This type of setups owe their origin to techniques such as atomic force microscopy. The authors fabricated a scanning probe with an integrated thermocouple tip similar. Müller-Hirsch used a 100-nm thick gold film deposited on mica. In this case, the probe was at 300 K while the sample was set to 100 K and a change in thermovoltage measured the change in heat flow. Kittel measured the transmitted power (Joule/sec) between a scanning tunneling microscope Au tip, and Au and GaN surfaces in ultra-high vacuum condition shown in Figure 7.4 . Authors observed a strong decrease in heat transfer with increasing separation distance. By modeling the tip of the microscope as a small sphere in a dipolar approximation and the sample as a semi-infinite surface, they theoretically calculated the transfer of electromagnetic energy between the half-space and the sphere. A dependence on the transfer of energy with the separation between the tip of $1/d^3$ was found, characteristic of the interaction between an electric dipole and an infinite plane in the non-radiating limit (100). This dependence was checked in the experiments as shown in Figure 7.4. It can be seen that for distances less than 10 nm there was a discrepancy with their theoretical predictions. The authors propose that one of the causes of the discrepancy is that at such small separation distances multipoles of a higher order than the dipole are excited. (101) .

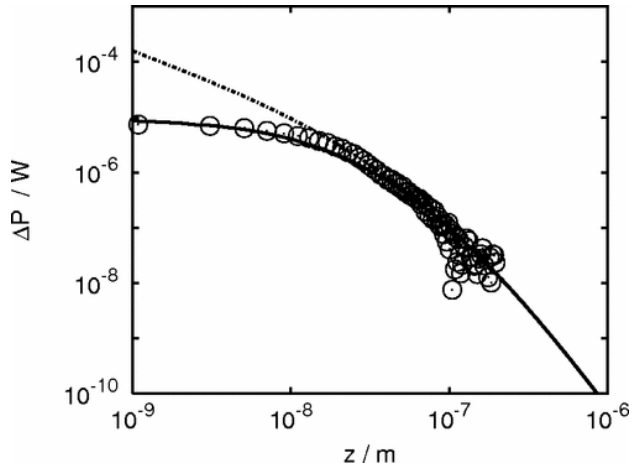

Figure 7.4: Heat power (J / sec) measured between a tip of a microscope (circles) and a gold surface. The dotted line corresponds to the theoretical predictions and the black line to an adjustment made by the authors (99).

The sphere-plate configuration is a compromise between the plate-plate and tip-plate system in the sense that, the large surface of the sphere allows greater heat transfer and therefore is easier to measure, but the sphere cannot be brought as close to the surface as the tip-plate configuration. Shen et al. (102) used this setup to measure near-field heat flux between the silica sphere and flat substrates as shown in Fig. 7.5. Three different substrates were used, namely, Au, Si, and SiO. Under the proximity force theorem (103), which assumes the sphere to be locally flat, heat transfer coefficient can be approximated as $\approx B/d^2$ with B being a constant and d the separation distances and are compared with the experimental results. The resultant near-field heat transfer coefficient between glass sphere and substrate was measured to be three orders of magnitude more than that expected between black-bodies for the smallest separation distance of 30 nm. The authors were therefore able to experimentally demonstrate that the near-field heat transfer can exceed blackbody radiation.

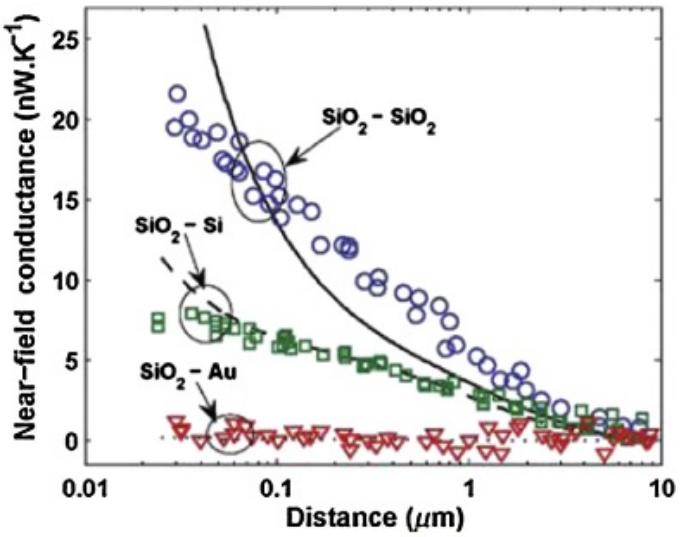

Figure 7.5: Plot of experimental near-field conductance, nW per Kelvin, measured at different vacuum gaps. For comparison, the measured values are compared with theoretical results from proximity force theorem shown by black lines (102).

Summarizing, these results show that at distances of separation smaller than the wavelength of Wien, the radiative heat transfer becomes dependent on distance, unlike that predicted by the Stefan-Boltzmann law (7.10). This can be traced back to the fact that Planks law (7.6) only takes into account the propagating EM fields radiated by the walls of the black body. Consequently, the radiated power described by these equations is independent of the separation distance to the surface. This suggests that other electromagnetic

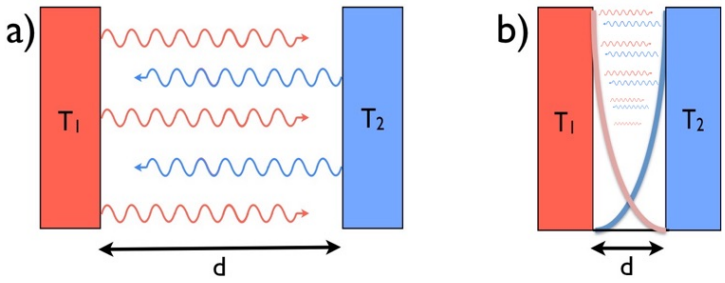

Figure 7.6: There are two modes of radiative heat transfer between two surfaces at temperatures T_1 and T_2. a) Evanescent modes are negligible while propagating modes dominate for separation distances $d > c\hbar/k_BT$ b) Evanescent modes dominate energy transfer for separation distances $d < c\hbar/k_BT$.

(non-propagating) modes can contribute to heat transfer at distances less than the Wien wavelength. Motivated by this, the following section presents an overview of the theoretical models that have been used to describe radiative heat transfer in the near field.

7.2 Background

Theoretical Models: Planar Geometries

The experimental work mentioned in section 7.1 shows that at small separation distances ($d < \lambda_w$) heat transfer is much higher than that predicted by the Stefan-Boltzmann equation. Keeping in mind that Plank's theory of radiation, from which the Stefan-Boltzmann equation follows, only takes into account propagating fields, it is expected that discrepancy between the Stefan-Boltzmann theory and experimental measurements arise from not including surface modes in the calculation of energy transfer (104). A distinction was made between the near-field region ($d < \lambda_w$), where evanescent fields contribute to the electromagnetic energy density and the far-field ($d \gg \lambda_w$) where evanescent fields have almost completely decayed and only propagating fields exist. In the far-field, power radiated by a surface at temperature T is correctly described by the Stefan-Boltzmann law (Eq.7.1), which only takes into account propagating fields. It should be mentioned that since the black body has a maximum emissivity $e = 1$, the Stefan-Boltzmann radiation law places an upper limit on the energy that can be transferred using propagating electromagnetic fields. However, in the near-field ($d \approx \lambda_w$) evanescent modes contribute actively to the density of electromagnetic energy which allows the limit imposed by the law of Stefan-Boltzmann to

be exceeded (21).

As an illustrative case, consider the transfer of radiative energy between two blackbody surfaces at temperatures T_1 and T_2 with $T_1 > T_2$, as shown in Fig.7.6. Consider two cases, in which they are separated by a distance d greater than $d \gg c\hbar/k_B T = \lambda_w$ and when $d \ll \lambda_w$. In the first case heat flow will be given by Stefan-Boltzmann law Eq.(7.10). Note that this expression is independent of the separation distance of the bodies since for these conditions heat transfer is dominated by propagating electromagnetic fields (illustrated in Figure7.6 a). At short distances (comparable with λ_w) fields generated by excitation of a surface mode contributes to the transfer of energy between the plates and the Eq. (7.10) is no longer valid. The intensity of these fields depends on the separation distance of the surfaces so that the transfer of electromagnetic energy also becomes dependent on the separation distance.

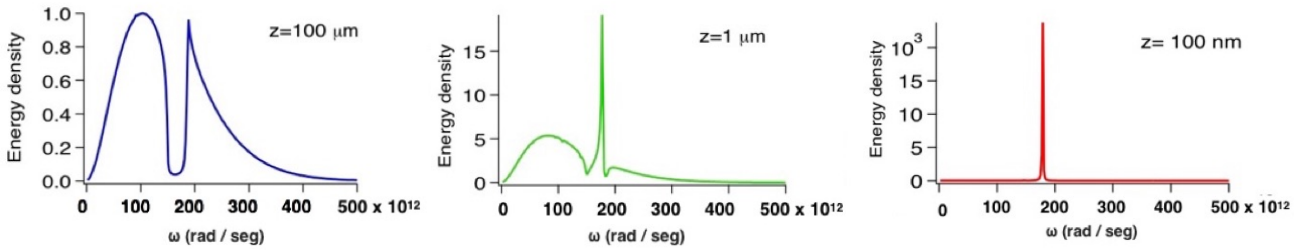

Figure 7.7: Theoretical calculations of the spectral density of energy radiated by a surface of SiC to T = 300 K measured at different distances z from the surface (21).

To further illustrate how evanescent modes contribute to energy transfer in Fig.7.7 theoretical calculations of the spectral density of radiated energy are shown by a surface of SiC at $300K$, at different distances from the surface including both propagating and evanescent fields (21). These calculations were carried out by assuming that the media is homogeneous and isotropic and modeled by a Lorentz dielectric function while the EM energy density was obtained using the Greens function written in plane wave basis. This system has a Wien wavelength of $\lambda_w = 7.6\mu$m. Figure 7.7 a) shows the spectral radiation density of the surface at a distance $d = 100\mu\text{m} \approx 13\lambda_w$. At this distance, the spectral energy density is similar to a Planckean curve (Eq. (7.6)), the difference is due to the fact that SiC is very reflective near $\omega = 170 \times 10^{12}$rad / s, so that the emissivity is small in this frequency range ($e = 1 - r$). At a distance slightly less than λ_w, $d = 1\mu\text{m} \approx \lambda_w/2$ the energy density changes drastically and an intense peak appears at a frequency $\omega = 178 \times 10^{12}\text{rad}/s$ which corresponds to the excitation of a system phonon. At $d = 100n\text{m} \approx 0.1\lambda_w$ the density of radiative energy becomes almost monochromatic. In the following sections it will be

seen how this peak of EM energy density found at the resonant frequency of the surface phonon of the system, $\omega = 178 \times 10^{12}$rad / s . It is also seen that at this frequency, the energy density increases more than four orders compared to the case of $d = 100\mu$m. In contrast to the Eq. 7.1 and 7.6, at separation distances smaller than λ_w, the radiative heat transfer becomes dependent on the separation distance and the spectral density of radiative energy tends to be consistent, and may increase orders of magnitude exceeding the limit established by the law of Stefan-Boltzmann (21, 105).

The phenomenon of heat transfer between bodies separated by nanometric distances has been treated theoretically since the seventies (95). Much of the work has been carried out using the theory of fluctuating electrodynamics introduced by Rytov (106). In summary, fluctuating electrodynamics proposes that thermal radiation is due to fluctuating load distributions and currents, generated by the thermal movement of charge carriers in a body at a temperature higher than absolute zero. The densities and currents generate fluctuating electromagnetic fields that can be obtained by calculating the Green function of the system. This formalism was first applied by Polder and Van Hove (95) to obtain a theoretical description of heat transfer between parallel plates. Polder and Van Hove obtained an analytical expression considering electromagnetic waves of different polarizations with respect to the surface and separating the contribution to the thermal radiation from the evanescent and propagating waves. Another problem that has been addressed is the heat flux between a sphere and a substrate at different temperatures (101, 107). In this system, the sphere is modeled as a point dipole with a Drude dielectric function. Dorofeyev calculated the Green function of a dipole in the presence of a flat surface (108), as well as the local fields of the sphere and the surface due to fluctuating sources in bodies (101). In this work, two peaks were found in heat transfer spectrum, one corresponding to the surface mode of the half-space and another to the surface mode of the sphere.

The near-field heat transfer between two media is a strong function of the geometry of bodies. Heat transfer calculations between two parallel media are the simplest case among different geometries. As a result, an overview of concepts used to calculate near-field heat flux between two parallel media has been presented. These concepts will be useful for the analysis of energy trnasfer between more complex nanostructured systems.

Theoretical Models: Non-planar geometries

As in the case of flat surfaces, in NPs systems, the excitation of surface modes increases the density of electromagnetic energy in the near field, so it is expected that the plasmonic

modes in NP systems play an important role in the transfer of heat (21). It is known that the dielectric function of the particle and geometric parameters such as shape and size, as well as interaction with another polarizable body, modify the plasmonic modes of the (14) system. Furthermore, in a system of two interacting particles separated by nanometric distances at different temperatures, the electromagnetic fields generated by thermal fluctuations can be coupled to the surface plasmonic modes of the system. Therefore, to study the transfer of heat between two particles, it is necessary to describe the surface modes in terms of their different geometric and dielectric parameters, since these modes would modulate heat transfer at nanometric distances.

The case of heat transfer between two spherical particles has been studied analytically, mainly under the dipolar approximation (107, 109). For example, Chapuis et al. (107) modeled the spheres with electric and magnetic dipoles and studied the dipole-electric dipole-magnetic interaction. Under this approach, a dependence is obtained with the center to center separation distance d, of $1/d^6$ for both magnetic and electric interaction (100). Other work, carried out by Manjavacas et al. (109) include interactions of the electric-dipole with the magnetic-dipole . They found that the crossed terms provide more interaction mechanisms, increasing the heat transfer compared to the model that only considers electrical-electric and magnetic-magnetic dipole interactions. However, magnetic contributions are only significant for metallic particles, due to the induced eddy currents.

The analytical dipolar models of radiative heat transfer between particles were compared with a numerical method performed by Domingues et al. (110). In this work, interaction between particles of the system was modeled by electrostatic potentials that take into account multipolar interactions beyond the dipole moment. For particles less than 2 nm in radius, they obtained good agreement with the dipolar model for separation distances between 8 and $100nm$. However, for distances less than 8 nm (4 times the radius of the particles) numerical simulations predict a transfer higher than that calculated by the dipolar model. The authors attribute the discrepancy to multipolar contributions that are not taken into account in the dipolar interaction model. Therefore, to describe the transfer of radiative heat at distances comparable to the sizes of the particles correctly, a description is required that takes into account multipolar moments beyond the dipolar.

Formalisms that consider multipolar moments have been proposed by Pérez-Madrid et al. (111) and Dorofeyev (101). Pérez-Madrid et al. they used a multipolar expansion method of the Coulomb interaction in the electrostatic approximation as well as a multipolar fluctuation-dissipation theorem. As a further approximation, Pérez-Madrid et al. worked

within the single scattering approximation, that is multiple scattering between particles was not taken into account. With this method, they calculated the heat transfer, as a function of the distance including interactions up to quadrupole order, which is the next multipolar order after the dipole moment. They compared their results with those obtained numerically by Domingues (110), obtaining a more significant agreement for separation distances less than four times the radius of the particles that the results obtained under the dipolar approximation. Dorofeyev established similar equations for the calculation of the radiative energy transfer between a sphere and a substrate including multipolar moments(101). He calculated the energy transfer between a surface and a silver sphere of 500 nm at a separation distance of 10^4nm including a maximum of 8 multipole moments within the single scattering approximation. However, a more in-depth study is needed of the contribution of multipolar moments at small distances, for example, an analysis of how the interaction of multipolar moments changes the system's modes as a function of the separation distance, and its influence on the flow of heat between the particles.

In this thesis, heat transfer in the quasi-static approach in NPs systems, depending on the parameters of the system such as size, separation distance, and dielectric properties is studied. The near electric field emitted at separation distances smaller than the thermal wavelength will be studied using a method that includes multipolar contributions and that allows systematic analysis of multipolar contributions to heat transfer and field augmentation. Also, it will be investigated how resonant modes can mediate the transfer of electromagnetic energy and how it depends on the dielectric and geometric parameters of the system.

Chapter 8

Model & Method

In this chapter a review of fluctuation electrodynamics is given. This has been the most commonly used analytical method in the study of near-field radiative heat transfer and is based on the fluctuation-dissipation theorem to describe fluctuating sources and the dyadic Greens function. This tool is already more than 60 years old and was developed in the 1950s by physicists in the former Soviet Union starting with Sergei M. Rytov (106). The method has been used to model energy transfer between parallel slabs separated by nano and micrometer and has fitted well with experimental results considering separations up to a few nanometers (112, 113). Afterwards, energy transfer between spherical NPs is obtained in the quasistatic approximation which relies on the multipolar decomposition of the fluctuating fields and the NP response. This is then used within the multipolar spectral representation to obtain a new method for calculating radiative heat transfer which includes full multipolar interactions and permits an analysis of how couple modes of the system contributes to energy transfer.

8.1 Fluctuational electrodynamics

Maxwell's equations describe the relationship between EM fields, and charge and current densities within a system. The constitutive equations complete the description by providing a relationship between EM fields and the response of the material that comprises the system. For example, absorption of radiation by a body can be related to the imaginary part of its dielectric function and the field scattered by a body can be calculated directly from the Maxwell equations by applying the appropriate boundary conditions. However, emission of radiation due to thermal movement of the charge carriers is not included in Maxwell's equations. The electrodynamic theory of fluctuations, introduced by Rytov (106), serves as a link between Maxwell's equations and thermal radiation and has been one of the

most widely used methods for calculating radiative heat transfer at the nanoscale (114). In the following section, Rytovs theory is briefly outlined, highlighting the fundamental concepts and methods used to calculate thermal EM fields. A review is given, implementing macroscopic electrodynamics, where the material response is assumed to happen locally. Ohm's law, for example, is written $\vec{j} = \sigma\vec{E}$ where all quantities are evaluated at the same $(\vec{r}, \omega)$. In metals, this approximation is expected to work on spatial scales longer than the mean free path of charge carriers and the Fermi wavelength. To the same level of approximation, interfaces between materials are assumed to be 'sharp.' The permittivity $\epsilon(\vec{r}, \omega)$, for example, varies like a step function across the boundary. This is accompanied by suitable boundary conditions for the macroscopic fields. The other approximation that is commonly applied is the linearity of the response of the system to external EM fields. The linear approximation provides a simple link between the probability distributions of the random forces and the field, yielding eventually to statistics which are completely characterized by mean values and the correlation spectra, described in the fluctuation-dissipation theorem (FDT).

Fluctuating currents and charge distributions

From a microscopic point of view the source of thermally emitted EM fields are fluctuating charge and current densities produced by random thermal movement of the constituents of a body, such as electrons, atoms or ions. However, fluctuational electrodynamics works at a macroscopic level, so that thermal EM fields are modeled as produced by fluctuations of volume densities of charges and currents. In other words, the electromagnetic field are produced by sources that are also macroscopic i e. charge and current volume densities. Fluctuational electrodynamics is built on this simple macroscopic description. Fluctuating charge and current sources depend on the temperature and dielectric properties of the body and are denoted by $\rho(0)$ and $\vec{j}^{(0)}$ respectively. This assumes a macroscopic material system whose internal temperature imposes the steady state properties of the radiation field. The sources are unable to thermalize by themselves and are taken to be in thermal equilibrium with a heat bath. Fluctuating sources emit thermal EM fields, $\vec{E}^{(0)}$ and $\vec{B}^{(0)}$, that act as external fields when interacting with other polarizable bodies in the system. The physical description of fluctuating sources, relies on the assumption that each emitting body in the system is at a local equilibrium temperature T. Consequently, fluctuating charges and currents generated by thermal random movement satisfy the conditions

$$\left\langle \rho^{(0)}(\vec{r}, t) \right\rangle = 0, \qquad \left\langle \vec{j}^{(0)}(\vec{r}, t) \right\rangle = 0, \tag{8.1}$$

where $\langle ... \rangle$ indicates a statistical average over all possible values of $\rho^{(0)}$ and $\vec{j}^{(0)}$ at a given time t. This condition states that there is no creation or destruction of charge due to thermal movement, and that averaged charge and current distributions are zero. The total charge and current densities in a given system can be separated into a fluctuating and external part. The external charge and density refers to any charge in the system that is not due to thermal fluctuations, so that the total charge is given by

$$\rho(\vec{r},t) = \rho^{(0)}(\vec{r},t) + \rho^{ext}(\vec{r},t), \qquad \vec{j}(\vec{r},t) = \vec{j}^{(0)}(\vec{r},t) + \vec{j}^{ext}(\vec{r},t). \tag{8.2}$$

The fluctuating sources can be described by its temporal autocorrelation function, defined as the average of a given variable of the system $\langle X(t)X(t')\rangle$, where $X = \rho, \vec{J}_\alpha$, and where the statistical average is taken over all possible values of variable X at time t and t' (114). It is convenient to use the Fourier transform of the autocorrelation function, for which the Wiener-Khinthcin theorem is used. This theorem states that Fourier components of autocorrelation functions with different frequencies are zero (115, 116). The autocorrelation function can be written as

$$\left\langle X(\vec{r},t), X(\vec{r'},t') \right\rangle = \int_{-\infty}^{\infty} \frac{d\omega}{2\pi} e^{i\omega(t-t')} \left\langle X(\vec{r},\omega), X(\vec{r'},\omega) \right\rangle \tag{8.3}$$

where as a consequence of the Wiener-Khinthcin theorem, there is no correlation between terms with different frequencies, so that $\langle X(\vec{r},\omega)X(\vec{r}',\omega')\rangle = 2\pi \langle X(\vec{r},\omega)X(\vec{r}',\omega')\rangle \delta(\omega - \omega')$. A connection between $\langle X(\vec{r},\omega)X(\vec{r}',\omega)\rangle$ and the local temperature of the body can be established by means of the FDT, which is a semi-classical approach that uses quantum theory to describe macroscopic quantities. The FDT can be seen as a general relationship between the microscopic fluctuations of a linear dissipative body in thermal equilibrium to its macroscopic parameters (resistance and temperature). Simply stated, it draws a relationship between the fluctuations of a dynamical variable of a system in thermodynamic equilibrium and the dissipative properties of the body in the presence of an external perturbative force.

To outline the principal concepts behind the FDT, consider a dynamical variable of a given system, denoted by X, which couples to an external force $f(t)$ in the following manner

$$\varepsilon = -Xf(t), \tag{8.4}$$

and assume that a linear relation exists between the driving force and the variable X,

$$X(\omega) = \alpha(\omega)f(\omega), \tag{8.5}$$

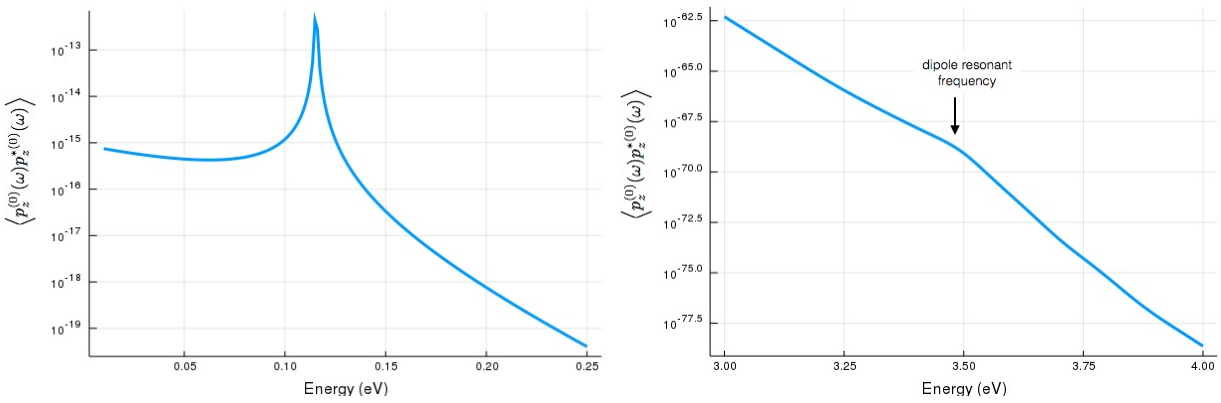

Figure 8.1: Current density spectrum for SiC (top) and Ag (bottom) near the isolated particle resonant frequencies calculated at 300 °K.

where $\alpha(\omega)$ is known as a generalized susceptibility corresponding to variable X and force f. The FDT establishes a relation between fluctuations of X and susceptibility α when the system is in thermal equilibrium at temperature T (114)

$$\langle X(\omega)X^*(\omega')\rangle = \frac{4\pi}{\omega}\mathrm{Im}\left[\alpha(\omega)\right]\Theta(\omega,T)\delta(\omega-\omega'), \tag{8.6}$$

where

$$\Theta(\omega,T) = \frac{\hbar\omega}{e^{\hbar\omega/k_BT}-1} \tag{8.7}$$

is the average energy of a quantum harmonic oscillator in thermal equilibrium at temperature T. An outline of a derivation of the FDT is found in Appendix B. From the relation given in equation (8.6), it can be seen that the FDT can be used either to derive the susceptibility of a system based on an analysis of its thermal fluctuations, or to derive properties of its fluctuations using a known susceptibility. By means of the FDT, fluctuational electrodynamics can describes thermal EM fields in terms of the susceptibility and temperature of the body that generates them.

To illustrate these concepts, consider the fluctuating dipole moment, $\vec{p}^{(0)}$ induced on a spherical particle due to random thermal motion of its charge carriers. Consider small homogeneous particle in vacuum with complex dielectric function $\epsilon(\omega)$, so that the polarizability of the particle can be described by the equation

$$\alpha(\omega) = a^3\left(\frac{\epsilon(\omega)-1}{\epsilon(\omega)+2}\right).$$

Using Eq. (8.6), the correlation function of the fluctuating dipole moment can be written as

$$\left\langle p_k^{(0)}(\vec{r},\omega)p_l^{*(0)}(\vec{r}',\omega)\right\rangle = \frac{4\pi}{\omega}\Theta(\omega,T)\mathrm{Im}[\alpha(\omega)]\delta(\omega-\omega')\delta_{lk}. \tag{8.8}$$

From Eqs. (8.8) and (8.7) it can be seen that the fluctuating dipole depends the polarizability $\alpha(\omega)$ and on the function Θ. The dipole correlation function will therefore increase near the poles of the polarizability $\alpha(\omega)$. However, at room temperature $\Theta(T,\omega)$ is many order of magnitude larger near infrared frequencies than in the visible spectrum, and falls off exponentially where the plasmon resonances of metals are usually found. It is therefore expected that the correlation function of the dipole moment to be much smaller for metals than dielectrics.

To illustrate, the spectral correlation function of the fluctuating dipole moment within 10 nm Ag and SiC NPs at room temperature is calculated. Since this work focuses on the coupling of thermal EM with the surface modes of NPs, the current density is plotted near the resonant frequencies of a SiC and Au spherical NP as can bee seen in Fig.8.1. For the case of SiC, the resonant frequency of the optical mode is found near 0.1 eV, at infrared wavelength, where as for Ag it is found in the visible range, near 3.5 eV. At these energy range fluctuating currents are orders of magnitude larger for SiC than in Ag. Since $\Theta(\omega,T)$ decreases at larger energies, the resonance of the Ag particles is only visible as a small shoulder, while the resonance of the SiC particle can be clearly appreciated. Since resonances in metals are usually in the visible part of the spectrum while those of, they are much more difficult to thermally excite than dielectrics.

Maxwell equations with fluctuating sources

By introducing fluctuating sources into Maxwells equations it is possible to obtain a description of the EM fields emitted by a body at a temperature $T > 0$. To this, consider Maxwell's equations

$$\begin{aligned} \nabla\cdot\vec{D}(\vec{r},t) &= 4\pi\rho(\vec{r},t), \qquad \nabla\times\vec{E}(\vec{r},t) = -\frac{1}{c}\frac{\partial}{\partial t}\vec{B}(\vec{r},t), \\ \nabla\cdot\vec{B}(\vec{r},t) &= 0, \qquad \nabla\times\vec{H}(\vec{r},t) = \frac{4\pi}{c}\vec{J}(\vec{r},t) + \frac{1}{c}\frac{\partial}{\partial t}\vec{D}(\vec{r},t), \end{aligned} \tag{8.9}$$

where $\vec{E}$ is an electric field and $\vec{B}$ is a magnetic induction. The displacement field $\vec{D}$ and magnetic field $\vec{H}$ are defined as

$$\begin{aligned} \vec{D} &= \vec{E} + 4\pi\vec{P}, \\ \vec{H} &= \vec{B} - 4\pi\vec{M}, \end{aligned} \tag{8.10}$$

where $\vec{P}$ and $\vec{M}$ are the electric polarization and magnetization respectively, while $\rho(\vec{r},t)$ and $\vec{J}(\vec{r},t)$ are charge and current densities. Equations (8.9) describe the relationship

between sources $(\rho, \vec{J})$, dielectric properties of the material and the resulting EM fields $(\vec{E}, \vec{B})$. Eqs. (8.9) in frequency space are

$$\begin{aligned} \nabla \cdot \vec{D}(\vec{r},\omega) &= 4\pi\rho(\vec{r},\omega), \qquad \nabla \times \vec{E}(\vec{r},\omega) = -\frac{1}{c} i\omega \vec{B}(\vec{r},\omega), \\ \nabla \cdot \vec{B}(\vec{r},\omega) &= 0, \qquad \nabla \times \vec{H}(\vec{r},\omega) = \frac{4\pi}{c}\vec{J}(\vec{r},\omega) + \frac{1}{c} i\omega \vec{D}(\vec{r},\omega). \end{aligned} \tag{8.11}$$

The central idea of fluctuational electrodynamics, is to add fluctuating sources $\rho^{(0)}$ and $\vec{J}^{(0)}$, in Maxwell's equation (117). We add the superscript (0) to differentiate from external sources, that do not depend on the temperature of the system. The total charge and current densities can be inserted in Eqs.(8.9). The present work focuses on the case when there is an absence of external sources, so that Eq.(8.2) only has a fluctuating term. Maxwell's equations are reduced to

$$\begin{aligned} \nabla \cdot \vec{D}(\vec{r},\omega) &= 4\pi\rho^{(0)}(\vec{r},\omega), \qquad \nabla \times \vec{E}(\vec{r},\omega) = -\frac{1}{c} i\omega \vec{B}(\vec{r},\omega), \\ \nabla \cdot \vec{B}(\vec{r},\omega) &= 0, \qquad \nabla \times \vec{H}(\vec{r},\omega) = \frac{4\pi}{c}\vec{J}^{(0)}(\vec{r},\omega) + \frac{1}{c} i\omega \vec{D}(\vec{r},\omega), \end{aligned} \tag{8.12}$$

consequently fields $\vec{E}$, $\vec{D}$, $\vec{B}$ and $\vec{H}$ are fluctuating and satisfy the conditions $\left\langle \vec{X} \right\rangle = 0$ where $\vec{X} = \vec{E}, \vec{D}, \vec{B}, \vec{H}$. These equations must be solved in addition with adequate boundary conditions to take into account discontinuities at the interface between media. Furthermore, the theory assumes that $\rho^{(0)}$ and $\vec{J}^{(0)}$ act as isolated sources, in the sense that they are not effected by the EM fields, and only depend on the temperature and dielectric properties of the emitting body (117).

A method commonly used to solve Maxwell's equations is by using the Green function. In frequency space, the fluctuating sources and the fields they generate are related by means of (18)

$$\begin{aligned} \vec{E}(\omega,\vec{r}) &= i\omega\mu_0 \int_V d\vec{r}' \mathbf{G}^E(\vec{r},\vec{r'},\omega) \cdot \vec{J}^{(0)}(\omega,\vec{r'}), \\ \vec{H}(\omega,\vec{r}) &= \int_V d\vec{r}' \mathbf{G}^H(\vec{r},\vec{r'},\omega) \cdot \vec{J}^{(0)}(\omega,\vec{r'}), \end{aligned} \tag{8.13}$$

where $\mathbf{G}^H$ y $\mathbf{G}^E$ are second-order tensors known as magnetic and electric Green functions. These relate the current density at a point $r^{\vec{prime}}$ with the electric and magnetic fields at another point $\vec{r}$. Due to the linear relation that exists between the source and the field, and by using condition $\left\langle \vec{J}^{(0)}(\vec{r},t) \right\rangle = 0$, it can be concluded that the statistical average of the EM fields is also zero. However, quantities of the form

$$\left\langle E_i(\vec{r},\omega) E_j^*(\vec{r}',\omega') \right\rangle = -\omega\omega'\mu_0^2 \int d\vec{r}'' \int d\vec{r}''' \mathbf{G}_{ik}^E(\vec{r},\vec{r}'',\omega) \mathbf{G}_{jn}^{*E}(\vec{r}',\vec{r}''',\omega') \left\langle J_k^{(0)}(\vec{r}'',\omega) J_n^{*(0)}(\vec{r}''',\omega') \right\rangle .$$

are written in terms of $\left\langle J_k^{(0)}(\vec{r}'',\omega)J_n^{*(0)}(\vec{r}''',\omega')\right\rangle$ which is related to the temporal correlation function of $\vec{J}^{(0)}(\vec{r}'',t)$. To illustrate this, consider de following temporal correlation function

$$\left\langle J_n^{(0)}(\vec{r},t)J_k^{*(0)}(\vec{r},t')\right\rangle, \tag{8.14}$$

where J_n y J_k are the Cartesian coordinates of the current density $\vec{j}(\vec{r},t)$. The temporal Fourier transform is

$$\vec{J}(\vec{r},t)=\int_{-\infty}^{\infty}\vec{J}(\vec{r},\omega)e^{-i\omega t}d\omega,$$

substituting in Eq. (8.14)

$$\left\langle \vec{J}_n^{(0)}(\vec{r},t)\vec{J}_k^{*(0)}(\vec{r},t')\right\rangle=\int_{-\infty}^{\infty}\int_{-\infty}^{\infty}\left\langle J_k^{(0)}(\vec{r},\omega)J_n^{*(0)}(\vec{r},\omega')\right\rangle e^{i(\omega t-\omega' t')}d\omega d\omega'. \tag{8.15}$$

In general, terms of the form $\left\langle J_k^{(0)}(\vec{r},\omega)J_n^{*(0)}(\vec{r},\omega')\right\rangle \neq 0$ and can be written in terms of the system's temperature using the FTD. Due to this property, the statistical average of physical quantities of the form $\left\langle \vec{E}(\vec{r},\omega)\cdot\vec{H}^*(\vec{r}',\omega')\right\rangle$, $\left\langle \vec{E}(\vec{r},\omega)\cdot\vec{E}^*(\vec{r}',\omega')\right\rangle$ and $\left\langle \vec{H}(\vec{r},\omega)\cdot\vec{H}^*(\vec{r}',\omega')\right\rangle$ as well as the Poynting vector and the EM energy density will be different than zero.

8.2 Near-field power exchange: quasi-static approximation

In the previous section Maxwell's equations with fluctuating sources were introduced, as well as a commonly used method to solve them. In this section, the problem of energy transfer between spherical NPs with small radii compared to thermal wavelength, separated by nanometric distances is approached. For these cases a quasi-static approach can be used, and Maxwell's equations are significantly simplified. In this section a new method that takes into account full multipolar interaction between NPs and separates the dielectric and geometric parameters of the system is proposed. This was achieved by a modification of the spectral representation presented in the first part of this thesis. By taking into account full interaction, the spectral representation method allows identification of each coupled mode and its contribution to energy transfer as the dielectric and geometric parameters of the system are varied. Furthermore, the system's eigenmodes can be calculated once the geometrical parameters are fixed. By correctly choosing the dielectric properties of the particles, the calculated eigenmodes can then me used to enhance or suppress energy transfer.

First consider the case of two non-overlapping, non-magnetic, polarizable spheres of radii a with complex dielectric function $\epsilon(\omega)$ at temperatures T_1 and T_2 respectively, immersed in a host medium characterized by dielectric constant ϵ_h and located at positions $\vec{R}_1$ and $\vec{R}_2$, where $R = |\vec{R}_2 - \vec{R}_1|$. A schematic model is shown in Figure (8.2). In the previous part of this thesis we studied the modification of the local electric field due to the charges induced on polarizable particles by an external field. In this case, random thermal movement of charge carriers in each particle generate fluctuating charge distributions which produce thermal electric fields. The thermal fields, which now take the role of the "external fields" of the previous section, induce charges on neighboring particles. Induced charges on each particle in the system then interact with each other through the near-field.

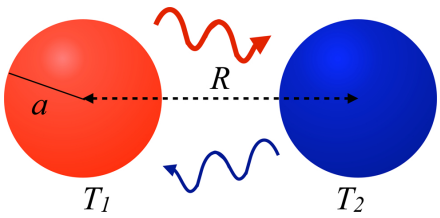

Figure 8.2: Schematic illustration of the interaction between two particles of radius a with center to center separation distance R with temperatures T_1 and T_2.

The rate of energy transfer, or power exchange, from particle 2 to 1 is given by (118**?**)

$$W_{2\to1} = -\int_{v_1} \left\langle \vec{J}_1^{ind}(\vec{r},t)\cdot\vec{E}_2(\vec{r},t)\right\rangle dv \tag{8.16}$$

where $\vec{J}_1^{ind}(\vec{r},t)$ is the induced density current in particle 1, $\vec{E}_2(\vec{r},t)$ is the total field produced by particle 2, the brackets represent an average in the statistical sense, i.e. as an averaging over the probabilities of all possible values at time t (114), and the integral is performed over v_1, the volume of particle 1. In the quasi-static regime, the above equation can be integrated by parts, and by use of the continuity equation, $\nabla\cdot\vec{J}(\vec{r},t) = -\partial\rho(\vec{r},t)/\partial t$, and the divergence theorem, (**?**) recast as

$$W_{2\to1} = -\int_{v_1} \left\langle \left[\frac{\partial}{\partial t}\rho_1^{ind}(\vec{r},t)\right] V_2(\vec{r},t)\right\rangle dv, \tag{8.17}$$

where $\rho_1^{ind}(\vec{r},t)$ is the induced charge distribution on particle 1 and $V_2(\vec{r},t)$ is the scalar potential, such that, $-\nabla V_2(\vec{r},t) = \vec{E}_2(\vec{r},t)$.

Taking the Fourier transform, $A(t) = \frac{1}{2\pi}\int_{-\infty}^{\infty} A(\omega)e^{-i\omega t}d\omega$, of both quantities in the integral of Eq. (8.17) and deriving respect time, obtain

$$W_{2\to1} = \frac{1}{4\pi^2}\int_{-\infty}^{\infty}\int_{-\infty}^{\infty} i\omega\left[\int_{v_1}\left\langle\rho_1^{ind}(\vec{r},\omega)V_2(\vec{r},\omega')\right\rangle dv\right] e^{-i(\omega+\omega')t}d\omega d\omega'. \tag{8.18}$$

By taking the multipolar expansion of the potential, $V_2(\vec{r},\omega) = \sum_\mu V_{\mu 2}(\omega) r^\mu Y_\mu(\hat{r})$ (18), where $Y_\mu(\hat{r})$ are the spherical harmonics of order μ, with $r = |\vec{r}|$ and $\hat{r} = \vec{r}/r$; the volume integral in Eq. (8.18) can be carried out, such that, it is written as

$$W_{2\to1}(\omega) = \frac{1}{4\pi^2}\int_{-\infty}^{\infty}\int_{-\infty}^{\infty} i\omega \sum_\mu \left\langle Q_{\mu 1}^{*ind}(\omega) V_{\mu 2}(\omega')\right\rangle e^{-i(\omega+\omega')t} d\omega d\omega' \,. \tag{8.19}$$

Here, $V_{\mu 2}(\omega)$ is the corresponding μ-th term of the total potential due to particle 2 and the μ-th multipolar charge distribution is given as, $Q_\mu(\omega) = \int_v r^\mu \rho(\vec{r},\omega) Y_\mu^*(\hat{r}) dv$, where $(*)$ means complex conjugated. Thus, $Q_{\mu 1}^{*ind}(\omega)$ is the complex conjugate of the μ-th multipole moment on particle 1. Assuming a linear response by the particles to the total external potential, the μ-th multipole moment satisfies the relation, $Q_{\mu 1}(\omega) = -\alpha_{\mu 1}(\omega) V_{\mu 2}(\omega)$, where $\alpha_{\mu 1}(\omega)$ is the particles multipolarizability, so that Eq. (8.19) can be recast as

$$W_{2\to1}(\omega) = -\frac{1}{4\pi^2}\int_{-\infty}^{\infty}\int_{-\infty}^{\infty} i\omega \sum_\mu \left\langle \alpha_{\mu 1}^*(\omega) V_{\mu 2}^*(\omega) V_{\mu 2}(\omega')\right\rangle e^{-i(\omega+\omega')t} d\omega d\omega' \tag{8.20}$$

To further simplify Eq. (8.20) $V_{\mu 2}(\omega)$ need to be related to the fluctuating multipoles on particles 2. It can be achieved by noting that a linear relation exists between ρ_2^0, the fluctuating charge density in particle 2 and $V_2(\vec{r})$, due to the Maxwell equations. A multipolar derivation of the rate of energy transfer or power exchange is presented in the following subsection.

8.3 Multipolar spectral representation with fluctuating sources

The total charge density on a given particle can be written as $\rho = \rho^{(0)} + \rho^{ind}$, where $\rho^{(0)}$ is the fluctuating charge density due to the thermal movement of the particles charge carriers and ρ^{ind} is the induced charge due to interaction between particles. Consequently, the μ-th multipole moment on particle i can be written as the sum

$$Q_{\mu i} = Q_{\mu i}^{(0)} + Q_{\mu i}^{ind}, \tag{8.21}$$

where i can be 1 or 2, and $Q_{\mu i}^{(0)}$ represent the fluctuating multipole terms due to $\rho^{(0)}$ and $Q_{\mu i}^{ind}$ the induced multipole moments due to ρ^{ind}. We stress that $Q_{\mu i}^{(0)}$, unlike $Q_{\mu i}^{ind}$, depends only on the properties of particle i, such as temperature and dielectric function, but not on the system configuration, such as number of particles, their separation distances or interaction with other polarizable objects.

The μ-th component of the multipolar expansion of the potential acting on particle i can be written as

$$V_{\mu i} = V_{\mu i}^{(0)} + V_{\mu i}^{ind}, \tag{8.22}$$

where $V_{\mu i}^{(0)}$ and $V_{\mu i}^{ind}$ are the potentials due to neighboring particle charge distributions $\rho^{(0)}$ and ρ^{ind} respectively. The interaction term $V_{\mu i}^{ind}$ is expected to fall off to zero as the separation distance between particles increases. In this manner, $V_{\mu i}^{(0)}$ can be thought of as the potential generated by the fluctuating sources in the absence of interaction i.e. as if it were an isolated particle. As particles are brought together, the term $V_{\mu i}^{(0)}$ induces charge distributions on neighboring particles, which in turn give rise to $V_{\mu i}^{ind}$. The potential written in Eq. (8.22) acts on particle i and induces a multipole moment given by $Q_{\mu i}^{ind} = -\alpha_{\mu i}(\omega) V_{\mu i}$.

Potential $V_{\mu i}$ can be further decomposed, writing it in terms of the multipoles on the neighboring particle, indexed by i':

$$\begin{aligned} V_{\mu i} &= \sum_{\mu'} (-1)^{\mu'} A_{\mu i}^{\mu' i'} Q_{\mu' i'} \\ &= \sum_{\mu'} (-1)^{\mu'} A_{\mu i}^{\mu' i'} \left[Q_{\mu' i'}^{(0)} + Q_{\mu' i'}^{ind} \right] \end{aligned} \tag{8.23}$$

where $A_{\mu i}^{\mu' i'}$ is the matrix defined in Eq. (4.11). Recall that $A_{\mu i}^{\mu' i'}$ is a matrix that describes the expansion of the total potential about the center of the i-th particle, as a sum over the μ' multipoles of the i'-th particle. Using Eq. (8.23), the induced multipolar moment are obtained as:

$$Q_{\mu i}^{ind} = -\frac{2l+1}{4\pi} \alpha_{\mu i}(\omega) \sum_{i' \neq i} \sum_{\mu'} (-1)^{\mu'} A_{\mu i}^{\mu' i'} \left[Q_{\mu' i'}^{(0)} + Q_{\mu' i'}^{ind} \right] \tag{8.24}$$

where $\alpha_\mu i$ is the multipolarizability of the i-th sphere given in Eq. (4.12). A system of equations for the induced multipoles Q_{lmi}^{ind}, are obtained as:

$$\sum_{l' m' i'} \left[-u(\omega) \delta_l^{l'} \delta_m^{m'} \delta_i^{i'} + H_{lmi}^{l' m', i'} \right] x_{l' m', i'} = f_{lm,i}, \tag{8.25}$$

where

$$x_{lm,i} = \frac{Q_{lm,i}^{ind}}{(l a_i^{2l+1})^{1/2}}, \qquad f_{lm,i} = -\frac{(l a_i^{2l+1})^{1/2}}{4\pi} \sum_{i'' \neq i} \sum_{l'' m''} (-1)^{l''} A_{lm,i}^{l'' m'', i''} Q_{l'' m', i''}^{(0)},$$

$$H_{lm,i}^{l' m', i'} = n_0^l \delta_{ll'} \delta_{mm'} \delta_{ii'} + (-1)^{l'} \frac{(l l' a_i^{2l+1} a_{i'}^{2l'+1})^{1/2}}{4\pi} A_{lm,i}^{l' m', i'}. \tag{8.26}$$

and where $u(\omega)$ is a complex spectral variable defined as $u(\omega) = \frac{1}{1 - \epsilon(\omega)/\epsilon_h}$. In matrix form we obtain

$$\left[-u(\omega) \mathbf{I} + \mathbf{H} \right] \vec{X} = \vec{F}, \tag{8.27}$$

where $\vec{X}$ and $\vec{F}$ are vectors whose corresponding elements are $x_{\mu i}$ and $f_{\mu i}$, as defined in Eq. (8.26). These equations are equivalent to Eqs.(4.14), however the sources now are of a fluctuating nature. The Greens matrix solutions method can then be carried over to this problem. The systems Green function is now

$$G_{\mu i}^{\mu' i'}(\omega) = -\sum_{\mu'' i''} \frac{U_{\mu}^{\mu''} (U^{-1})_{\mu''}^{\mu'}}{u(\omega) - n_{\mu''}}, \tag{8.28}$$

where $\mathbf{U}$ is the unitary matrix that diagonalizes $\mathbf{H}$, such that $\mathbf{U}^{-1}\mathbf{H}\mathbf{U} = \mathbf{n}$, where $\mathbf{n}$ is a diagonal matrix formed by the real and positive eigenvalues of $\mathbf{H}$. It is important to point out that while resonant conditions of the coupled modes are given by the poles of the Green function, resonant conditions for the isolated modes can be obtained from the poles of the polarizabilities Eq. (4.12), which are satisfied whenever $\mathrm{Re}[u(\omega_s^0)] = n_s^0$. Moreover, as particle separation increases eigenvalues n_s tend to n_0^s and resonant frequencies of the coupled modes tend to those of isolated modes: $\omega_s \to \omega_s^0$.(82).

Solutions to Eq. (8.27) are found by

$$\vec{X} = \mathbf{G}\vec{F}, \tag{8.29}$$

which establishes a method for obtaining the multipole moments. Once multipole moments are obtained, the total potential can be calculated and set in terms of $Q_{\mu}^{(0)}$. Using Eq. (8.29) and Eq. (8.23) in Eq. (8.22), the μ-th term of the potential acting on particle i can be written in the form

$$V_{\mu i} = \sum_{\mu'} \chi_{\mu i}^{\mu' i'}(\omega) Q_{\mu' i'}^{(0)}, \tag{8.30}$$

where $\chi_{\mu i}^{\mu' i'}(\omega)$ are components of a matrix given by

$$\chi_{\mu i}^{\mu' i'}(\omega) = \sum_{\mu'' \mu'''} (-1)^{\mu''} A_{\mu i}^{\mu'' i'} \left[\frac{(-1)^{\mu'+1} (a_{i'}^{2\mu''+1} \mu'' a_i^{2\mu'''+1} \mu''')^{1/2}}{4\pi} A_{\mu''' i}^{\mu' i'} G_{\mu'' i'}^{\mu''' i}(\omega) + \delta_{\mu''}^{\mu'} \right]. \tag{8.31}$$

From the above equation it is possible to identify terms describing different contributions to potential $V_{\mu i}$. For instance, the first term describes interaction between induced multipoles and retains information of coupled modes through Greens function $G_{\mu''}^{\mu'''}(\omega)$. Meanwhile, the second term in Eq. (8.31) describes first interaction of the thermal fields with particles, i.e., the single scattering approximation or without coupling. Dependence of each term on particle separation distance can be obtained using Eq. (**??**) where, $A_{\mu}^{\mu'} \propto 1/R^{\mu+\mu'+1}$. Therefore first terms in brackets in Eq. (8.31) fall off as $1/R^{\mu+\mu'+\mu''+\mu'''+2}$ while second terms as $1/R^{\mu+\mu''+1}$. Consequently, terms describing interaction fall off more rapidly than

those without coupling. Thus, at large separation distances, single scattering terms will dominate and interaction terms will be negligible. However, at short separation distance the interaction terms can modify the near-field and now, they are not longer negligible.

8.4 Eigenmode Description of Power Exchange

In Eq. (8.20) an expression that describes power exchange between particles in the quasi-static limit and a relation between the multipolar moments on each particle and the total potential Eq. (8.31) was presented. Using these expressions in Eq. (8.20) a multipolar representation of energy transfer is obtained

$$W_{2\to1}(\omega) = -\frac{1}{4\pi^2}\int_{-\infty}^{\infty}\int_{-\infty}^{\infty} i\omega \sum_{\mu,\mu',\mu''} \alpha^{*}_{\mu 1}(\omega)\chi^{*\mu' 2}_{\mu 1}(\omega)\chi^{\mu'' 2}_{\mu 1}(\omega') \times \left\langle Q^{*(0)}_{\mu' 2}(\omega) Q^{(0)}_{\mu'' 2}(\omega')\right\rangle e^{-i(\omega+\omega')t} d\omega d\omega' . \tag{8.32}$$

Using the fluctuation-disipation theorem given by (111, 118)

$$\left\langle Q^{*(0)}_{\mu i}(\omega) Q^{(0)}_{\mu' i'}(\omega')\right\rangle = \frac{4\pi}{\omega}\Theta\left(T_i,\omega\right)\mathrm{Im}[\alpha_{\mu i}(\omega)]\delta(\omega'+\omega)\delta_{\mu\mu'}\delta_{ii'}, \tag{8.33}$$

where $\Theta\left(T_i,\omega\right) = \frac{\hbar\omega}{e^{\hbar\omega/k_B T}-1}$, Eq. (8.32) takes the form

$$W_{2\to1} = \int_0^{\infty}\frac{2}{\pi}\sum_{\mu,\mu'}\mathrm{Im}[\alpha_{\mu 1}(\omega)]\mathrm{Im}[\alpha_{\mu' 2}(\omega)]\left|\chi^{\mu' 2}_{\mu 1}(\omega)\right|^2\Theta(T_2,\omega)d\omega. \tag{8.34}$$

Here, each particle is taken to be in local thermal equilibrium allowing the fluctuating multipole moments to be characterized by the fluctuation-dissipation theorem.

Calculating an equivalent quantity for the power exchange from particle 1 to particle 2, the net power exchange at frequency ω between particles is

$$\begin{aligned} W(\omega) &= W_{2\to1}(\omega) - W_{1\to2}(\omega) \\ &= \frac{2}{\pi}\sum_{\mu,\mu'}\mathrm{Im}[\alpha_{\mu 1}(\omega)]\mathrm{Im}[\alpha_{\mu' 2}(\omega)]\left|\chi^{\mu'}_{\mu}(\omega)\right|^2\left\{\Theta(T_2,\omega)-\Theta(T_1,\omega)\right\}. \end{aligned} \tag{8.35}$$

where $\left|\chi^{\mu' 2}_{\mu 1}(\omega)\right| = \left|\chi^{\mu' 1}_{\mu 2}(\omega)\right|$ is used and therefore omit the i and i' indexes. In the case of more than two particles, a quantity equivalent to Eq. 8.35 can be calculated for the set of particles i and j by a simple substitution of indexes. Total power exchange is found by integrating over all frequencies, and can be cast into the form

$$W_{\mathrm{tot}} = \int_0^{\infty}\Phi(\omega)\left\{\Theta(T_2,\omega)-\Theta(T_1,\omega)\right\}d\omega, \tag{8.36}$$

where

$$\Phi(\omega) = \frac{2}{\pi} \sum_{\mu,\mu'} \mathrm{Im}[\alpha_{\mu 1}(\omega)] \mathrm{Im}[\alpha_{\mu' 2}(\omega)] \left| \chi_{\mu}^{\mu'}(\omega) \right|^2, \tag{8.37}$$

is a dimensionless generalized flux that carries the geometric and dielectric parameters of the system. From Eq. (8.37) notice that the generalized flux depends on particle radius and separation distances through the polarizablities and through $\chi_{\mu}^{\mu'}(\omega)$. Naturally, larger volumes and closer proximity between particles, lead to larger flux. Furthermore, from Eq. (8.37) it can be seen that $\Phi(\omega)$ will increase when $\mathrm{Im}[\alpha_{\mu}]$ or $\chi_{\mu}^{\mu'}(\omega)$ are large. It can be associated with two frequency-dependent mechanisms which modulate the generalized flux: the excitation of isolated particle modes, given through the multipolarizabilities, and excitation of the system's coupled modes, given through $\chi_{\mu}^{\mu'}(\omega)$. Recall that resonant conditions of the isolated modes are met when $u(\omega) = n_l^0$, while those for coupled modes when $u(\omega) = n_{\mu}$, with the additional condition that $\mathrm{Im}[u(\omega)] \ll 1$. Consequently, the inclusion of coupled modes provide an additional mechanism through which energy can be transferred, mainly when resonant conditions are met.

8.5 Method outline: heat transfer

In this section we outline the procedure to obtain the radiative energy transfer in a system of NPs.

1. Dielectric parameters: Choose the NPs and host matrix material and the corresponding model dielectric function.

2. Geometric parameters: The number of particles, particle radius, positions and temperatures are defined. We point out that the SR allows the modeling of particles of different particle sizes, as long as radi are smaller than the exciting wavelength.

3. Calculation of geometric matrices: Once the geometric parameters are defined, the matrices **A** and **H** can be calculated using Eqs. (4.11) and (8.26) respectively. These matrices only depend on the geometric parameters of the system and are completely defined once the particle radii and positions are chosen.

4. Calculation of Green's Matrix: Once matrix **H** is obtained, its eigenvectors and eigenvalues are calculated via an eigen decomposition method. Using the spectral variable, eigenvectors and eigenvalues, Eq. (4.16) is used to calculate the Greens matrix at a given frequency. The Green matrix holds the information of the system's normal

modes. Resonant frequencies of the system can be found by calculating the poles of the matrix.

5. Using interaction matrix **A** and the Green matrix **G** we can define the response matrix χ shown in Eq. (8.31).

6. Once the response matrix χ is found, heat flux spectrum and total rate of energy transfer can be calculated using Eq.(8.36)

Chapter 9

Results

In this chapter we present the main results obtained with the fluctuating multipolar spectral method. First, to illustrate the method, energy transfer between a dimer of dielectric spheres is analyzed in the dipolar approxaimation. This allows analytical expressions of the energy flux spectrum and a simple tracking of the modes of the system and their contribution to energy transfer. We then analyze the same system taking into consideration full multipolar interaction and compare these results with the dipole approximation. Finally, we consider the case of a trimer of spheres. The rate of energy transfer is calculated between particles and compared to the case of a dimer. With this method it is possible to consider small separation distances, i. e. cases where the center to center separation distances is $R < 3a$.

9.1 Dipolar Interaction

Let us verify our method by comparing with exiting theories within the dipolar approximation. Then, we identify the effects due to the coupling between dipolar modes. So, defining L_{max} as the highest order multipole taken into account, indexes l and m can take values $l = 1, 2, ...L_{max}$ and once l is given $m = -l, ..., 0, ..., l$. As a first example, we consider the case of two spheres in the dipole approximation, which is achieved by taking $L_{max} = 1$ and then, $m = -1, 0, 1$. The problem of power exchange by two interacting dipoles, including radiation terms, has been studied in the single scattering approximation (107) and with coupling or full interaction(109).

Within the dipole approximation and using the spectral representation, the generalized

flux in Eq. (8.35) is reduced to three terms

$$\Phi(\omega) = \frac{2}{\pi}\mathrm{Im}[\alpha_1(\omega)]\mathrm{Im}[\alpha_2(\omega)] \times \sum_{m=-1}^{1}\left\{\left[A_{1m}^{1m}\right]^4\left[G_{1m}^{1m}(\omega)\right]^2 + 2\left[A_{1m}^{1m}\right]^3\mathrm{Re}[G_{1m}^{1m}(\omega)] + \left[A_{1m}^{1m}\right]^2\right\}, \tag{9.1}$$

where matrix elements from Eq. (**??**) are: $A_{1m}^{1m} = (-1)\frac{4\pi}{R^3}\left(\frac{1}{3}\right)$ if $m = \pm 1$ and $A_{1m}^{1m} = \frac{4\pi}{R^3}\left(\frac{2}{3}\right)$ if $m = 0$. The first two terms result from the coupling or full interaction and are multiplied by the Green function in Eq. (8.28), while the last term is given by the single scattering. In this particular case, $A_{1m}^{1m} \propto 1/R^3$, so that the last term in Eq. (9.1) falls off as $1/R^6$ while the remaining terms fall off as $1/R^9$ and $1/R^{12}$. Consequently, for large separations power exchange is dominated by its last term, which describes the interaction of the thermal fields in the single scattering approximation. Moreover, at large separations, coupled modes of the system tend to zero and Eq. (9.1) tends to that derived by Volokitin et al. (104) and Chapuis et. al. (107) taking the quasi-static limit. However, at smaller separations, coupled terms are comparable to single scattering terms, and provide additional channels through which energy can be transferred, particularly when resonant conditions are met. By keeping all terms in Eq. (9.1) we recover the formalism of interacting dipoles used for example by Manjavancas (109).

To further illustrate, we consider two systems comprised of spherical SiC particles, which support surface modes in the infrared which can be more easily excited by thermal fields near room temperatures. To explore geometrical factors besides the separation distance, we consider dimer A with particle radii $a_1 = a_2 = 5.0$ nm and dimer B with radii $a_1 = 2.5$ nm and $a_2 = 7.5$ nm. The parameters for the Drude-Lorentz dielectric function of SiC were taken from Joulain et al. (21). In Figure (9.1) we compare $\Phi(\omega)$ calculated using Eq. (9.1) and equations found in reference (107), at two different separation distances for both systems. We can see that $\Phi(\omega)$ is larger for dimer A for both separations distances by nearly half order of magnitude. This is because $\Phi(\omega)$ depends on the multiplication of the volume of the spheres(107), which is larger for dimer A. In Figure (9.1) a) and b) particle centers are separated by $R = 35$ nm. For this configuration interaction between spheres is negligible and the spectrum calculated using Eq. (9.1) and equations found in Ref. 107 match perfectly. Notice that one peak is observed, corresponding to an energy of the dipole resonant frequency of an isolated SiC sphere. From the definition of dipole polarizability, $\alpha(\omega) \propto [1/3 - u(\omega)]^{-1}$ we obtain that the resonant energy is found at 0.1154 eV.

We point out that the total number of modes that are obtained depends on the value of L_{max} and the number of particles in the system. For two particles in the dipole approxima-

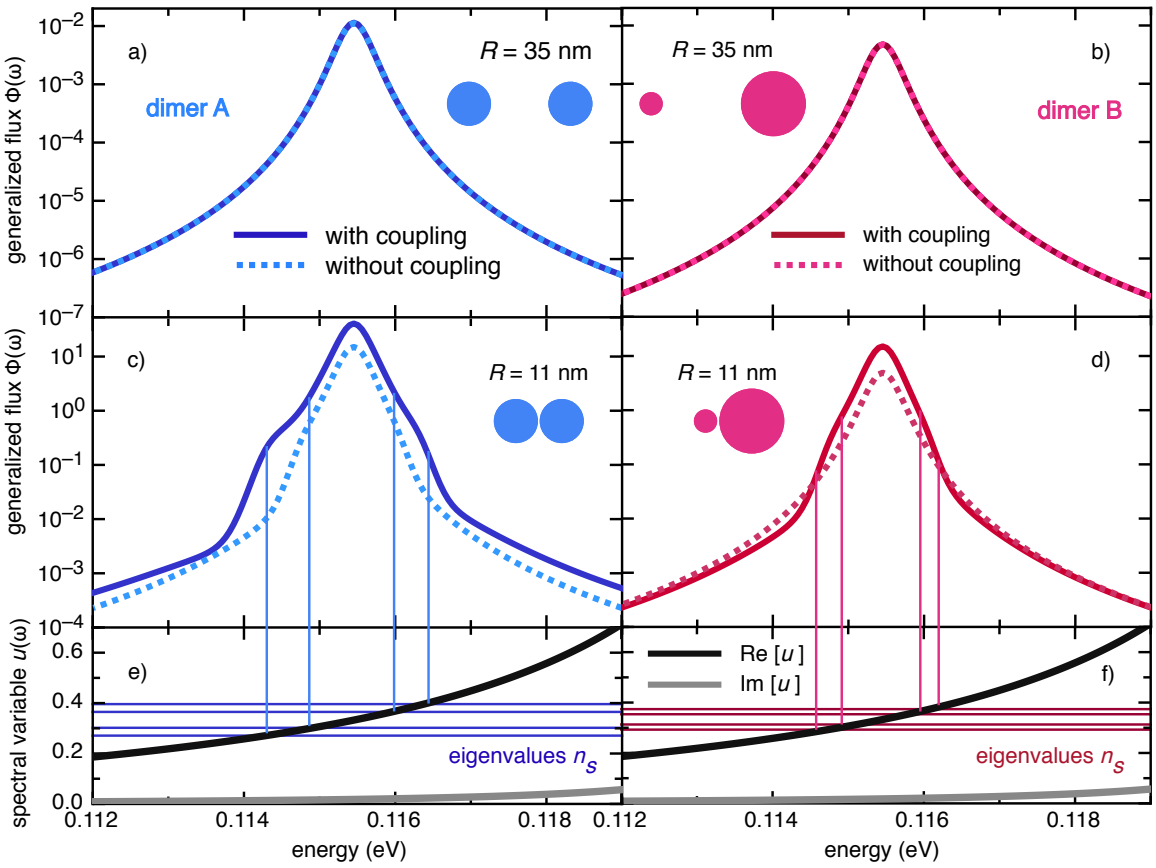

Figure 9.1: $\Phi(\omega)$ in the dipole approximation ($L_{max} = 1$) for dimer A (left) and dimer B (right) separated by a) and b) 35 nm and c) and d) 11 nm. Solid line is calculated with coupling using Eq. (9.1) and dotted using single scattering approximation (without coupling) in Ref. [104]. In e) and f) the real (black line) and imaginary (gray line) part of the spectral variable are shown and their intersection with coupled modes shown in horizontal lines.

tion $L_{max} = 1$ and $m = -1, 0, 1$, a total of 6 eigenmodes are obtained. At large separations, the interaction between particles is negligible resulting in one mode six-time degenerate. Therefore, at $R = 35$ nm the system behaves as two isolated spheres and all eigenvalues n_s tend to that of an isolated sphere, $n_0 = 1/3$. When particles are brought closer together, interaction breaks symmetry, partially removing degeneracy of the modes and shifting the resonant frequencies with respect to isolated modes. From Table 9.1 it can bee seen that at $R = 11$ nm eigenmodes corresponding to $m = 0$ are non degenerate. This is due to the breaking of symmetry in the z direction, parallel to the axis that joins the center of the spheres. Meanwhile modes with indexes $m = -1, 1$ are doubly degenerate, reflecting the symmetry that exist in the x-y directions. Furthermore, shift of the resonant frequencies is larger for dimer A than dimer B. This can be traced to the dependence of the interaction terms on the multiplication of the volume of spheres, as can be seen in Eq. (8.26), which is larger for dimer A than dimer B. A stronger interaction gives rise to a larger frequency shift of the modes. In Fig. 9.1 c) and d), $\Phi(\omega)$ is shown for $R = 11$ nm. In contrast to the case of $R = 35$ nm, two additional shoulders can be seen in the spectrum, which corresponds to an excitation of coupled modes. This is corroborated in Figure (9.1) e) and f) where the spectral variable is shown along with the eigenvalues of the coupled modes of the system, where resonant conditions are met when $\mathrm{Re}\,[u(\omega)] = n_s$. The spectrum is asymmetric since the shoulder at smaller energies are more intense than those at larger energies. The asymmetry in the spectrum can be traced to the fact that modes at lower energy correspond to smaller values of $\mathrm{Im}[u(\omega)]$, and therefore are excited more intensely.

In Figure (9.2) we show the calculated power exchange for dimer A and B varying the separation distance, using Eq. (8.36). To show how the coupled modes modify power exchange, we compare it with results within the single scattering approximation or without coupling. Power exchange was done by integrating the power spectrum from $0.1100 - 0.1200$ eV, as contributions from the rest of the range were negligible. Since power exchange depends on the polarizabilities which are proportional to the product of particle volumes, dimer A has more substantial power exchange than dimer B for all distances. It is seen that for $R > 20$ nm, interaction becomes negligible. Moreover, at these separation distances power exchange falls off as $1/R^6$. As particles are brought closer, interaction causes power exchange to deviate from that calculated in the single scattering approximation or without coupling. At $R = 11$ nm, single scattering terms account for only 25 % of the power exchange in dimer A and up to 35 % in dimer B. It can be argued that interaction between particles generates coupled modes, which are additional channels through which energy may

Dimer A: $a_1 = a_2 = 5.0$ nm		
m	Eigenvalue (n_s)	Resonant Energy (eV)
0	0.271	0.1142
0	0.396	0.1163
1,-1	0.302	0.1149
1,-1	0.365	0.1160
Dimer B: $a_1 = 2.5$ nm, $a_2 = 7.5$ nm		
m	Eigenvalue (n_s)	Resonant Energy (eV)
0	0.293	0.1147
0	0.374	0.1160
1,-1	0.313	0.1151
1,-1	0.354	0.1158

Table 9.1: Eigenvalues and resonant frequencies of the coupled modes of dimer A and B with $R = 11$ nm in the dipole approximation.

be transferred. These are the same mechanisms that bring about an enhancement of the electric field near the sphere's surface when exciting coupled modes(**?**). Almost an order of magnitude increases total power exchange, consequently, at small separation distances, it is insufficient to work in the single scattering approximation or when mode coupling is not taken into account.

Summarizing, for large separation distances the system's eigenmodes tend to those of found using single scattering (82). As separation decreases and interaction is stronger, the degeneracy of the system's modes is broken and shifted concerning isolated modes. $\Phi(\omega)$ undergoes an overall broadening with decreasing separation distance due to the shift of the resonant frequencies of the system's modes, as well as an increase in intensity. At small distances, full scattering effects mainly contribute to the $\Phi(\omega)$ and should be included in power exchange calculations. Therefore, the single scattering approximation at distances comparable to the particle radius is insufficient and coupling between modes becomes essential.

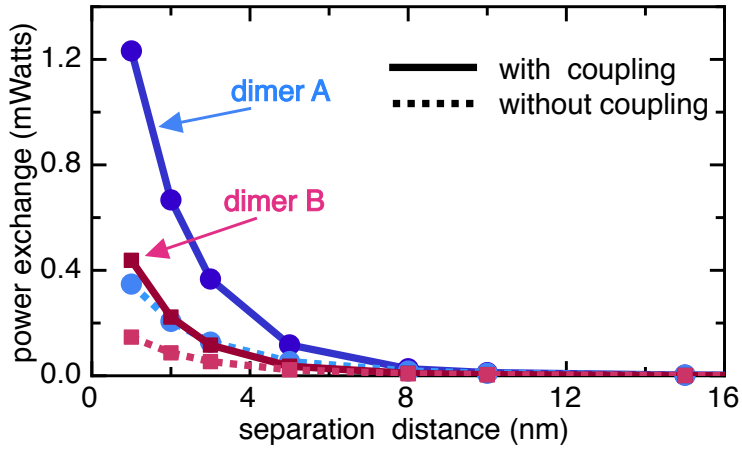

Figure 9.2: Power exchange at the dipole approximation as a function of separation, $d = R - a_1 - a_2$, for dimer A and dimer B, where SiC spheres are at 300 and 400 K.

9.2 Multipolar Interaction

It is known that at small separation distances multipolar interactions beyond the dipolar are needed to correctly describe the coupled modes of the system and consequently the power exchange between particles. (82, 111) In the following section we include higher order multipoles to calculate $\Phi(\omega)$ and show its dependence with the maximum order of multipole interactions considered. We label by L_{max} the order of the multipole approximation considered, to define convergence criteria. It is done by increasing the number of L_{max} until the largest difference between calculated $\Phi(\omega)$ spectrum is less than 1 %, which for the systems considered here it is achieved by taking $L_{max} = 50$. The convergence criteria used, as well as the number of multipolar terms required to obtain consistent solutions, depends on the specific problem and has been discussed in the literature in the context of electromagnetic scattering and near-field interaction between particles. (119) In general, the L_{max} needed for convergence increases as the separation distance decreases. (119)

In Figure (9.3) we show $\Phi(\omega)$ for two SiC particles of 5 nm radius with varying values of R. While the maximum intensity of the generalized flux is not significantly increased, an overall broadening of the spectrum, with respect to the dipole approximation, is easily appreciated. We have included the dipolar case in Figure (9.3) for comparison. From Eqs. (8.31) and (8.37) we recall that both coupled and isolated modes contribute to $\Phi(\omega)$. The overall broadening of the spectrum can be attributed to the excitation of both coupled and isolated modes. For example, because resonant frequencies of isolated modes do not depend on separation distance, we can identify the non-coupled dipole resonance, at the

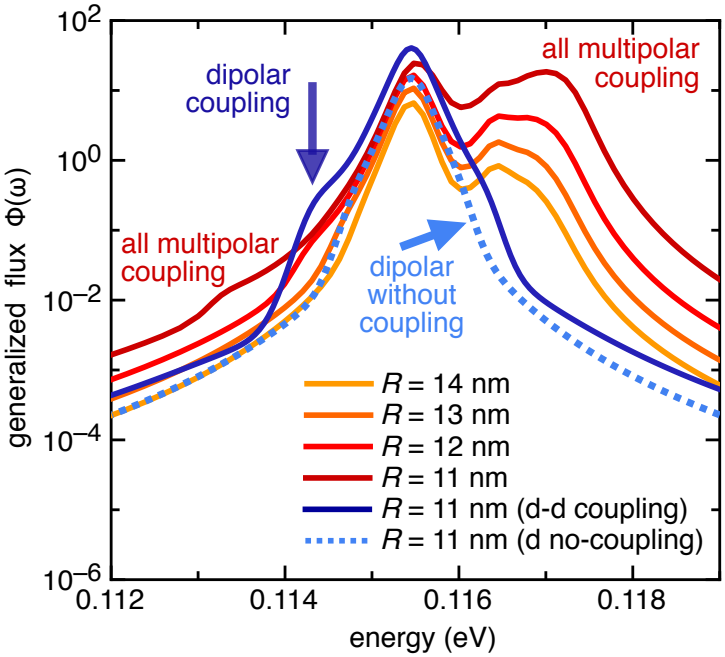

Figure 9.3: Generalized flux with all multipoles of dimer A with varying center to center separation distance for $R = 11, 12, 13$, and 14 nm. Systems with uncoupled and coupled modes corresponding to the dipolar approximation at $R = 11$ nm are also shown.

same energy of 0.1154 eV for all values of R, as well as the non-coupled quadrupolar excitation at 0.1164 eV. Peaks found at higher energies, between $0.1160 - 0.1180$ eV, are mainly due to non-coupled modes of higher order than dipole and quadrupole. In contrast, the shoulders found below 0.1154 eV, which vary with separation distance, can be associated primarily to the excitation of coupled high-multipolar modes with the dipole mode. As separation distance between NPs decreases, the resonant frequency of this mode is red-shifted to energies with smaller $\mathrm{Im}[u(\omega)]$ and therefore are excited more intensely.

In Figure (9.4) we show the total power exchange between two SiC spheres at temperatures $T_2 = 400°$ K and $T_1 = 300°$ K with radius $a_1 = a_2 = 5$ nm. The integration limits for calculation of the power exchange are taken to be $0.1000 - 0.1500$ eV. By varying the limits we verified that contributions from the rest of the spectrum are not significant for SiC spheres at the temperatures considered. Furthermore comparing Figures (9.3) and (9.2), it can be seen that inclusion of multipolar interactions provides more active modes for energy transfer and the power exchange for all separation distances compared to the dipole approximation increases. For $R > 20$ nm power exchange falls off as R^{-6}, therefore defining the region where the dipole approximation is valid. However at smaller values of R power exchange increases at a faster rate than predicted by the dipole approximation.

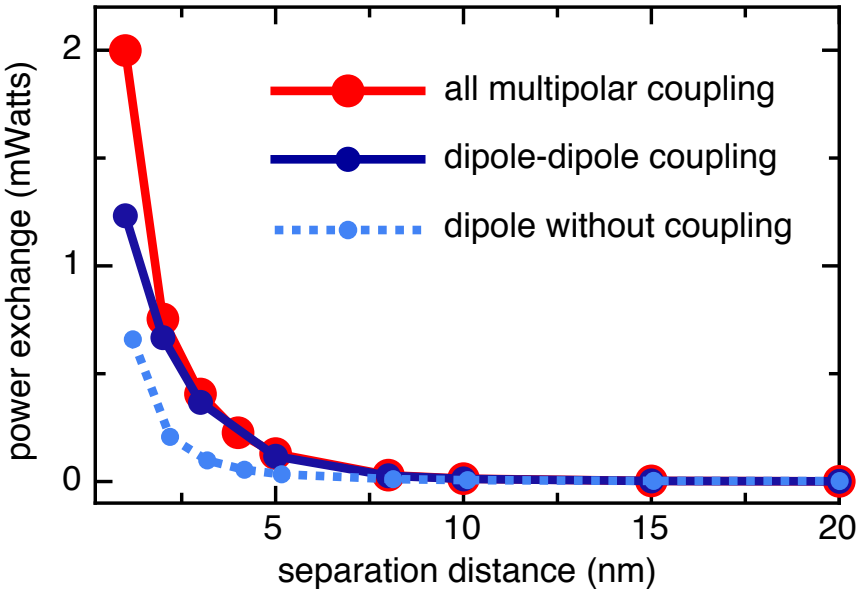

Figure 9.4: Total power exchange for temperatures $T_1 = 400$ and $T_2 = 300$ at the non-interacting dipole, interacting dipole and interacting multipole ($L_{max} = 50$) plotted against separation distance $d = R - 2a$ for dimer A.

Power exchange due to the inclusion of multipoles increases by nearly a factor of three compared to the dipole single scattering approximation and nearly doubles compared to the interacting dipole approximation as can be seen in Figure (9.4). As expected, inclusion of coupling increases power exchange when compared to the single scattering approximation. As a final remark, power exchange between particles depends on the multiplication of the volume of the spheres. Therefore, dimer A shows largest power exchange and this decreases as the system becomes more asymmetric, in other words, when the ratio between spheres a_1/a_2 is different from unity. Furthermore, contribution to power exchange due to coupled modes increases as the system becomes more symmetric, i.e., a_1/a_2 tends to one. For example, in dimer A with $R \approx 11$ nm, coupled modes contribute up to nearly 25% of total power exchange between particles.

9.3 Effects of many-body multipolar interactions

In this section we use a system comprised of three spherical particles, aligned on a same axis, to illustrate collective effects. Emergent phenomena due to many particle interactions, have been studied largely using the coupled dipole approximation (120). As we have discussed, this is valid for cases where the ratio of radius to center-center separation distance is larger

than $R/a \approx 3$. However, at smaller ratios, i.e. smaller separation distances for a fixed radius, the dipole approximation is no longer valid and multipolar interactions become important. The multipolar spectral representation presented in this work, allows us to investigate the many-body interactions in closely spaced particles.

We compare the power exchange between two 5 nm SiC particles separated by a center-center distance R (dimer) and two 5 nm SiC particles separated by the same distance R with a third particle of the same radius whose center lies at the midpoint (trimer). The condition $R \geq 4a$ must hold to avoid overlapping of particles. In Figure (9.5) we show the flux spectrum between particle 1 and 2 with a separation distance of 22 nm for the dimer and trimer. It can be seen that the flux spectrum of the dimer is dominated by the isolated resonances of the dipolar mode, with a small contribution from the quadrupolar one. In this system coupled modes have contribute little to the flux spectrum compared to the isolated modes. In contrast to dimer, the flux spectrum of the trimer has a contribution from the isolated dipole, quadrupole and octupole modes. Furthermore, multipolar coupled modes have a large contribution, with peak intensities of coupled modes comparable to the peak intensities of the dipolar isolated mode. It is seen that there is an overall broadening of the spectrum, in particular for energies smaller than the dipole resonance. This can be explained by noticing that at this energy range, the imaginary part of the spectral variable decreases with decreasing energy and therefore modes at this smaller energies couple stronger to the fluctuating thermal fields of the other particles. Consequently, for this separation distance, coupled modes that are shifted to lower energies with respect to their corresponding isolated mode will contribute larger to the spectrum than those that are shifted towards higher energies.

For the following analysis it is convenient to define a normalized heat flux as

$$\varphi(\omega) = \Phi_{1\to2}^{(\text{trimer})} / \Phi_{1\to2}^{(\text{dimer})} \tag{9.2}$$

where $\Phi_{1\to2}^{(\text{dimer})}$ is the spectral heat flux from particle 1 to particle 2 in the dimer and $\Phi_{1\to2}^{(\text{trimer})}$ is the heat flux from particle 1 to particle 2 in the trimer. An equivalent quantity for the total power exchange can be defined as $P = P_{1\to2}^{(\text{trimer})} / P_{1\to2}^{(\text{dimer})}$. In Figure (9.6) we show the enhancement of the flux spectrum and power exchange with varying separation distance when particles 1 and 2 are at 400 and 300 K respectively. Since we calculate energy transfer between particles 1 and 2, only the temperatures of these particles enter into the power exchange equation. For simplicity we consider the middle particle to be at temperature $T_3 = 0$, so that it does not generate additional fields. Inclusion of multipole interaction allows the consideration of small separation distances where the dipole approximation is no

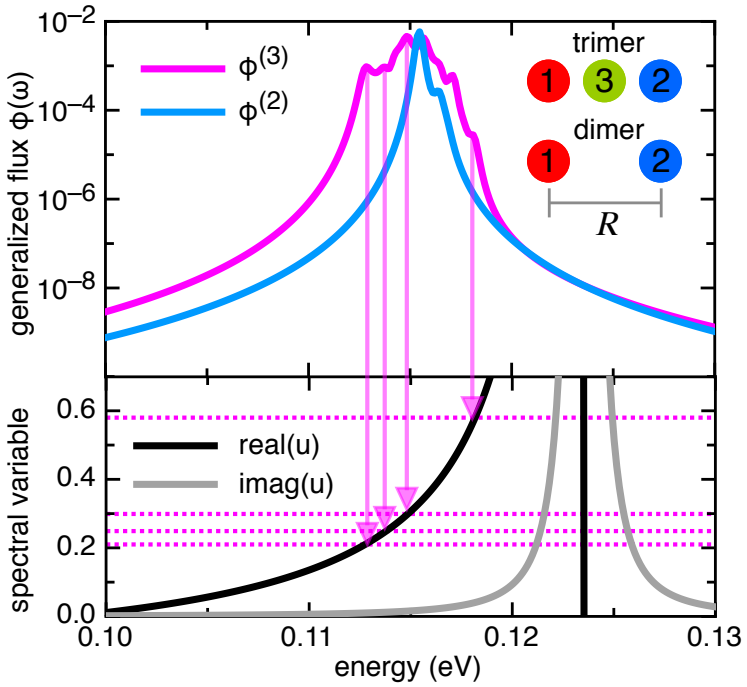

Figure 9.5: $\Phi_{1\to 2}$ for the dimer and trimer with a center-center separation $R = 22$ nm. The real (black line) and imaginary (gray line) part of the spectral variable are shown (bottom). Intersection with eigenvalues shown in horizontal lines corresponds to the resonant coupled modes while vertical arrows show the isolated resonances.

longer accurate.

In Figure (9.6) we show power enhancement versus the ratio of separation distance to sphere radius R/a. It can be seen that a power enhancement (P) curve is obtained similar to those found in references (120) where a coupled dipole approximation is used. Results show that an enhancement of power exchange of up to an order of magnitude was found due to interactions with a third body. However, this enhancement falls off quickly as separation distance is increased. We point out that this tendency is not monotonic, but rather has a maximum for a given separation distance. To help understand this behavior and the role of coupled modes in the enhancement of power exchange, in Figure (9.6) we show the normalized and generalized heat flux spectrum calculated at and near the maximum of enhancement. We point out that the generalized flux in Figure (9.6) (c) is in a log scale, and that largest contribution to total energy transfer comes from the region localized near the non-coupled dipoles resonance, at the same energy of 0.1154 eV. For configurations with ratios $R/a > 6.5$ there is a tendency of increasing enhancement with decreasing separations distance. We notice that normalized flux for the $R/a = 7.0$ and $R/a = 6.5$ configurations are very similar for energies near the non-coupled dipole resonance. This is en part due to the fact that resonant energies of coupled modes are distributed near 0.1154 for both configurations. However, coupled modes in the $R/a = 6.5$ configuration can be excited more strongly by the thermal fields than in the $R/a = 7.0$ due to the smaller separation distance. For configurations with ratios $R/a < 6.5$ a tendency of decreasing enhancement with decreasing separation distance is observed. In particular, for a ratio of $R/a = 6.0$, an increase of the normalized flux can be seen at nearly all energies, except near the non-coupled dipole resonance. This is because interaction between particles shifts the resonant energies of the coupled modes away from non-coupled resonant energy. Consequently, even though enhancement at the non-coupled resonance is only slightly less than the enhancement at this same energy for $R/a = 6.5$, the overall effect is a decrease in total energy transfer. Therefore, for smaller ratios than $R/a = 6.5$, although the normalized flux continues to increase with decreasing separation distance, coupled modes are not excited as strongly at 0.1154 eV, leading to a smaller enhancement of power exchange.

From these results we can see that heat flux spectrum is enhanced by more than an order of magnitude for certain energies and separation distances, leading to an enhancement of power exchange of up to an order of magnitude. It is seen that multipolar modes play an important role at separation distances comparable to the radius of the spheres, which

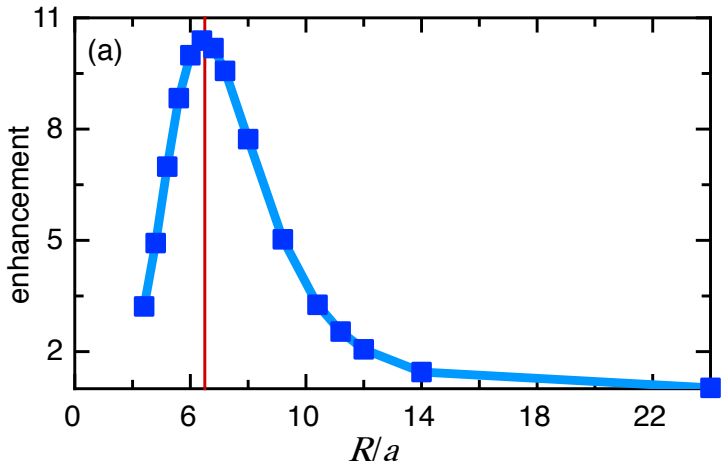

Figure 9.6: Enhancement of power exchange in the trimer system when compared to the dimer.

previously have not been considered in many body systems. Inclusion of a third sphere opens new channels of energy transfer compared to the dimer even though the third particle is taken to be at zero temperature. An overall broadening of flux spectrum is observed, as in the two particle case, however in three particle system the intensity and broadening of flux spectrum is much larger.

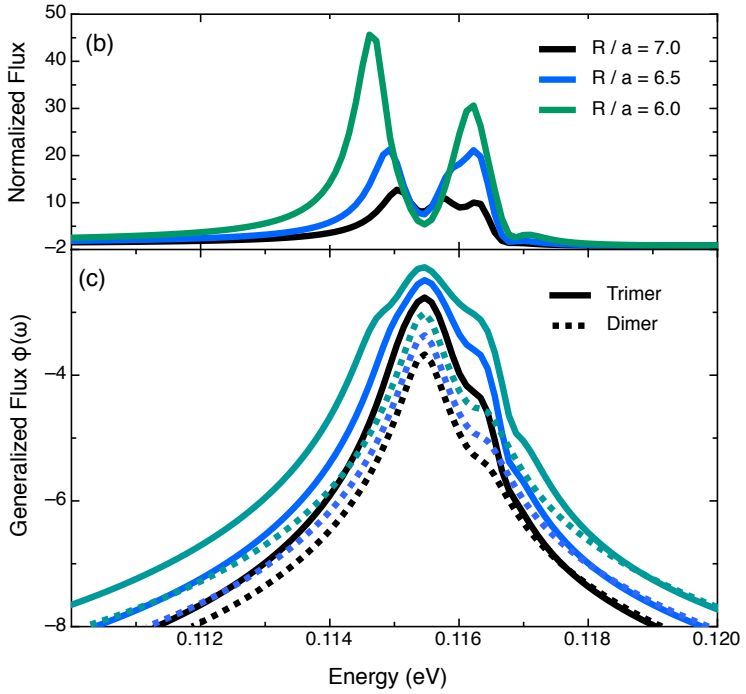

Figure 9.7: Enhancement of the flux spectrum of the trimer system compared to the dimer with varying separation distance.

Chapter 10

Conclusions k

A study of the role of coupled surface modes in radiative energy transfer between small spherical nanoparticles mediated by multipolar interactions was presented. The importance of including multipolar distributions as well as full interaction and coupling between particles at nanometer separation distances was shown, and an identification of the regime where the single scattering approximation is valid was obtained. An analysis was presented of how multipolar interaction affects coupled surface modes which are additional channels through which energy is transferred and which is commonly neglected or calculated at the dipole level increasing energy transfer nearly an order of magnitude. Furthermore, it is shown that excitation of multipole coupled modes brings about an overall broadening of the flux spectrum leading to a substantial increase of power exchange compared to the single scattering or dipole approximations. The increase of energy transfer brought about by the excitation of multipolar coupled modes at nanometric separation distances may help account for deviations observed in experiments when compared to current models. This was achieved by developing a new method that combines the fluctuation-dissipation theorem and a multipolar spectral representation which separates dielectric and geometric parameters of the system, allowing unambiguous identification of coupled surface modes. With this formalism, we have also studied the radiative energy transfer in a system of three particles with varying separation distance. The inclusion of multipole interactions was used to study many body effects at small separation distances where the dipole approximation has been typically used but is insufficient to describe full interactions. Optimal parameters for the enhancement of energy transfer, of up to an order of magnitude due to a third particle were found which were found to depend on the tendencies of the coupled modes of the system. In the trimer system, heat flux spectrum is enhanced by up to 2 orders of magnitude for specific energies and separation distances leading to an enhancement of power exchange of up to an order of magnitude relative to the dimer.

In this thesis we have studied the multipolar nearf-field radiative heat transfer between dielectric NPs, however much room is left for future work. For example, the radiative heat tranfer between multilayer planar materials has been recently studied by Perez-Rodriguez et. al. (121). In the work by Perez-Rodriguez, heat transfer is controlled by modifying the dielectric properties one of the layered media by adding nanocavities or NPs. The incrustation and porosity are added in a random manner and described by effective medium theory and shift the polariton resonance of the material. The question remains of how energy transfer would be effected by adding closely spaced and/or ordered NPs or nanocavities. Furthermore, by using the method presented in this thesis, large filling factors and small separation distances between particles could be studied.

Along a similar line, much recent research has been focused on the optical properties of plasmomic hexagonal lattices and hexagonal ribbons (122). Many of the electronic properties found in 2-d systems such as graphene have found an analogy plasmonic arrays. For example, the plasmonic band structure found in 2-d hexagonal systems composed of metallic NPs, posses Dirac cones in the K points of the Brilluoin zone. Likewise, the band structure of plasmonic honeycomb ribbons, posses edge states which give rise to flat edge bands, similar to those found in graphene ribbons. However, the modeling of these systems has been carried out mainly in the dipole approximation and remains valid for separation distnaces comparable to the particle radius. The question remains of how multipolar interaction could effect the plasmonic bands and other optical properties of the system.

Appendix A

Dielectric Function for metallic nanoparticles

In chapter 2 we discussed a model to obtain the dielectric function of bulk metals which describes the response of nearly free electrons to an external EM field. This model accounts for what is known as intraband transitions. Intraband contributions come from electron transitions at the Fermi level in incompletely filled bands, or when a filled band overlaps in energy with an empty band. These transitions also provide an absorption mechanism but at lower energies. Electrons at the Fermi level in metals are excited by photons of very small energies, such that, they are essentially "free" electrons. However, when modeling the dielectric function of metallic nanoparticles, modifications must me made to describe size effects and possible intraband transitions. Interband contributions are due to electron transitions from occupied to empty bulk bands separated by an energy gap. The electrons are bound by a restoring force given by the energy difference between ground and excited electronic states in metals, usually at the ultra violet (UV) region. These effects can usually be explained satisfactorily with classical EM theory and a size-adapted bulk dielectric constants. Experimentally measured dielectric functions $\epsilon_{\text{exp}}(\omega)$, have contributions from interband (inter) and intraband (intra) electron transitions, which we assume are additive so that the total dielectric function is written as

$$\epsilon(\omega) = \epsilon_{\text{inter}}(\omega) + \epsilon_{\text{intra}}(\omega) \tag{A.1}$$

Intraband transitions are described by the drude model

$$\epsilon_{\text{intra}}(\omega) = 1 - \frac{\omega_p^2}{\omega(\omega + i\gamma\omega)} \tag{A.2}$$

where ω_p is the plasma frequency and $1/\tau$ the damping constant which is related to the dispersion of electrons. Since are interested in small nanoparticles we have to consider that electrons can be also dispersed by the NP surface, because the free electron's mean free path is now comparable or larger than the dimension of the particle. Therefore, it is

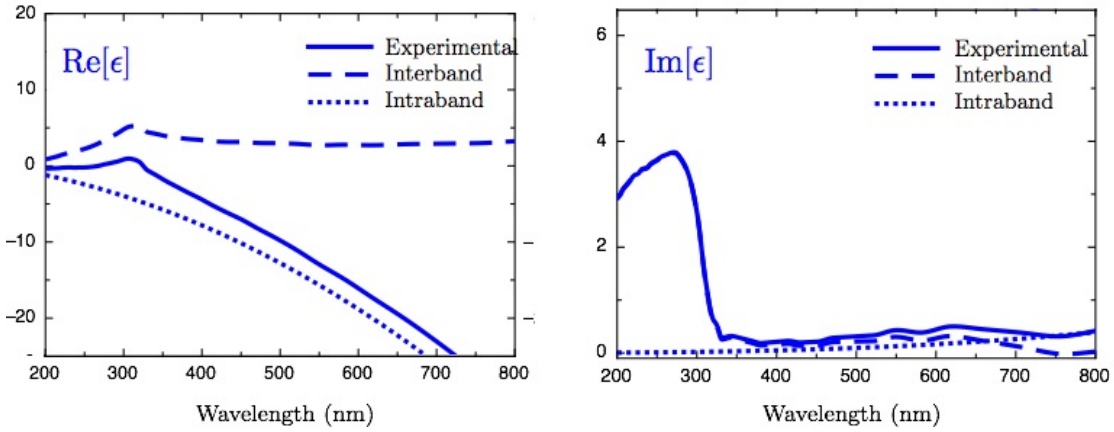

Figure A.1: Absorption spectrum of two Ag nanoparticles of a = 12 nm for different gap separation, where center to center separation is given as $R = 2a + d$. The case of an isolated particle is also shown (top). Electric field enhancement of the isolated particle and the interacting particles separated by 1 nm (bottom).

necessary to include an extra damping term $\tau(a)$ to ϵ_{exp} , due to the surface scattering of the "free" electrons. The surface dispersion not only depends on the particle size, but also on its shape.

To include surface dispersion we need modify the intraband contributions by changing the damping term. From Eq.(A.2), we obtain the input of the bound charges by subtracting the free electron contribution from the bulk dielectric function. The free electron contributions are calculated with Drude and using the theoretical values of ω_p. Now, we include the surface damping by adding the extra damping term $\tau(a)$ to the Drude model. Finally, we obtain a dielectric function, which also depends on he NP size, and includes the contributions of (i) the free electrons, (ii) surface damping, and (iii) interband transitions or bound electrons, given by

$$\begin{aligned} \epsilon(\omega, a) &= \epsilon_{\text{inter}}(\omega) + \epsilon_{\text{intra}}(\omega) \\ &= [\epsilon_{\text{exp}}(\omega) - \epsilon_{\text{intra}}(\omega)] + \left[1 - \frac{\omega_p^2}{\omega(\omega + i\gamma\omega)}\right] \end{aligned} \tag{A.3}$$

dispersion of a sphere of radius a given by $1/\tau(a) = v_f/a$, where v_f is the fermi velocity of the free electrons. The smaller the particle, the more important is the surface dispersion effect.

Appendix B

Fluctuation-Dissipation Theorem

Charge carriers within a body at temperature $T > 0$, undergo random thermal movement, which results in fluctuating charge distributions and current densities. The statistical description of the fluctuating sources is obtained by means of the fluctuation-dissipation theorem (FDT), which provides a general relationship between the dissipation properties of a system and its thermal fluctuations. Therefor, the statistical behavior of thermal fluctuations can be described in terms of the system's dissipative properties. The theorem is based on work done by Nyquist (123), who studied voltage fluctuations through a resistance. The generalized form of the theorem was derived by Callen and Welton using quantum theory (124). In the context of fluctuational electrodynamics, the FDT is usually derived in its quantum form (114, 124) and then applied in macroscopic electromagnetic theory, converting the fluctuational electrodynamics into a semiclassical theory (125). Since our system of polarizable particles is macroscopic, in the FDT is also developed in a classical way, however to take into account the quantization of electromagnetic modes, necessary for the correct description of thermal radiation, a quantum term is introduced at end of the derivation.

Assume that a system of N particles is in thermodynamic equilibrium at a temperature T and can be described using a canonical assembly. The state of the system is determined by its generalized coordinates $s = [\vec{q}_1 ... \vec{q}_N; \vec{p}_1, ... \vec{p}_N]$. Taking $x = x(s(t))$ as a dynamical variable of the system [1] whose expectation value can be calculated as

$$\langle x(t) \rangle = \frac{\int ds \rho(s) x(s,t)}{\int ds \rho(s)}, \tag{B.1}$$

where $\rho(s) = e^{-H/k_B T}$, H the Hamiltonian of the system. In stationary systems, such as systems in equilibrium, the expected value is independent of time so that $\langle x(t) \rangle = \langle x \rangle$.

[1] Variable x is dependent on time through the generalized coordinates of the system

$$x(s(t)) = x(\vec{q}^N(t), \vec{p}^N(t)).$$

It is considered that the system is subject to a perturbation force dependent on time $f(t)$ and that it is coupled to the amount $x(s)$, so that it generates a perturbative term in the Hamiltonian of the system given by

$$H' = -x(s)f(t). \tag{B.2}$$

For example, $f(t)$ can be an external electric field $\vec{E}_{ext}(t)$ and $x(s)$ the electric dipole moment that the field induces in the body, so that the interaction potential is given by $-\vec{p}\cdot\vec{E}_{ext}(t)$. Denoting the fluctuations of x as

$$X(t) = \langle x(t)\rangle - \langle x\rangle\,, \tag{B.3}$$

where $\langle x\rangle$ is the expectation value in thermodynamic equilibrium. Eq. (B.3) describes deviations from the expected value.

For a system in equilibrium the average of the fluctuations is zero $\langle X(t)\rangle = 0$, however for a system subject to an external force, the generalized susceptibility is defined $\hat{\alpha}$ as an operator that relates the perturbative force $f(t)$ and the average value $\langle X(t)\rangle$

$$\langle X(t)\rangle = \hat{\alpha}f(t) = \int_{-\infty}^{t} \tilde{\alpha}(t-t')f(t')dt', \tag{B.4}$$

where $\tilde{\alpha}(t-t')$ is a function of time that depends on the properties of the system. It has been assumed that the system is stationary i.e. is independent of the temporary origin so that $\alpha(t,t') = \tilde{\alpha}(t-t')$ is satisfied. The response of the system to the disturbance must be causal so that $\tilde{\alpha}(t-t') = 0$ if $t > t'$.

The FDT seeks to obtain an expression of the generalized susceptibility in terms of the statistical properties of the system. To simplify the deduction and analyze the physical implications of the theorem, a specific form of the perturbative force is considered, however, the result obtained is equal to the general case. A more detailed and general derivation can be found, for example, in works by Kubo (126), Landau (114). Considering a system where the perturbative force is applied from an infinite time in the past and is " turned off " at time $t = 0$. So that

$$f(t) = f_0 \text{ si } t < 0,$$

$$f(t) = 0 \text{ si } t > 0.$$

Eq. (**??**) can be reduced to

$$\langle X(t)\rangle = f_0 \int_{t}^{\infty} \tilde{\alpha}(\tau)d\tau, \tag{B.5}$$

where $\tau = t - t'$. Assuming that the generalized susceptibility and its derivative tend to zero for times $t \to \infty$, the generalized susceptibility can be cleared to obtain

$$\tilde{\alpha}(t) = \frac{\Theta(t)}{f_0} \frac{d}{dt} \langle X(t) \rangle \,, \tag{B.6}$$

where $\Theta(t)$ is the Heavside function, which guarantees causality ($\tilde{\alpha}(t - t' = 0)$ for $t' > t$). The expected value of the fluctuations $\langle X(t) \rangle$ can be related to the correlation function of x using the Eq.(B.1) and expanding the distribution function ρ. At time $t = 0$ the distribution function is given by

$$\rho(s) \propto e^{-(H_0 + H')/k_B T} = \rho_0 e^{-H'/k_B T} = \rho_0 \left[1 - \frac{1}{k_B T} H' + ... \right] , \tag{B.7}$$

where $\rho_0 = e^{-H/k_B T}$. Inserting Eq.(B.7) in Eq.(B.1) and expanding to first order in the perturbation H'

$$\langle x(t) \rangle = \langle x \rangle - \frac{1}{k_B T} \left[\langle H'(s) x(s,t) \rangle - \langle H'(s) \rangle \langle x(s,t) \rangle \right] , \tag{B.8}$$

donde al tomar los promedios estadísticos $\langle ... \rangle$ se utiliza la función de distribución sin la perturbación ρ_0. Dado que al tiempo $t = 0$ el término $H' = -x(s) f_0$ la ecuación anterior se reduce a

$$\begin{aligned} X(t) = \langle x(t) \rangle - \langle x \rangle &= -\frac{1}{k_B T} \left[\langle H'(s) x(s,t) \rangle - \langle H'(s) \rangle \langle x(s,t) \rangle \right] \\ &= -\frac{f_0}{k_B T} \left[\langle x \rangle \langle x \rangle - \langle x(s,0) x(s,t) \rangle \right] \\ &= -\frac{f_0}{k_B T} \langle \left[x(s,0) - \langle x \rangle \right] \left[x(s,t) - \langle x \rangle \right] \rangle \\ &= -\frac{f_0}{k_B T} \left[\langle X(0) X(t) \rangle \right] , \end{aligned} \tag{B.9}$$

where $X(t) = \langle x(t) \rangle - \langle x \rangle$ are fluctuation in time t and is the temporal correlation function

$$\langle X(0) X(t) \rangle = \langle x(s,0) \rangle \langle x(s,t) \rangle - \langle x(s,0) x(s,t) \rangle \,.$$

Inserting Eq.(B.9) in (B.6)

$$\tilde{\alpha}(t) = -\frac{\Theta(t)}{k_B T} \frac{d}{dt} \left[\langle X(0) X(t) \rangle \right] , \tag{B.10}$$

the classic time-dependent FDT (127). The theorem shows that it is possible to write the response of a system (susceptibility) in terms of the temporal correlation function of system fluctuations.

The FDT can be passed to the frequency space using the Fourier transform of the fluctuations

$$X(\omega) = \frac{1}{2\pi} \int X(t) e^{i\omega t} dt, \qquad X(t) = \int X(\omega) e^{-i\omega t} d\omega.$$

Consider the correlation function $\langle X(\omega)X^*(\omega')\rangle$. Taking its Fourier transform

$$\begin{aligned}\langle X(\omega)X^*(\omega')\rangle &= \frac{1}{4\pi^2}\int\int_{-\infty}^{\infty}\langle X(\tau)X(\tau')\rangle\, e^{i(\tau\omega'-\tau'\omega)}d\tau d\tau' \\ &= \frac{1}{4\pi^2}\int\int_{-\infty}^{\infty}\langle X(\tau)X(t+\tau)\rangle\, e^{i(\omega-\omega')\tau}e^{i\omega t}d\tau dt,\end{aligned} \tag{B.11}$$

where the asterisk indicates the complex conjugate and in the second equality the change of variable $tau^{prime} = t + tau$ was used. The Wiener-Khintchine theorem states that the Fourier components of the autocorrelation function with different frequencies are annulled (115, 116). So that

$$\langle X(\omega)X^*(\omega')\rangle = \delta(\omega-\omega')\frac{1}{2\pi}\int_{-\infty}^{\infty}\langle X(\tau)X(t+\tau)\rangle\, e^{i(\omega-\omega')\tau}e^{i\omega t}dt. \tag{B.12}$$

The term in the integral is known as the spectral density. Using the Wiener-Khintchine theorem and performing the Fourier transform of each term of Eq. (B.9) and using Eq. (B.12)

$$\left[\alpha(\omega)-\alpha^*(\omega)\right]\delta(\omega-\omega') = \frac{4\pi i\omega}{k_BT}\left\langle X(\omega)X^*(\omega')\right\rangle, \tag{B.13}$$

which is the classic TFD in the Fourier space [1] .

The principle of equipartition of energy identifies the factor k_BT with the average energy per degree of freedom of the system. This term results from the assumption that the energy distribution of the system is continuous. However, according to quantum mechanics the energy levels of the system and, therefore, the transitions between the states of the system will be quantized. The system absorbs energy $\Delta E = E_n - E_m = \hbar\omega_{nm}$, where E_n, E_m are system energy levels. As a consequence, the average energy k_BT must be replaced by

$$k_BT \to \frac{\hbar\omega}{e^{\hbar\omega/k_BT}-1} + \frac{\hbar\omega}{2}, \tag{B.14}$$

which corresponds to the average energy of a quantum harmonic oscillator. In the $k_BT \gg \hbar\omega$ limit, the classic term k_BT is retrieved. The quantum version of the TFD remains

$$\langle X(\omega)X^*(\omega')\rangle = \frac{4\pi}{i\omega 2}\left(\frac{\hbar\omega}{e^{\hbar\omega/k_BT}-1}+\frac{\hbar\omega}{2}\right)\left[\alpha(\omega)-\alpha^*(\omega)\right]\delta(\omega-\omega'). \tag{B.15}$$

Defining the quantity

$$\Theta(\omega,T) = \frac{\hbar\omega}{e^{\hbar\omega/k_BT}-1}+\frac{\hbar\omega}{2},$$

Eq. (B.15) becomes

$$\langle X(\omega)X^*(\omega')\rangle = \frac{4\pi}{\omega}\mathrm{Im}\left[\alpha(\omega)\right]\Theta(\omega,T)\delta(\omega-\omega'). \tag{B.16}$$

[1] The following Fourier transform of the Heavside function is used $\Theta(\omega) = \frac{1}{2}\delta(\omega) - \frac{1}{2\pi}\frac{1}{i\omega}$.

Appendix C

Solutions to $(-a\mathbf{I} + \mathbf{H})\vec{x} = \vec{b}$

In this work we are interested in solving equations of the form

$$(-u\mathbf{I} + \mathbf{H}) \cdot \vec{x} = \vec{b} \tag{C.1}$$

where $\mathbf{H}$ is an $N \times N$ hermitian matrix, $\mathbf{I}$ the $N \times N$ identity matrix and u a scalar. In this appendix we discuss a method to solve this type of linear system, which consist of writing the solutions $\vec{x}$ in terms of the eigenvalues and eigenvectors of matrix $\mathbf{H}$.

Assuming that $\mathbf{H}$ is a hermitian matrix with linearly independent eigenvectors, it can be factorized as

$$\mathbf{U}^\dagger \mathbf{H} \mathbf{U} = \mathbf{n} \tag{C.2}$$

where $\mathbf{U}$ is a unitary matrix with the property that $\mathbf{U}\mathbf{U}^\dagger = \mathbf{I}$, and $\mathbf{n}$ is a diagonal matrix

$$\mathbf{n} = \begin{pmatrix} n_1 & 0 & \dots & 0 \\ 0 & n_2 & \dots & 0 \\ \vdots & \vdots & \ddots & \vdots \\ 0 & 0 & \dots & n_N \end{pmatrix} \tag{C.3}$$

whose elements n_i are eigenvalues of $\mathbf{H}$. Inserting this in Eq. (C.1) we have

$$\begin{aligned} -u\mathbf{I} + \mathbf{H} &= -u\mathbf{I} + \mathbf{U}\mathbf{n}\mathbf{U}^\dagger \\ &= \mathbf{U}(-u\mathbf{I})\mathbf{U}^\dagger + \mathbf{U}\mathbf{n}\mathbf{U}^\dagger \\ &= \mathbf{U}\left(-u\mathbf{I} + \mathbf{n}\right)\mathbf{U}^\dagger \\ &= \mathbf{U}\mathbf{Y}\mathbf{U}^\dagger, \end{aligned} \tag{C.4}$$

where $\mathbf{Y} = -u\mathbf{I} + \mathbf{n}$. We are interested in the inverse matrix, which we label as $\mathbf{G}$, written as

$$\begin{aligned} \mathbf{G} = (-u\mathbf{I} + \mathbf{H})^{-1} &= \left(\mathbf{U}\mathbf{Y}\mathbf{U}^\dagger\right)^{-1} \\ &= \mathbf{U}^\dagger \mathbf{Y}^{-1} \mathbf{U} \end{aligned} \tag{C.5}$$

where we used the property $\mathbf{U}^\dagger = \mathbf{U}^{-1}$. The components of this matrix are

$$\begin{aligned}\mathbf{G}_{ij} &= \sum_{\alpha\beta} \mathbf{U}^\dagger_{i\alpha} {\mathbf{Y}_{\alpha\beta}}^{-1} \mathbf{U}_{\beta j} \\ &= \sum_{\alpha\beta} \mathbf{U}^\dagger_{i\alpha} {\mathbf{Y}_{\alpha\beta}}^{-1} \mathbf{U}_{\beta j} \\ &= \sum_{\alpha\beta} \mathbf{U}^\dagger_{i\alpha} (-u+n_\beta)^{-1} \delta_{\alpha\beta} \mathbf{U}_{\beta j} \\ &= -\sum_{\alpha} \frac{\mathbf{U}^\dagger_{i\alpha}\mathbf{U}_{\alpha j}}{(u-n_\alpha)}.\end{aligned} \tag{C.6}$$

Solutions can then be found in terms of the eigenvalues and eigenvector of $\mathbf{H}$

$$\vec{x} = \mathbf{G}\cdot\vec{b} = (-u\mathbf{I}+\mathbf{H})^{-1}\cdot\vec{b}. \tag{C.7}$$

Note that matrix $\mathbf{G} = \mathbf{G}(u)$ must be calculated for each value of u.

Bibliography

[1] David Becerril, Humberto Batiz, Giuseppe Pirruccio, and Cecilia Noguez. Efficient coupling to plasmonic multipole resonances by using a multipolar incident field. *ACS Photonics*, 5(4):1404–1411, 2018. vii, xi, 21

[2] David Becerril and Cecilia Noguez. Near-field energy transfer between nanoparticles modulated by coupled multipolar modes. *Phys. Rev. B*, 99:045418, Jan 2019. viii, xii

[3] O. Hess, J. B. Pendry, S. A. Maier, R. F. Oulton, J. M. Hamm, and K. L. Tsakmakidis. Active nanoplasmonic metamaterials. *Nature Materials*, 11, 06 2012. 1

[4] Costas M. Soukoulis and Martin Wegener. Past achievements and future challenges in the development of three-dimensional photonic metamaterials. *Nature Photonics*, 5, 07 2011. 1

[5] Jiaming Hao, Jing Wang, Xianliang Liu, Willie J. Padilla, Lei Zhou, and Min Qiu. High performance optical absorber based on a plasmonic metamaterial. *Applied Physics Letters*, 96(25), 2010. 1

[6] Michael G. Nielsen, Anders Pors, Ole Albrektsen, and Sergey I. Bozhevolnyi. Efficient absorption of visible radiation by gap plasmon resonators. *Opt. Express*, 20(12):13311–13319, Jun 2012. 2

[7] Andrea Cattoni, Petru Ghenuche, Anne-Marie Haghiri-Gosnet, Dominique Decanini, Jing Chen, Jean-Luc Pelouard, and Stéphane Collin. Plasmonic nanocavities for biosensing fabricated by soft uv nanoimprint lithography. *Nano Letters*, 11(9):3557–3563, 2011. 2

[8] Zhichao Ruan, Min Yan, Curtis W. Neff, and Min Qiu. Ideal cylindrical cloak: Perfect but sensitive to tiny perturbations. *Phys. Rev. Lett.*, 99:113903, Sep 2007. 2

[9] Achim Kittel, Wolfgang Müller-Hirsch, Jürgen Parisi, Svend-Age Biehs, Daniel Reddig, and Martin Holthaus. Near-field heat transfer in a scanning thermal microscope. *Phys. Rev. Lett.*, 95:224301, Nov 2005. 2

[10] M. Laroche, R. Carminati, and J.-J. Greffet. Near-field thermophotovoltaic energy conversion. *Journal of Applied Physics*, 100(6), 2006. 2

[11] Clayton R. Otey, Wah Tung Lau, and Shanhui Fan. Thermal rectification through vacuum. *Phys. Rev. Lett.*, 104:154301, Apr 2010. 2

[12] Philippe Ben-Abdallah and Svend-Age Biehs. Near-field thermal transistor. *Phys. Rev. Lett.*, 112:044301, Jan 2014. 2

[13] Viacheslav Kubytskyi, Svend-Age Biehs, and Philippe Ben-Abdallah. Radiative bistability and thermal memory. *Phys. Rev. Lett.*, 113, Aug 2014. 2

[14] Carlos E. Román-Velázquez and Cecilia Noguez. Designing the plasmonic response of shell nanoparticles: Spectral representation. *The Journal of Chemical Physics*, 134(4), 2011. 3, 20, 28, 30, 33, 34, 38, 70

[15] Sunae So, Minkyung Kim, Dasol Lee, Duc Minh Nguyen, and Junsuk Rho. Overcoming diffraction limit: From microscopy to nanoscopy. *Applied Spectroscopy Reviews*, 53(2-4):290–312, 2018. 5

[16] Matthew Pelton and Garnett W Bryant. *Introduction to metal-nanoparticle plasmonics*. A Wiley-Science Wise Co-Publication. Wiley, Hoboken, NJ, 2013. 5, 9

[17] David Tanner. *Optical effects in solids*. 1996. 6

[18] J.D. Jackson. *Classical electrodynamics*. Wiley, 1975. 6, 8, 19, 22, 37, 38, 78, 81

[19] S. A. Maier. *Plasmonics: Fundamentals and Applications*. Springer US, 2007. 6, 14

[20] M. A. Ordal, L. L. Long, R. J. Bell, S. E. Bell, R. R. Bell, R. W. Alexander, and C. A. Ward. Optical properties of the metals al, co, cu, au, fe, pb, ni, pd, pt, ag, ti, and w in the infrared and far infrared. *Appl. Opt.*, 22(7):1099–1119, Apr 1983. 6

[21] Karl Joulain, Jean-Philippe Mulet, François Marquier, Rémi Carminati, and Jean-Jacques Greffet. Surface electromagnetic waves thermally excited: Radiative heat transfer, coherence properties and casimir forces revisited in the near field. *Surface Science Reports*, 57(3):59–112, 2005. 6, 11, 14, 62, 68, 69, 70, 88

[22] Gustav Mie. Beiträge zur optik trüber medien, speziell kolloidaler metallösungen. *Annalen der Physik*, 330(3):377–445. 7

[23] Shoji Asano and Giichi Yamamoto. Light scattering by a spheroidal particle. *Appl. Opt.*, 14(1):29–49, Jan 1975. 7

[24] Arthur C. Lind and J. Mayo Greenberg. Electromagnetic scattering by obliquely oriented cylinders. *Journal of Applied Physics*, 37(8):3195–3203, 1966. 7

[25] T. Wakamatsu and K. Aizawa. Penetration-depth characteristics of evanescent fields at metal attenuated total reflection. *Jap. J. Appl. Phys.*, 44(6R):4272, 2005. 10

[26] Britain Willingham and Stephan Link. Energy transport in metal nanoparticle chains via sub-radiant plasmon modes. *Opt. Express*, 19(7):6450–6461, Mar 2011. 11

[27] Stefan A. Maier, Pieter G. Kik, Harry A. Atwater, Sheffer Meltzer, Elad Harel, Bruce E. Koel, and Ari A. G. Requicha. Local detection of electromagnetic energy transport below the diffraction limit in metal nanoparticle plasmon waveguides. *Nature Materials*, 2:229, 03 2003. 11

[28] Na Liu, Mario Hentschel, Thomas Weiss, A. Paul Alivisatos, and Harald Giessen. Three-dimensional plasmon rulers. *Science*, 332(6036):1407–1410, 2011. 11

[29] H. Failache, S. Saltiel, M. Fichet, D. Bloch, and M. Ducloy. Resonant coupling in the van der waals interaction between an excited alkali atom and a dielectric surface: an experimental study via stepwise selective reflection spectroscopy. *The European Physical Journal D - Atomic, Molecular, Optical and Plasma Physics*, 23(2):237–255, May 2003. 11

[30] R. Hillenbrand, T. Taubner, and F. Keilmann. Phonon-enhanced light–matter interaction at the nanometre scale. *Nature*, 418:159, 07 2002. 11

[31] C. Kittel. *Introduction to Solid State Physics*. Wiley, 2004. 11, 13

[32] N.W. Ashcroft and N.D. Mermin. *Solid State Physics*. Cengage Learning, 2011. 11, 12, 14, 15

[33] G. Grosso and G.P. Parravicini. *Solid State Physics*. Elsevier Science, 2000. 11, 14, 15

[34] R. Fuchs. Theory of the optical properties of ionic crystal cubes. *Phys. Rev. B*, 11:1732–1740, Feb 1975. 19, 28, 33, 37, 43, 46

[35] Ronald Fuchs and K. L. Kliewer. Optical modes of vibration in an ionic crystal sphere∗. *J. Opt. Soc. Am.*, 58(3):319–330, Mar 1968. 19

[36] Craig F. Bohren and D.R. Huffman. *Absorption and scattering of light by small particles*. Wiley science paperback series. Wiley, 1983. 19, 33, 37

[37] Cecilia Noguez and Rubén G. Barrera. Disorder effects on the effective dielectric response of a linear chain of polarizable spheres. *Physica A: Statistical Mechanics and its Applications*, 211(4):399 – 410, 1994. 21, 28, 32

[38] Allen Taflove. Review of the formulation and applications of the finite-difference time-domain method for numerical modeling of electromagnetic wave interactions with arbitrary structures. *Wave Motion*, 10(6):547 – 582, 1988. Special Issue on Numerical Methods for Electromagnetic Wave Interactions. 22

[39] Bruce T. Draine and Piotr J. Flatau. Discrete-dipole approximation for scattering calculations. *J. Opt. Soc. Am. A*, 11(4):1491–1499, Apr 1994. 22

[40] Clemens Burda, Xiaobo Chen, Radha Narayanan, and Mostafa A. El-Sayed. Chemistry and properties of nanocrystals of different shapes. *Chemical Reviews*, 105(4):1025–1102, 2005. 27

[41] E Hutter and J.H. Fendler. Exploitation of localized surface plasmon resonance. *Advanced Materials*, 16(19):1685–1706, 2005. 27

[42] Nathaniel L. Rosi and Chad A. Mirkin. Nanostructures in biodiagnostics. *Chemical Reviews*, 105(4):1547–1562, 2005. 27

[43] Marie Daniel and Didier Astruc. Gold nanoparticles: Assembly, supramolecular chemistry, quantum size related properties and applications toward biology, catalysis and nanotechnology. *Chemical Reviews*, 104(1):293–346, 2004. 27

[44] A. L. González, Cecilia Noguez, G. P. Ortiz, and G. Rodríguez-Gattorno. Optical absorbance of colloidal suspensions of silver polyhedral nanoparticles. *The Journal of Physical Chemistry B*, 109(37):17512–17517, 2005. 28

[45] Ali M. Angulo, Cecilia Noguez, and George C. Schatz. Electromagnetic field enhancement for wedge-shaped metal nanostructures. *J. Phys. Chem. Lett.*, 2(16):1978–1983, 2011. 28, 30

[46] Encai Hao and George C. Schatz. Electromagnetic fields around silver nanoparticles and dimers. *The Journal of Chemical Physics*, 120(1):357–366, 2004. 28, 30

[47] Cecilia Noguez. Surface plasmons on metal nanoparticles: The influence of shape and physical environment. *The Journal of Physical Chemistry C*, 111(10):3806–3819, 2007. 28, 39, 45

[48] Gilad Haran. Single-molecule raman spectroscopy: A probe of surface dynamics and plasmonic fields. *Accounts of Chemical Research*, 43(8):1135–1143, 2010. 29

[49] Marco Notarianni, Kristy Vernon, Alison Chou, Muhsen Aljada, Jinzhang Liu, and Nunzio Motta. Plasmonic effect of gold nanoparticles in organic solar cells. *Solar Energy*, 106:23 – 37, 2014. Third and Fourth Generation Solar Cells. 29

[50] S Jain, D G Hirst, and J M O'Sullivan. Gold nanoparticles as novel agents for cancer therapy. *The British Journal of Radiology*, 85(1010):101–113, 2012. 29

[51] Kadir Aslan, Joseph R Lakowicz, and Chris D Geddes. Plasmon light scattering in biology and medicine: new sensing approaches, visions and perspectives. *Current Opinion in Chemical Biology*, 9(5):538 – 544, 2005. 29

[52] Konstantin Sokolov, Michele Follen, Jesse Aaron, Ina Pavlova, Anais Malpica, Reuben Lotan, and Rebecca Richards-Kortum. Real-time vital optical imaging of precancer using anti-epidermal growth factor receptor antibodies conjugated to gold nanoparticles. *Cancer Research*, 63(9):1999–2004, 2003. 29

[53] Nader Engheta and Richard W Ziolkowski. *Metamaterials: Physics and Engineering Explorations*. Wiley-IEEE Press, 2006. 29

[54] C. Della Giovampaola and N. Engheta. Digital metamaterials. *Nat. Mat.*, 13(13):1115–1121, 2014. 29

[55] J. B. Pendry. Electromagnetic materials enter the negative age. *Phys. Word*, 14(47), 2001. 29

[56] C. M. Soukoulis, S. Linden, and M. Wegener. Negative refractive index at optical wavelengths. *Science*, 315(47-49), 2007. 29

[57] V. M. Shalaev. Optical negative-index metamaterials. *Nat. Photon.*, 1(41-48), 2007. 29

[58] K. B. Alici, A. B. Turhan, C. M. Soukoulis, and E. Ozbay. Optically thin composite resonant absorber at the near-infrared band: a polarization independent and spectrally broadband configuration. *Opt. Expr.*, 19(15):14260–14267, 2011. 29

[59] D. Schurig, J. J. Mock, B. J. Justice, S. A. Cummer, J.B Pendry, A. F. Starr, and D. R. Smith. Metamaterial electromagnetic cloak at microwave frequencies. *Science*, 314:977–980, 2006. 29

[60] S. Murai, M. A. Verschuuren, G. Lozano, G. Pirruccio, S. R. K. Rodriguez, and J. G. Rivas. Hybrid plasmonic-photonic modes in diffractive arrays of nanoparticles coupled to light-emitting optical waveguides. *Opt. Expr.*, 4(4250-4262), 2013. 29

[61] G. Lozano, D. J. Louwers, S. R. K. Rodríguez, S. Murai, O. Jansen, M. A. Verschuuren, and J. Gomez Rivas. Plasmonics for solid-state lighting: enhanced excitation and directional emission of highly efficient light sources. *Light: Science and Applications*, 2(e66), 2013. 29

[62] G. Pirruccio, M. Ramezani, S. R. K. Rodriguez, and J. Gomez Rivas. Coherent control of the optical absorption in a plasmonic lattice coupled to a luminescent layer. *Phys. Rev. Lett.*, 116(103002), 2016. 29, 30

[63] A. L. González and Cecilia Noguez. Influence of morphology on the optical properties of metal nanoparticles. *J. Comput. Theor. Nanosci*, 4(2):231–238, 2007. 29

[64] Iván O. Sosa, Cecila Noguez, and Rubén G. Barrera. Optical properties of metal nanoparticles with arbitrary shapes. *J. Phys. Chem. A*, 107(26):6269–6275, 2003. 29

[65] S. Zhang, D. A. Genov, Y. Wang, M. Liu, and X. Zhang. Plasmon-exciton-polariton lasing. *Optica*, 101(047401), 2008. 30

[66] N. Liu, L. Langguth, T. Weiss, J. Kastel, M. Fleischhauer, T. Pfau, and H. Giessen. Plasmonic analogue of electromagnetically induced transparency at the drude damping limit. *Nat. Mat.*, 8(758-762), 2009. 30

[67] M. Ramezani, A. Halpin, A. I. Fernandez-Dominguez, J. Feist, S. R. K. Rodriguez, F. J. Garcia-Vidal, and Jaime Gomez Rivas. Plasmon-exciton-polariton lasing. *Optica*, 4(31-37), 2017. 30

[68] V. N. Pustovit and T. V. Shahbazyan. Plasmon-mediated superradiance near metal nanostructures. *Phys. Rev. B*, 82(075429), 2010. 30

[69] D. Martin-Cano, L. Martin-Moreno, F. J. Garcia-Vidal, and E. Moreno. Resonance energy transfer and superradiance mediated by plasmonic nanowaveguides. *Nano Lett.*, 10(8)(3129–3134), 2010. 30

[70] Radoslaw Kolkowski, Lucia Petti, Massimo Rippa, Clement Lafargue, and Joseph Zyss. Octupolar plasmonic meta-molecules for nonlinear chiral watermarking at sub-wavelength scale. *ACS Photonics*, 2(7):899–906, 2015. 30

[71] Mathieu L Juan, Maurizio Righini, and Romain Quidant. Plasmon nano-optical tweezers. *Nat Photon*, 5(6):349–356, 06 2011. 30

[72] Rafael Diaz-H.R, Raul Esquivel-Sirvent, and Cecilia Noguez. Plasmonic response of nested nanoparticles with arbitrary geometry. *J. Phys. Chem. C*, 120(4):2349–2354, 2016. 30

[73] T. S. Kao, S. D. Jenkins, J. Ruostekoski, and N. I. Zheludev. Coherent control of nanoscale light localization in metamaterial: Creating and positioning isolated subwavelength energy hot spots. *Phys. Rev. Lett.*, 106:085501, Feb 2011. 30

[74] T. Das, Prasad P. Iyer, R. A. DeCrescent, and J. A. Schuller. Beam engineering for selective and enhanced coupling to multipolar resonances. *Phys. Rev. B*, 92(24110(R)), 2015. 30

[75] I. M. Vellekoop and A. P. Mosk. Focusing coherent light through opaque strongly scattering media. *Opt. Lett.*, 32(2309-2311), 2007. 30

[76] J. Yoon, K. H. Seol, S. H. Song, and R. Magnusson. Critical coupling in dissipative surface-plasmon resonators with multiple ports. *Opt. Expr.*, 18(25702-25711), 2010. 30

[77] J. W. Yoon, G. M. Koh, S. H. Song, and R. Magnusson. Measurement and modeling of a complete optical absorption and scattering by coherent surface plasmon-polariton excitation using a silver thin-film grating. *Phys. Rev. Lett.*, 109(257402), 2012. 30

[78] Eun-Ah You, Wei Zhou, Jae Yong Suh, Mark D. Huntington, and Teri W. Odom. Polarization-dependent multipolar plasmon resonances in anisotropic multiscale au particles. *ACS Nano*, 6(2):1786–1794, 2012. 30

[79] Xu Yu-lin. "electromagnetic scattering by an aggregate of spheres. *Appl. Opt.*, 34:4573–4588, 1995. 30

[80] Francisco Claro. Theory of resonant modes in particulate matter. *Phys. Rev. B*, 30:4989–4999, Nov 1984. 35, 36

[81] B. U. Felderhof, G. W. Ford, and E. G. D. Cohen. Cluster expansion for the dielectric constant of a polarizable suspension. *Journal of Statistical Physics*, 28(1):135–164, 1982. 36

[82] R. Rojas and F. Claro. Electromagnetic response of an array of particles: Normal-mode theory. *Phys. Rev. B*, 34:3730–3736, Sep 1986. 41, 83, 91, 92

[83] Cecilia Noguez. Optical properties of isolated and supported metal nanoparticles. *Opt. Mater.*, 27(7):1204 – 1211, 2005. 41

[84] Ruben Esteban, Andrei G. Borisov, Peter Nordlander, and Javier Aizpurua. Bridging quantum and classical plasmonics with a quantum-corrected model. *Nat. Comm.*, 3(825), 2012. 41

[85] P. B. Johnson and R. W. Christy. Optical constants of the noble metals. *Phys. Rev. B*, 6:4370–4379, 1972. 42

[86] Ezequiel R. Encina and Eduardo A. Coronado. Near field enhancement in ag au nanospheres heterodimers. *J. Phys. Chem. C*, 115(32):15908–15914, 2011. 42

[87] B. V. Karlekar and R. M. Desmond. *Engineering heat transfer*. West Pub. Co St. Paul, 1977. 58

[88] M. Jammer. *The conceptual development of quantum mechanics*. International series in pure and applied physics. McGraw-Hill, 1966. 58

[89] R.M. Eisberg. *Fundamentals of modern physics*. Wiley, 1961. 58, 59

[90] M. Planck. *The Theory of Heat Radiation*. Dover Books on Physics Series. Dover Publications, 1959. 61

[91] Mathieu Francoeur and M. Pinar Mengüç. Role of fluctuational electrodynamics in near-field radiative heat transfer. *Journal of Quantitative Spectroscopy and Radiative Transfer*, 109(2):280 – 293, 2008. 62

[92] G. A. Domoto, R. F. Boehm, and C. L. Tien. Experimental investigation of radiative transfer between metallic surfaces at cryogenic temperatures. *Journal of Heat Transfer*, 92(3):412–416, 08 1970. 62

[93] C. C. Williams and H. K. Wickramasinghe. Scanning thermal profiler. *Applied Physics Letters*, 49(23):1587–1589, 1986. 62

[94] Arvind Narayanaswamy, Sheng Shen, and Gang Chen. Near-field radiative heat transfer between a sphere and a substrate. *Phys. Rev. B*, 78:115303, Sep 2008. 62

[95] D. Polder and M. Van Hove. Theory of radiative heat transfer between closely spaced bodies. *Phys. Rev. B*, 4:3303–3314, Nov 1971. 62, 69

[96] C.M Hargreaves. Anomalous radiative transfer between closely-spaced bodies. *Physics Letters A*, 30(9):491 – 492, 1969. 63

[97] R. S. Ottens, V. Quetschke, Stacy Wise, A. A. Alemi, R. Lundock, G. Mueller, D. H. Reitze, D. B. Tanner, and B. F. Whiting. Near-field radiative heat transfer between macroscopic planar surfaces. *Phys. Rev. Lett.*, 107:014301, Jun 2011. 64

[98] W. Müller-Hirsch, A. Kraft, M. T. Hirsch, J. Parisi, and A. Kittel. Heat transfer in ultrahigh vacuum scanning thermal microscopy. *Journal of Vacuum Science and Technology A*, 17(4):1205–1210, 1999. 65

[99] A. Kittel, W. Muller-Hirsch, J. Parisi, S.V. Biehs, D. Reddig, and M. Holthaus. Near-field heat transfer in a scanning thermal microscope. *Phys. Rev. Lett.*, 95, 2005. 65

[100] C. Noguez, C. E. Román-Velázquez, R. Esquivel-Sirvent, and C. Villarreal. High-multipolar effects on the casimir force: The non-retarded limit. *EPL (Europhysics Letters)*, 67(2):191, 2004. 65, 70

[101] Illarion Dorofeyev. Rate of heat transfer between a probing body and a sample due to electromagnetic fluctuations. *Physics Letters A*, 372(9):1341 – 1347, 2008. 65, 69, 70, 71

[102] Sheng Shen, Arvind Narayanaswamy, and Gang Chen. Surface phonon polaritons mediated energy transfer between nanoscale gaps. *Nano Letters*, 9(8):2909–2913, 2009. 66

[103] B. Derjaguin. Untersuchungen über die reibung und adhäsion, iv. *Kolloid-Zeitschrift*, 69(2):155–164, Nov 1934. 66

[104] A. I. Volokitin and B. N. J. Persson. Radiative heat transfer between nanostructures. *Phys. Rev. B*, 63:205404, Apr 2001. 67, 88, 89

[105] Philippe Ben-Abdallah Svend-Age Biehs and Felipe S. S. Rosa. Nanoscale radiative heat transfer and its applications. *Infrared Radiation*, 2012. 69

[106] S.M. Rytov, I.U.A. Kravstov, and V.I. Tatarski. *Principles of statistical radiophysics.* Principles of Statistical Radiophysics. Springer-Verlag, 1989. 69, 73

[107] Pierre-Olivier Chapuis, Marine Laroche, Sebastian Volz, and Jean-Jacques Greffet. Radiative heat transfer between metallic nanoparticles. *Applied Physics Letters*, 92(20), 2008. 69, 70, 87, 88

[108] I. Dorofeyev. The van der waals interaction of microparticles with a substrate characterized by a nonlocal response. *Phys. Lett. A*, 363(4):251 – 256, 2007. 69

[109] Alejandro Manjavacas and F. Javier García de Abajo. Radiative heat transfer between neighboring particles. *Phys. Rev. B*, 86:075466, Aug 2012. 70, 87, 88

[110] Gilberto Domingues, Sebastian Volz, Karl Joulain, and Jean-Jacques Greffet. Heat transfer between two nanoparticles through near field interaction. *Phys. Rev. Lett.*, 94:085901, Mar 2005. 70, 71

[111] A. Pérez-Madrid, J. M. Rubí, and L. C. Lapas. Heat transfer between nanoparticles: Thermal conductance for near-field interactions. *Phys. Rev. B*, 77:155417, Apr 2008. 70, 84, 92

[112] Raphael St-Gelais, Linxiao Zhu, Shanhui Fan, and Michal Lipson. Near-field radiative heat transfer between parallel structures in the deep subwavelength regime. *Nature Nanotechnology*, 11:515, 03 2016. 73

[113] Kyeongtae Kim, Bai Song, Víctor Fernández-Hurtado, Woochul Lee, Wonho Jeong, Longji Cui, Dakotah Thompson, Johannes Feist, M. T. Homer Reid, Francisco J. García-Vidal, Juan Carlos Cuevas, Edgar Meyhofer, and Pramod Reddy. Radiative heat transfer in the extreme near field. *Nature*, 528:387, 12 2015. 73

[114] L.D. Landau and E.M. Lifshitz. *Statistical Physics.* Number v. 5. Elsevier Science, 2013. 74, 75, 76, 80, 105, 106

[115] A. Khintchine. Correlation theory of stationary stochastic processes. *Mathematische Annalen*, 109(1):604–615, 1934. 75, 108

[116] Norbert Wiener. Generalized harmonic analysis. *Acta Math.*, 55:117–258, 1930. 75, 108

[117] C Henkel. Nanoscale thermal transfer – an invitation to fluctuation electrodynamics. *Zeitschrift für Naturforschung A*, 72(2):99–108, 2018. 78

[118] L.D. LANDAU and E.M. LIFSHITZ. In *Electrodynamics of Continuous Media*, volume 8 of *Course of Theoretical Physics*. Pergamon, Amsterdam, second edition revised and enlarged edition, 1984. 80, 84

[119] Arvind Narayanaswamy and Gang Chen. Thermal near-field radiative transfer between two spheres. *Phys. Rev. B*, 77:075125, Feb 2008. 92

[120] Philippe Ben-Abdallah, Svend-Age Biehs, and Karl Joulain. Many-body radiative heat transfer theory. *Phys. Rev. Lett.*, 107:114301, Sep 2011. 94, 97

[121] J. E. Pérez-Rodríguez, G. Pirruccio, and R. Esquivel-Sirvent. Fano interference for tailoring near-field radiative heat transfer. *Phys. Rev. Materials*, 1:062201, Nov 2017. 102

[122] Li Wang, Ruo-Yang Zhang, Meng Xiao, Dezhuan Han, C T Chan, and Weijia Wen. The existence of topological edge states in honeycomb plasmonic lattices. *New Journal of Physics*, 18(10):103029, oct 2016. 102

[123] H. Nyquis. Certain topics in telegraph transmission theory. *American Institute of Electrical Engineers, Transactions of the*, 1928. 105

[124] Herbert B. Callen and Theodore A. Welton. Irreversibility and generalized noise. *Phys. Rev.*, 83:34–40, Jul 1951. 105

[125] F. S. S. Rosa, D. A. R. Dalvit, and P. W. Milonni. Electromagnetic energy, absorption, and casimir forces. ii. inhomogeneous dielectric media. *Phys. Rev. A*, 84:053813, Nov 2011. 105

[126] R Kubo. The fluctuation-dissipation theorem. *Reports on Progress in Physics*, 29(1):255, 1966. 106

[127] D. Chandler. *Introduction to Modern Statistical Mechanics*. Oxford University Press, 1987. 107